DEPARTMENT OF THE AIR FORCE

AIR UNIVERSITY

AIR FORCE INSTITUTE OF TECHNOLOGY

Wright-Patterson Air Force Base, Ohio

AFIT/GEO/ENG/90D-02

A COMPACT OPTICAL ASSOCIATIVE MEMORY USING DYNAMIC HOLOGRAPHIC STORAGE MEDIA AND PHOTOREFRACTIVE GAIN AND ATTENUATION ELEMENTS

THESIS

Thomas Joseph Burns
Captain, USAF

AFIT/GEO/ENG/90D-02

Approved for public release; distribution unlimited

AFIT/GEO/ENG/90D-02

A COMPACT OPTICAL ASSOCIATIVE MEMORY USING DYNAMIC HOLOGRAPHIC STORAGE MEDIA AND PHOTOREFRACTIVE GAIN AND ATTENUATION ELEMENTS

THESIS

Presented to the Faculty of the School of Engineering

of the Air Force Institute of Technology

Air University

In Partial Fulfillment of the

Requirements for the Degree of

Master of Science in Electrical Engineering

Thomas Joseph Burns, B.S.E.E.

Captain, USAF

December 1990

Preface

When I entered AFIT, several graduating students warned me not to take on an "experimental" thesis. So, naturally, I did. And although there were times when equipment failures and long hours spent alone in the lab combined to test my patience, in the end, the experience proved extremely rewarding. In fact, I highly recommend a "hands on" thesis to anyone so inclined, provided they possess the same support I enjoyed throughout the course of the thesis. To the people who offered this support, I am deeply grateful.

To my advisor, Dr Steve Rogers, and my committee members for reviewing the manuscript and for granting me the freedom to choose my own path. To George Vogel and Ken Keppler, whose valuable insights kept me on that path and ultimately led to many of my successes. To Dave Ridenour and Dave Heatherington, whose patience and tireless assistance truly went above and beyond the call. And, finally, to the three most important people in my life, my wife, Anne, and my sons, Jacob and Joseph. This document carries my name, but contains your sacrifices. *Amor vincit omnia.*

Thomas Joseph Burns

Table of Contents

List of Figures

Abstract

This research effort implemented a compact optical associative memory architecture consisting of a Fabry-Perot Confocal Resonator (FPCR) optical processing environment, two dynamically reprogrammable Lithium Niobate volume holograms, and Barium Titanate gain and attenuation elements. The reduced physical dimensions of the compact optical processing environment make it more adaptable to military applications than previous associative memory designs.

The FPCR employs Mangin mirrors designed to reduce spherical aberrations in off-axis rays. The orientation of the gain element's grating vector angle and the model used to predict the profile of the attenuation element were unique to this research effort. The object stored in the associative memory was phase encoded using a glass microsope slide etched in a 40% hydrofluoric acid solution. Beam path deviations caused by the non-parallel geometry of the photorefractive crystals were corrected with a variable pitch, plate glass optical wedge inserted in the cavity's feedback arm.

Experimental results showed the system is capable of storing and fully retrieving a single object from memory when presented with partial information about the object. Additional system modifications are required to store and retrieve multiple objects.

A COMPACT OPTICAL ASSOCIATIVE MEMORY USING DYNAMIC HOLOGRAPHIC STORAGE MEDIA AND PHOTOREFRACTIVE GAIN AND ATTENUATION ELEMENTS

I. Introduction

1.1 Background

The mystery of the human brain's ability to easily locate and recognize a complex pattern in a cluttered scene, such as a tank surrounded by trees in a forest, has never been solved (19). For years, computer scientists have unsuccessfully tried to use the sequential processing power of digital computers to recognize objects a young child can casually identify at a glance. Many scientists now believe the solution to pattern recognition problems will not come through advancements in conventional Von Neumann digital computer technology, but through the development of "*computers*" that mimic the biological architecture of the human brain (1:88).

The brain is comprised of a vast collection of parallel, densely interconnected biological processors called neurons. Artificial neural networks are "brain inspired processors" that attempt to model elementary aspects of the structure and behavior of neurons (3:1572). One particularly important function performed by the brain is called associative memory. Associative memory is the ability to recall an entire object (e.g., word, picture, sound) when presented with partial or noise corrupted information about the object (23:6). One type of artificial associative memory, the Hopfield neural network, simulates the recall behavior of N biological neurons using an iterative feedback model consisting of N nonlinear computational elements (called artificial neurons) where the output of each artificial neuron is connected to the input of every other artificial neuron (17). The number of required interconnections and the time required to recall the correct stored object both increase with N. Thus, researchers are continuously looking for ways to increase interconnectivity and processing speed. "In this respect, one technology stands out as being particularly promising for constructing neural computers: optics" (1:88).

The basic component of an optical neural network is the hologram (28:1754). A hologram is a "wavefront reconstruction device" that records the interference pattern between an object

and a reference beam on a light sensitive medium and reconstructs the object beam when it is illuminated by the reference beam (15). The hologram can be viewed as an interconnection device that connects each point of light, or "neuron," in the input reference beam to each point of light in the output image beam (28:1754). Volume holograms, such as the photorefractive crystal Lithium Niobate ($LiNbO_3$), are particularly attractive for this application because they provide a large number of three-dimensional interconnections ($\approx 10^{12}$) and can store many holograms in a single crystal (28:1754). The associative memory investigated in this thesis uses $LiNbO_3$ holograms as memory storage and recall devices.

Several optical associative memory architectures were investigated in this thesis, with particular emphasis placed on the design developed by Stoll and Lee (25, 26, 31). The internal components Stoll and Lee use in their design are identical to those proposed by Wilson, and include two iron doped Lithium Niobate ($Fe : LiNbO_3$) volume holograms for memory storage and recall, and two Barium Titanate ($BaTiO_3$) gain and nonlinear thresholding elements (30). The major drawback to Stoll and Lee's architecture, from an Air Force perspective, is its size. Their design uses a variety of lenses and beamsplitters to form a large loop that make it impractical for use on an airborne platform. The architecture implemented in this thesis "collapses" the optical components used by Stoll and Lee into the relatively compact and lightweight confocal resonator shown in Figure 11.

1.2 Summary of Current Knowledge

Every associative memory architecture investigated in this thesis employs the same basic processing scheme. A hologram containing several memories is illuminated by an incomplete version of one of the stored memories. The hologram's output consists of an array of correlation peaks (one peak for each stored pattern), where the intensity of each peak is determined by how closely the corresponding pattern matches the input. A nonlinear thresholding device attenuates the weaker peaks and amplifies the strongest peak before they are used to "read out" their associated memories from a second hologram, T2. The output of the system is dominated by the memory generated by the strongest correlation peak and, thus, corresponds to the memory that most closely matches the distorted input.

The associative memory architecture implemented in this thesis consists of five major

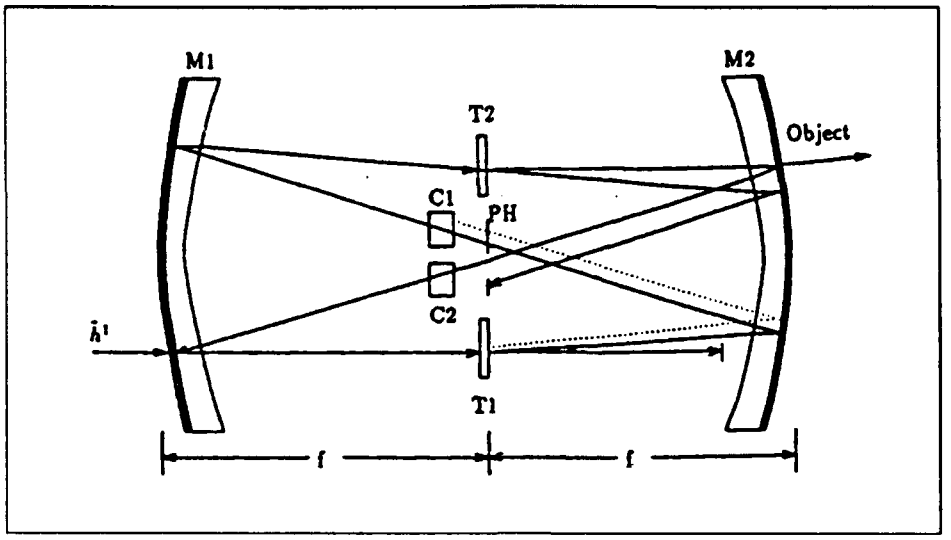

Figure 1. Fabry-Perot confocal resonator associative memory as proposed by Wilson (35:27).

components: two $Fe : LiNbO_3$ crystals, two z-cut $BaTiO_3$ crystals, and a Fabry-Perot confocal cavity resonator. Constructing and characterizing the ensemble operation of the components required a working understanding of the basic principles behind their operation.

1.2.1 $Fe : LiNbO_3$ Crystals. When two electromagnetic waves combine to form an interference pattern inside a $Fe : LiNbO_3$ crystal, photo-excited charge carriers migrate to dark regions in the crystal where they are trapped by local impurity centers. A net space-charge distribution is formed that modulates the crystal's index of refraction via the electro-optic effect. The point by point modulation of the index of refraction within the crystal forms a holographic grating. (16:206) Illuminating the crystal with either of the waves used to form the grating produces the other wave. Eichler reports as many as 500 holographic gratings (or, memories) have been written in a single 1 mm^2 crystal (7:169). However, in previous work performed at AFIT, Frye was never able to write and recall more than one grating at a time (13).

1.2.2 $BaTiO_3$ Crystals. Two $BaTiO_3$ crystals were used in the confocal resonator associative memory. One provided gain to compensate for energy losses as the signal beam traverses the cavity, the other acted as a thresholding device to eliminate cross-correlation noise. Gain was achieved through a process known as two-wave coupling in which energy from an

intense beam (pump beam) is deflected off a holographic grating in the direction of a weaker beam (signal beam). The amount of gain is a nonlinear function of the ratio of the power in both beams as well as the orientation of the crystal's optic axis with respect to the beams' bisector. (35) Wilson has reported gain values as high as 125 using a z-cut $BaTiO_3$ crystal. Wilson has also experimentally verified the gain's nonlinear dependence on the pump to signal beam power ratio. His results show a two-wave coupled $BaTiO_3$ crystal can be used to simultaneously attenuate small signals and amplify strong signals (35). Thus, a second two-wave coupled $BaTiO_3$ crystal was used to threshold the correlation peaks exiting the first hologram.

1.2.3 Fabry-Perot Confocal Resonator. A Fabry-Perot confocal resonator (Figure 11) is an optical feedback system consisting of two opposing concave mirrors with coincident focal points (5:945). An input entering the partially transmissive mirror M1 will reflect off M2 and arrive, Fourier transformed, at the midplane of the resonator. Successive reflections from M1 and M2 transform the input between the Fourier and image domains. The cavity output is located at M2 where a small portion of the beam passes through the partially transmissive mirror surface. When it reaches the point it entered the cavity, the signal beam recombines with the input and begins another oscillation. Because the input and feedback beams are coherent, they will form an interference pattern at the output. Intensity variations in the pattern will depend on path length (or phase) differences between the two beams. Extreme (bright/dark) phase variations limit the processing capability of the resonator. The confocal resonator used in this thesis employs Mangin, rather than conventional spherical mirrors, to reduce phase variations across the output plane. A Mangin mirror behaves like a doublet lens to correct spherical aberrations caused by non-paraxial rays. Fainman and Lee investigated a confocal resonator comprised of two confocal Mangin mirrors and found the mirrors significantly improved the resolution and space-bandwidth properties of the feedback system (8).

1.3 Problem Statement

Airborne platforms are currently not able to autonomously locate and recognize targets. Aircraft multi-sensor target detection systems provide the pilot with some target information, but the pilot must still perform the critical task of target recognition. "Smart" missiles cannot

distinguish a tank from a tree in a cluttered scene. An optical associative memory functioning as an automatic target recognition system could be used to reduce a pilot's combat target recognition workload as well as help guide a "fire and forget" missile to a specific target.

1.4 Objective

The objective of this thesis was to construct, demonstrate, and characterize a Fabry-Perot confocal resonator associative memory architecture for use as a large scale prototype of an airborne pattern recognition system.

1.5 Scope

This thesis implemented and characterized the confocal Fabry-Perot resonator associative memory architecture proposed by Wilson (35). Although no attempt was made to duplicate experimental results previously obtained at AFIT, many experiments were repeated to gain an understanding of each component's operating characteristics. Additional $Fe : LiNbO_3$ experiments were conducted to develop techniques for storing and retaining multiple memories and reducing cross-correlation noise.

1.6 Approach

The Fabry-Perot Confocal Resonator Optical Associative Memory architecture was constructed "from the ground up," beginning with individual evaluations of the performance of each component and ending with the successful implementation of a modified version of Wilson's original design. The experimental approach used to achieve these results was divided into three major sections.

1. *Preliminary Experiments.* Previously performed $Fe : LiNbO_3$ holography and $BaTiO_3$ two-wave coupling experiments were duplicated to gain an understanding of the operational characteristics of each component in the system (13, 22, 35). Additional two-wave coupling experiments were accomplished to further characterize the gain and attenuation behavior of two new z-cut $BaTiO_3$ crystals.

2. *Discrete Model of the Fabry-Perot Confocal Resonator Optical Associative Memory.* A model of the Fabry-Perot Confocal Resonator was designed and constructed from discrete optical components. This model served as a test bed for evaluating Wilson's proposed design by providing easy access to individual system components. The results obtained from experiments conducted in the discrete system led to modifications in Wilson's original design. After implementing the modifications, the system was able to recall a complete object when presented with partial information about the object.

3. *Fabry-Perot Confocal Resonator Optical Associative Memory.* The key components used in the discrete system were appropriately modified and placed inside the confocal resonator. A distorted version of a single object stored in the volume holograms was repeatedly presented to the system while component parameters were adjusted to achieve maximum recall efficiency. Additional modifications to the original architecture were made to enhance system performance. The system was eventually able to recall a complete object when presented with partial information about the object.

1.7 Organization

The organization of this thesis parallels the manner in which work progressed from theoretical development to experimental demonstration. Chapter 2 provides an overview of associative memory concepts, the Hopfield neural network associative memory and several "Hopfield-like" optical associative memory architectures. Chapter 3 develops the detailed theory of each of the system's internal components and compares the behavior of a Hopfield neural network with a Fourier optics mathematical model developed to describe the system's holographic recall process. Chapter 4 provides experimental results of preliminary investigations into the two wave coupling gain and attenuation processes. These are followed by a detailed description of the methodology, procedures and results obtained from associative memory experiments conducted in the discrete optical feedback system. Chapter 5 provides similar information for the associative memory experiments performed in the Fabry-Perot Confocal Resonator. Conclusions and original contributions are provided in Chapter 6.

II. Literature Review

2.1 Introduction

Associative memories are able to retrieve an entire object from memory when presented with partial or noisy information about the object. Neural network associative memories achieve these results quickly and accurately by using a large number of parallel and extensively interconnected processing elements. Optical processing elements have demonstrated the ability to rapidly connect 10^6 parallel input channels to 10^6 parallel output channels (27:98). Consequently, many designers of modern associative memory architectures are combining the speed and interconnectivity of optics with the computational methods of neural networks (25:1900). In particular, many modern optical designs employ an inner product processing technique derived from a neural network model proposed in 1982 by J.J. Hopfield (17). This chapter describes the fundamental concepts of associative memory storage and recall and relates them to the Hopfield neural network model. Several different optical Hopfield-like neural networks are then investigated, concluding with a discussion of the architecture proposed by Wilson and implemented in this thesis (35).

2.2 Associative Memory Storage and Recall

Although there are many different types of associative memory schemes present in the literature (e.g., matrix-vector, holographic, neural network), most display the same basic associative behavior (12). Multiple sets of associated patterns ($u^k \rightarrow v^k$) are stored in a static or dynamic fashion so that subsequent presentations of a key pattern, u^k, will generate its paired pattern, v^k. If the stored patterns are different, the memory is heteroassociative. If the stored patterns are identical ($u^k = v^k$), the memory is autoassociative. In general, heteroassociative memories are used to make decisions, and autoassociative memories are employed for error correction, noise reduction and image restoration (4:273).

Associative memory schemes can be classified by the manner in which they learn (store) and recall information (28:1752). Storage of associated pairs is accomplished using either dynamic or static learning rules. (12:504). Dynamic learning implies the associations are learned over time,

generally through an error driven process. Dynamic learning can be described by the equation

$$\frac{dW}{dt} = f(W, u^k, v^k, v) \tag{1}$$

where $W(x, y, x', y', t)$ is the weight pattern used to store the associations $u^k \rightarrow v^k$, $v(x, y)$ is the recalled output pattern and the superscript k represents a specific pattern contained in a larger set of patterns (12:505). Conversely, static learning is not time dependent and is a function only of the associated pattern vectors (i.e., $W = f(u^k, v^k)$) (12:5041). The associative memory learning methods employed by the architectures investigated in this thesis are static.

The recall behavior of optical associative memories capable of selecting the correct object from partial information is generally, but not always, dynamic. In a dynamic recall process, the output evolves over time until reaching a steady-state output corresponding to the object that most closely matches the input.

A static recall associative memory is capable of generating the correct output in a non-iterative, or single pass, manner. A simple mathematical example of a static recall operation is provided below.

Let the static recall equation for a heteroassociative memory capable of recalling a one-dimensional pattern, $v^k(x)$, when presented with a one-dimensional input $u^k(x)$ be given by the expression

$$v(x) = \int W(x, y) u^m(y) dy \tag{2}$$

where $u^m(y)$ is an input pattern corresponding to one of the stored patterns $u^k(y)$. Additionally, assume the associative memory has been trained in advance to store M associations through the following static learning process:

$$W(x, y) = \sum_{k=1}^{M} v^k(x) u^k(y) \tag{3}$$

Inserting equation 4 into equation 3 and rearranging the integral and summation signs yields the following expression for the recalled pattern $v(x)$:

$$v(x) = \sum_k v^k(x) \left[\int u^k(y) u^m(y) dy \right] \tag{4}$$

The bracketed term in equation 5 represents the inner product of the input with each of the stored input patterns. If the stored input patterns are orthogonal and energy normalized, the bracketed term equals 0 when $k \neq m$ and 1 when $k = m$ (12:5041). Under these conditions, the output is the desired association $v^k(x)$. Although the storage and recall equations used in this example are quite simple, they provide the foundation for the mathematical behavior of the Hopfield neural network discussed in the following section.

2.3 Hopfield Neural Network Associative Memory

The Hopfield neural network consists of a single layer of N nodes (or neurons), where each neuron is connected to one element of a 1 x N input vector (Figure 2). The output of each neuron, V_i, is connected to its own input and the inputs of all other nodes through a weighted N x N feedback interconnection matrix, W_{ij} (29:80).

A simple mathematical model describing the input-output behavior of a single, N input, neuron is given by

$$V_i = f\left(\sum_{j=0}^{N-1} W_{ij} V_j \right) \tag{5}$$

where f is a nonlinear thresholding operation and W_{ij} is the connection weight linking the output of neuron j to the input of neuron i (18). Assuming the nonlinear behavior of the neuron described by equation 1 is a hard limiter, it will respond with a 0 if $\sum_j W_{ij} V_j$ is slightly smaller than 0, and with a +1 if $\sum_j W_{ij} V_j$ is slightly greater than 0.

The storage and recall behavior of the Hopfield net is often expressed in matrix-vector rather than integral form to satisfy the constraints of a digital computer (12). Given M autoassociated

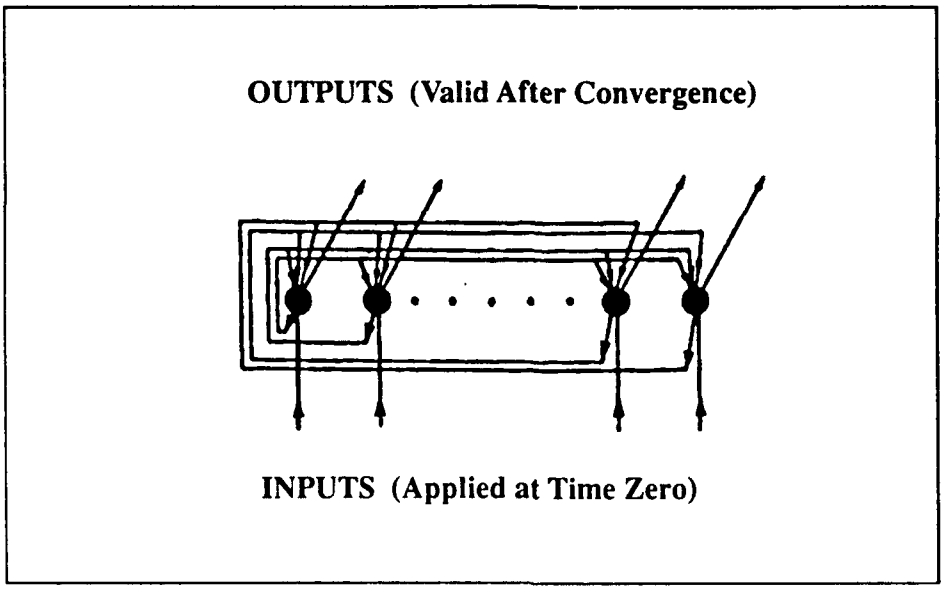

Figure 2. Hopfield neural network (23:6).

vector pairs, $\mathbf{V}^k \rightarrow \mathbf{V}^k$, the matrix-vector storage and recall equations are

$$W_{ij} = \sum_{k=1}^{M} V_i^k V_j^k \quad (i \neq j;\ = 0\ for\ i = j) \tag{6}$$

$$V_i(t+1) = f\left(\sum_j W_{ij}\hat{V}_j(t)\right) \tag{7}$$

where f is a nonlinear function, $\hat{V}_j$ is a distorted input, and the time dependence implies the network iterates until it converges on the memory closest in the Hamming sense to the distorted input (18).

Equations 7 and 8 show the Hopfield net learns by generating an interconnection matrix formed through an *outer product* process involving each of M associative pairs. Farhat has shown the same results can be achieved by taking a different, but mathematically equivalent approach involving a vector *inner product* process (10:5095). Inserting equation 7 into equatic . 8 and

interchanging the order of summations yields the following expression for the steady state output:

$$\begin{aligned} V_i &= f\left(\sum_k V_i^k \left[\sum_j V_j^k \hat{V}_j\right]\right) \\ &= f\left(V_i^{ko}\sum_j V_j^{ko}\hat{V}_j^{ko} + \sum_{k\neq ko} V_i^k \sum_j V_j^k \hat{V}_j^k\right) \\ &= f\left(V_i^{ko}(V^{ko},\hat{V}^{ko}) + \sum_{k\neq ko} V_i^k(V^k,\hat{V}^{ko})\right) \end{aligned} \tag{8}$$

where $\hat{V}^{ko}$ is a distorted version of V^{ko} and $(\cdot,\cdot)$ denotes the *inner product* operation. Equation 9 implies the steady state output of the modified Hopfield network is the weighted sum of all stored memories where the weights equal the inner product of each memory with the distorted input. The first term in equation 9 is generally referred to as the auto-correlation of the input with its matching memory while the remaining terms are considered cross-correlation noise. *It is important to note that even though the terms in equation 8 and 9 have been rearranged, the expressions are still mathematically equivalent* (10:5095). The fact that the same result can be achieved either by taking the outer product of each of the associated exemplar vectors, or by taking the inner product of each exemplar vector with the distorted input, is used later to draw a comparison between the operation of the Fabry- Perot Confocal Resonator Optical Associative Memory and the Hopfield neural network.

2.4 Optical Associative Memories

Optical associative memories, as the name implies, rely on optical devices and optical information processing techniques to retrieve noise-free objects when addressed by partial or distorted input objects (25:1900). A key component in many optical associative memories is the hologram. Two common holographic associative memory architectures used in the past are the ghost image generator and the correlation peak detector (26:428). Both types are shown in Figure 3.

The ghost image associative memory was introduced by van Heerden in 1963 (32:387). In this architecture, the input is correlated with each of M memories stored in the first hologram. The output consists of M correlation peaks where the brightest peak corresponds to the memory

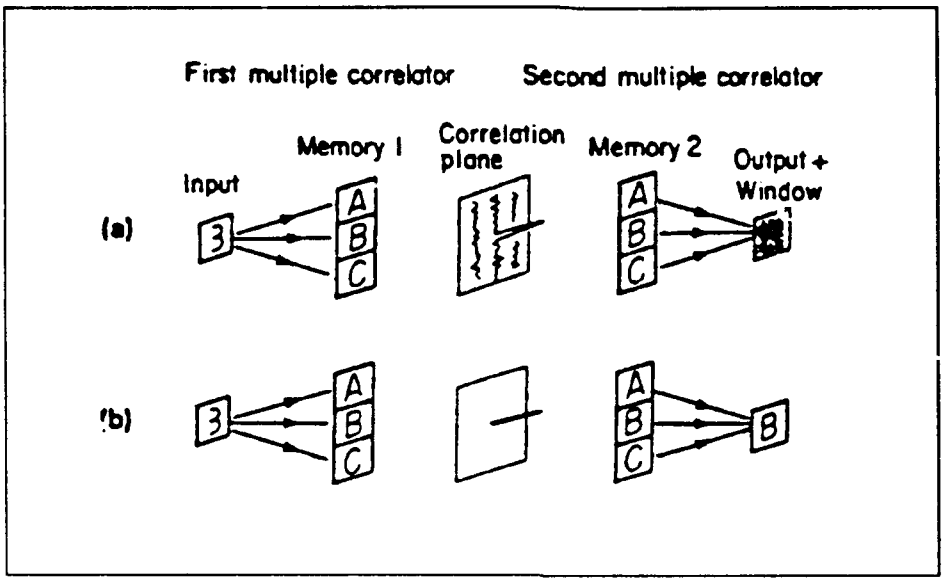

Figure 3. Two types of holographic associative memories (a) ghost image, and (b) peak detector (26:429).

that most closely matches the *input*. Each correlation peak is used as a reference beam to read out its associated image stored in a second hologram. The output of the second hologram is a superposition of every image stored in the second hologram, with the brightest image corresponding to the brightest correlation peak. The disadvantages of this architecture are that it can only store and recall a limited number of images and the recreated images in the output are usually severely degraded from cross-correlation noise (25:1900). The peak detection architecture seeks to eliminate cross-correlation noise by filtering the peaks in the correlation plane.

The peak detection associative memory also correlates a distorted input with each memory stored in the first hologram. However, in contrast to the ghost holography architecture which allows each peak to address the second hologram, the peak detection scheme only allows the strongest peak to pass through the correlation plane. Thus, a single memory corresponding to the best match between the input and the stored objects is produced at the output. (26:428). The major drawback of this architecture is that it requires an active device in the correlation plane to locate and select the brightest correlation peak. Active devices are often expensive, cumbersome and subject to failure.

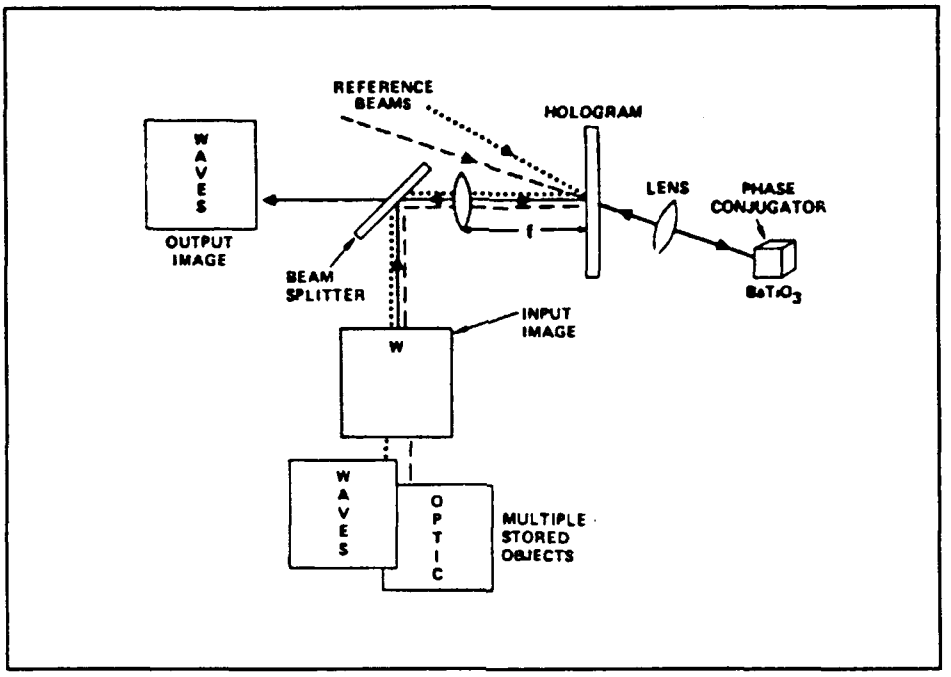

Figure 4. Phase conjugate autoassociative memory as implemented by Owechko, et al. (25:1905).

With the resurgence of interest in neural networks, many optical associative memory designers have turned to architectures that combine the memory storage and recall advantages of holograms and the computational methods of neural networks (25:1900). Three key components present in modern holographic associative memories that mimic neural networks are feedback, nonlinear thresholding and interconnectivity. Several recently proposed and/or implemented optical neural network associative memory architectures employing these principles are discussed below.

2.4.1 Y. Owechko, et al. - Phase Conjugate Optical Associative Memory. Owechko's architecture uses a thermoplastic hologram to provide interconnectivity between the input and output and a four-wave coupled phase conjugate mirror (PCM) as a nonlinear thresholding and gain element. A diagram of Owechko's "open loop" architecture (the output is not fed back to the input) is shown in Figure 4.

Multiple objects are stored in the hologram through an angle- multiplexing Vander Lugt

filtering scheme in which the phase and amplitude of each object is captured by creating an interference pattern in the hologram with a plane wave reference beam traveling at an angle unique to that object. The hologram is then illuminated by a distorted version of one of the stored objects and the output is Fourier transformed and projected onto the PCM.

As shown by Goodman, illuminating a Vander Lugt hologram with an incomplete version of a stored object and Fourier transforming its output generates a separate correlation term in the Fourier plane for each stored object. (15:175). The intensity of each correlation peak is proportional to the degree of correlation between the distorted input and the object recorded using that reference beam. Owechko points out this correlation process is analogous to the inner product operation described by equation 9 (25:1903).

The four-wave coupled PCM acts as a nonlinear thresholding and gain device by attenuating low intensity correlation peaks (corresponding to objects that don't match the distorted input) and amplifying the high intensity peaks. The PCM retroreflects the thresholded correlation peaks back towards the hologram where they read out their associated memories.

The output of the hologram is a superposition of every memory stored in the hologram, each weighted by the strength of the correlation between the distorted input and the memory. The strongest output pattern (the auto correlation term shown in equation 7) corresponds to the best match between the distorted input and the stored objects. Owechko demonstrated the performance of the system by storing two words, optics and waves, in the hologram. He presented distorted versions of each word and the network was able to correctly choose and reconstruct the complete word (25:1909).

Although Owechko's associative memory was able to correctly select between two stored objects when presented with a distorted version of one object, the architecture limits the number of objects that can be stored and unambiguously recalled. As Psaltis points out, thin film holograms have small storage capacities compared to other optical materials (e.g., photorefractive crystals) (28:1754). Additionally, thin film holograms are fixed. That is, a new hologram must be created each time a memory is added to the system. Finally, because this is a single pass system, the additional processing power offered through iterative feedback is lost. Paek and Psaltis were able to achieve much better results using a closed loop system.

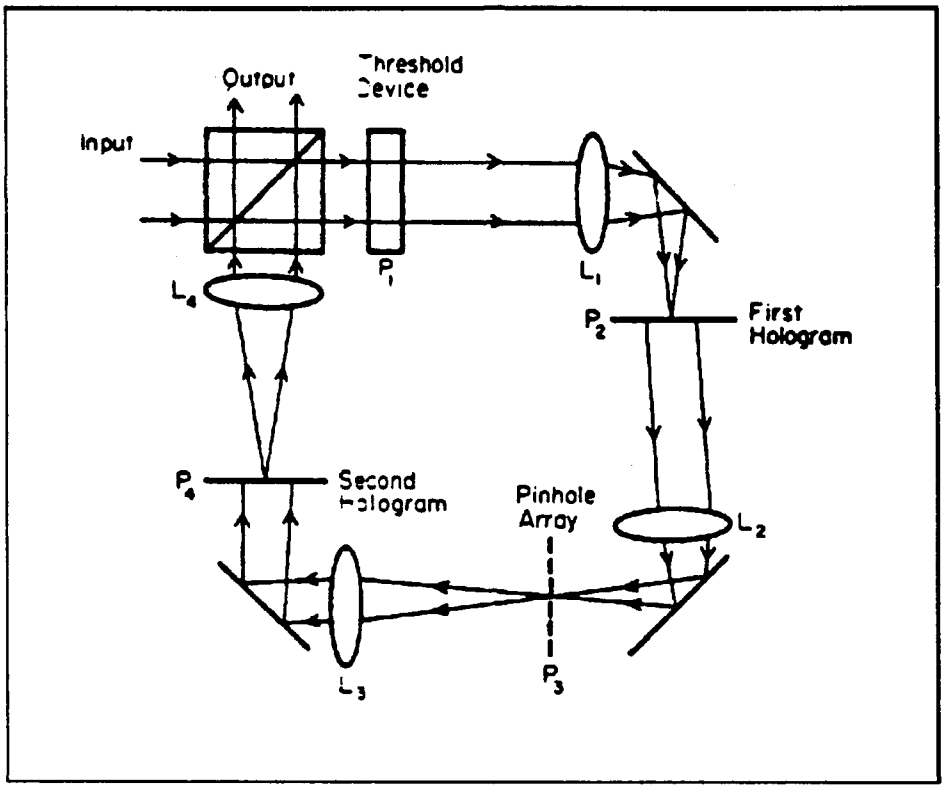

Figure 5. Paek and Psaltis' optical associative loop. The thresholding device is a microchannel spatial light modulator (26:431).

2.4.2 E. Paek, D. Psaltis - Optical Associative Loop. Paek and Psaltis developed a closed loop autoassociative memory architecture that employs a spatial light modulator thresholding and gain device, two thermoplastic holograms for memory storage and recall, and a set of pinholes placed in the correlation plane to remove unwanted cross-correlation noise (26:432). A diagram of their architecture is shown in Figure 5.

When presented with a distorted version of a stored object, the first hologram and L2 combine to generate a separate peak in the correlation plane for each stored memory. As before, the intensity of each peak is determined by how closely the input matches each memory. Each peak is then "pinholed" in the correlation plane to eliminate cross talk. The resulting points of light, converted to reference beams by L3, are used to read out their associated memories from the second hologram. A single wave containing the superposition of each memory leaving the second hologram travels to the beam splitter where a portion exits the system as an output and the

remainder combines with the input to form a closed loop path. The opto-electronic thresholding device then attenuates the weaker memory components and accentuates (amplifies) the strongest component. The amplification provides enough gain to overcome the losses in the loop introduced by the lenses, mirrors and holograms.

The system was able to select and clearly reconstruct a complete object from a distorted image of one of four stored memories (each memory was a gray scale picture of a person's face). Paek and Psaltis attributed their results to the elimination of cross- correlation noise between peaks in the correlation plane.

Cross-correlation noise was reduced by first edge-enhancing the input and stored objects and then "pinholing" the peaks in the correlation plane. The objects were edge-enhanced by using a phase diffuser to spread energy out of the object's D.C. frequency component into higher spatial frequency components. As shown by Goodman, the size (physical dimension) of a correlation term produced by correlating two edge-enhanced objects is smaller than the size of the term produced by correlating two normal objects (15:136). Thus, edge-enhancing allowed Paek and Psaltis to reduce the amount of overlap (cross talk) between correlation terms in the correlation plane. They were able to reduce the cross talk even further by placing .35 mm diameter pinholes at the center of each correlation peak. The pinholes allowed only the bright central region of each peak to pass, effectively blocking the cross-correlation noise surrounding the peak.

Although Paek and Psaltis were able to successfully reconstruct a distorted input corresponding to one of four stored objects, their architecture has two major drawbacks. First, the spatial light modulator used to provide thresholding and gain is an active device that is expensive and delicate. Second, as before, the thermoplastic holographic storage media prevents the rapid addition or deletion of system memories (i.e., real time adaptive learning). Frye attempted to overcome these limitations using a photorefractive crystal as a memory storage device and two "passive" opposing self-pumped PCMs as a resonant feedback cavity.

2.4.3 D. Frye - Resonant Phase Conjugate Holographic Associative Memory. Frye's optical associative memory architecture employs an iron doped Lithium Niobate ($Fe : LiNbO_3$) volume hologram as an input/output interconnection element and two opposing Barium Titanate ($BaTiO_3$) self-pumped phase conjugate mirrors as nonlinear thresholding and feedback ele-

ments (13). As opposed to the "fixed" nature of thermoplastic holograms, $Fe : LiNbO_3$ is an "adaptive" photorefractive crystal in which holograms can be written, read out and erased in nanosecond time frames (7:71). A diagram of Frye's "closed loop" architecture is shown in Figure 6.

The architecture is based on a design proposed by Dunning et al. (13:57). It consists of two optical "legs," where each leg contains a PCM. Each object is passed through a phase diffuser to spread the energy in the object into its higher frequency components. The Fourier transform of each object is then stored in the volume hologram using an angle multiplexing scheme. When the volume hologram is illuminated by an incomplete object, it generates one weighted correlation term for each stored memory. The first self-pumped PCM nonlinearly thresholds the correlation terms and reflects them back towards the hologram where they "read out" their associated memories. A single wave carrying the weighted superposition of every memory stored in the hologram is focused onto a second self-pumped PCM. Each memory is conjugated and returned to the beam splitter where part of the wave exits the system as the output and the remainder combines with the original input to "fill in" the missing portion of the object. After a sufficient number of iterations, the missing portion of the incomplete object is restored.

Frye's experimental investigation of the behavior of the resonant cavity associative memory was divided into three main parts. He first determined the input parameters required to maximize the diffraction efficiency of the volume hologram. Diffraction efficiency is defined in this experiment as the ratio of the power in the correlation beam to the power of the input beam (Figure 7). Second, he investigated the recall behavior for multiple objects stored in a *single pass system.* Finally, he attempted to implement the resonant cavity architecture.

The diffraction efficiency of the $LiNbO_3$ crystal was measured as a function of three separate parameters: 1) the total power of the reference and object beams, 2) the ratio of the reference beam power to the object beam power, and 3) the polarization of the object beam. The experimental arrangement is shown in Figure 7.

Frye's results show the diffraction efficiency is maximized when 1) the total power of the reference and object beams equals 36.5 mW, 2) the ratio of the reference beam to the object beam is 6 to 1, and 3) the object beam polarization is parallel to the optic axis (13:24-26). After adjusting

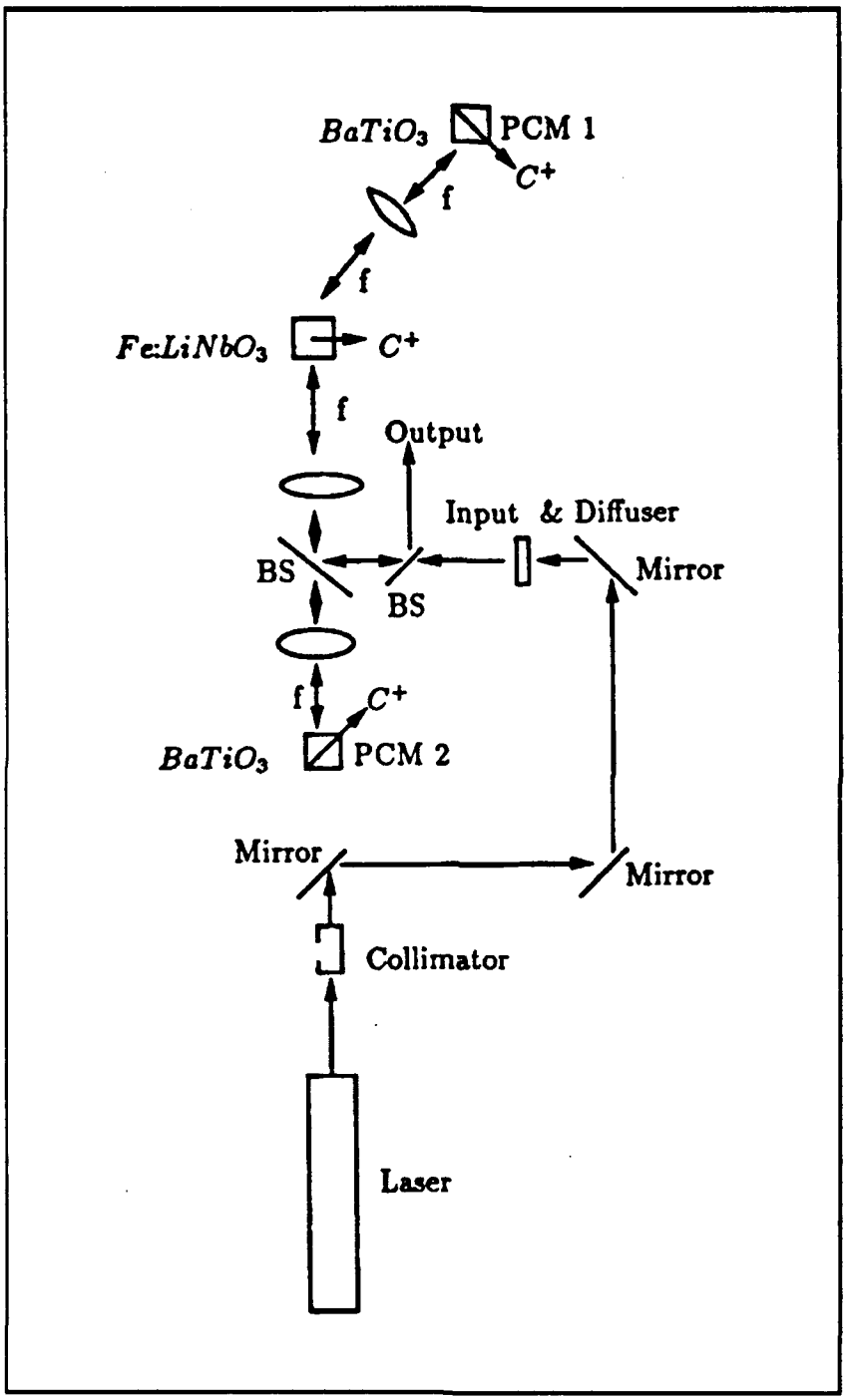

Figure 6. Resonant cavity associative memory. The holographic storage media is $LiNbO_3$ and the cavity feedback elements are self-pumped phase conjugate mirrors made from $BaTiO_3$ (13:58).

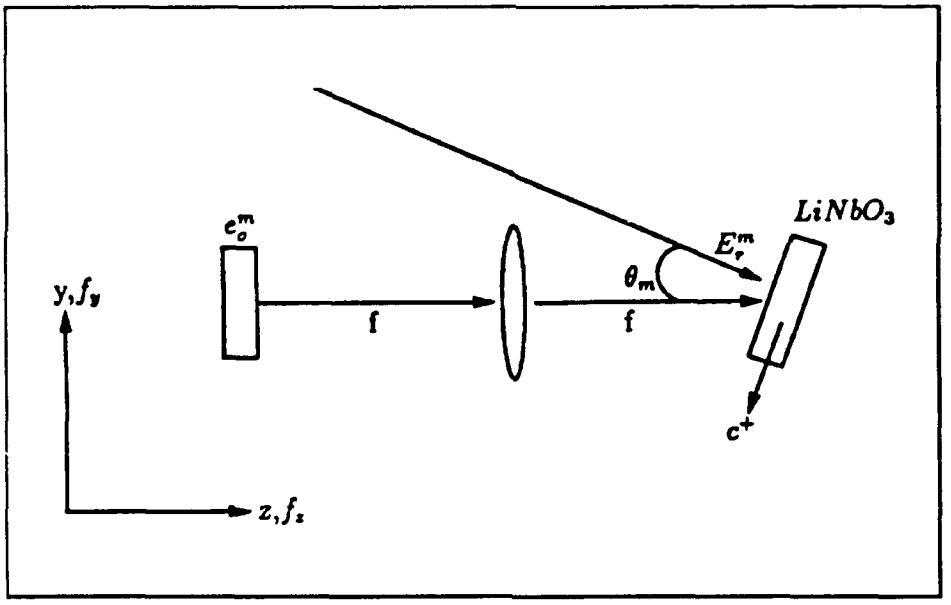

Figure 7. Frye's experimental arrangement for investigating the optimum diffraction efficiency of a $LiNbO_3$ hologram. E_r^m is a unique plane wave reference beam corresponding to each stored image e_o^m (13:33).

the reference and object beams to obtain maximum diffraction efficiency, Frye investigated the storage and recall of multiple objects in a single pass associative memory.

The Fourier transforms of three phase diffuse objects were stored in a $Fe : LiNbO_3$ crystal using multiplexed plane wave reference beams. The hologram was illuminated with both a distorted and complete object, and the output of a *single pass associative memory* architecture resembling Owechko's was observed. It was found the system was capable of recalling a complete image when presented with a complete object. However, unlike Owechko's results, it would not reconstruct a complete image from a distorted object (recall that Owechko used a four-wave coupled PCM that provided system gain, while Frye's self-pumped PCM introduced a system loss). Additionally, Frye found when he illuminated a multiple object hologram with one of the stored objects and waited sufficiently long for the PCM to form a presentable output (3 to 5 minutes), the gratings associated with the other objects were distorted or erased. He was never able to correct this problem and ultimately recommended permanently "fixing" the images stored in the crystal by using a thermal cycling process (13:54). In Frye's final experiment, he attempted to improve

the system's recall performance by using a second PCM to create a closed loop, resonant cavity.

The resonant cavity was constructed, and a single object was stored in the volume hologram. Although the original intent of the experiment was to show the system would reconstruct a complete image when presented with a *distorted* object, it was found the system would not play back an image when presented with a *complete* object. Power measurements at different points in the system showed "the losses in the system were sufficient to stifle full resonant oscillations" (13:61). In order to achieve enough gain to overcome system losses, Frye recommended (but did not implement) using either four-wave coupled PCMs or adding a two- wave coupled gain element in the leg containing the first PCM. Researchers at Hughes Research and Technology Center successfully demonstrated a closed loop architecture that implemented the latter suggestion.

2.4.4 H. Stoll, L-S. Lee - Oscillating Ring Resonator. Stoll and Lee's closed loop architecture is similar to Paek and Psaltis' with two major exceptions. First, two adaptive photorefractive $Fe : LiNbO_3$ holograms, rather than fixed thermoplastic holograms, provide memory storage and recall. Second, two, passive two-wave coupled $BaTiO_3$ crystals are used to perform the nonlinear thresholding and gain operations performed by Paek and Psaltis' spatial light modulator (30). A diagram of Stoll and Lee's architecture is shown in Figure 8.

When illuminated by a distorted version of a stored object, the first hologram (containing the Fourier transform of the phase diffused objects) produces an array of correlation peaks that are "pinholed" to eliminate cross-correlation noise. A non- saturated, two-wave coupled $BaTiO_3$ crystal is used to amplify the central region of each correlation peak to improve the read out performance of the second $Fe : LiNbO_3$ hologram. As before, a single wave containing the weighted superposition of the system memories is produced by the second hologram. The wave is passed through a beam splitter, and the portion that does not exit the system as output is passed through a saturated, two-wave coupled $BaTiO_3$ crystal that nonlinearly thresholds the weighted memories. The system is allowed to resonate in this manner until it reaches a steady state solution.

The gain and nonlinear thresholding behavior of two-wave coupled $BaTiO_3$ crystals has been investigated at AFIT by Wilson and Keppler (35, 22). A typical two-wave coupled $BaTiO_3$ crystal is shown in Figure 9. Gain is achieved by interfering the pump and probe (signal) beams inside the crystal to form an interference grating that deflects energy from the pump to the signal

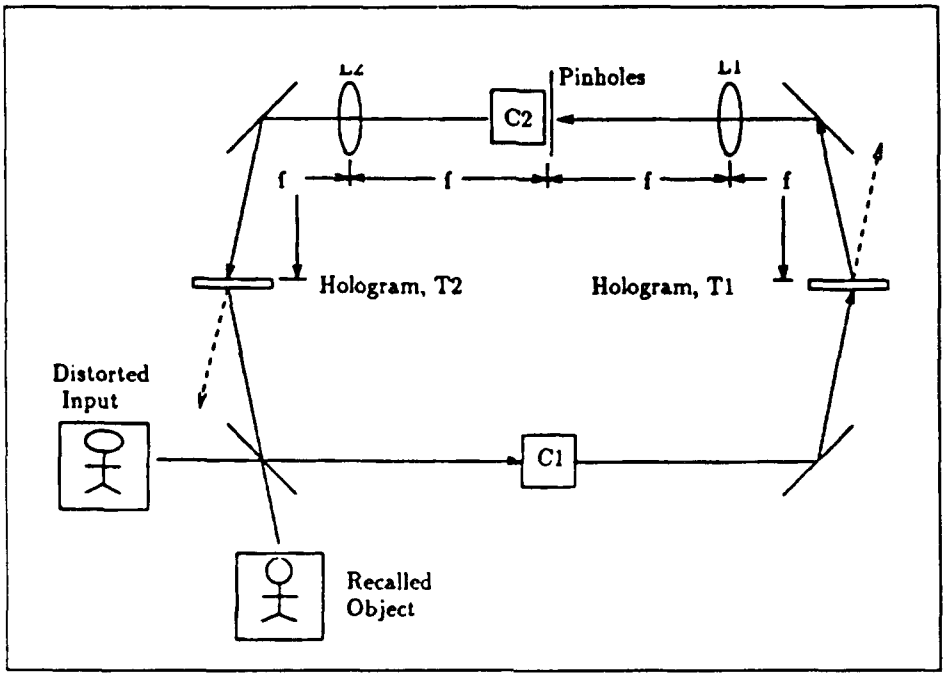

Figure 8. Stoll and Lee's closed loop optical associative memory. The $Fe : LiNbO_3$ crystals allow adaptive storage and recall. Two $BaTiO_3$ crystals provide nonlinear thresholding and gain (35:14).

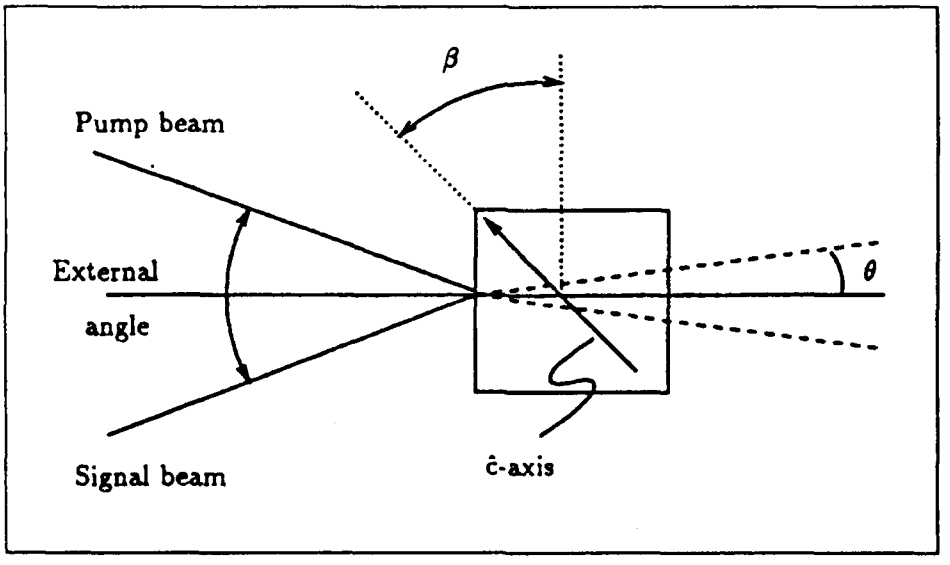

Figure 9. A two-wave coupled z-cut $BaTiO_3$ crystal (22:32).

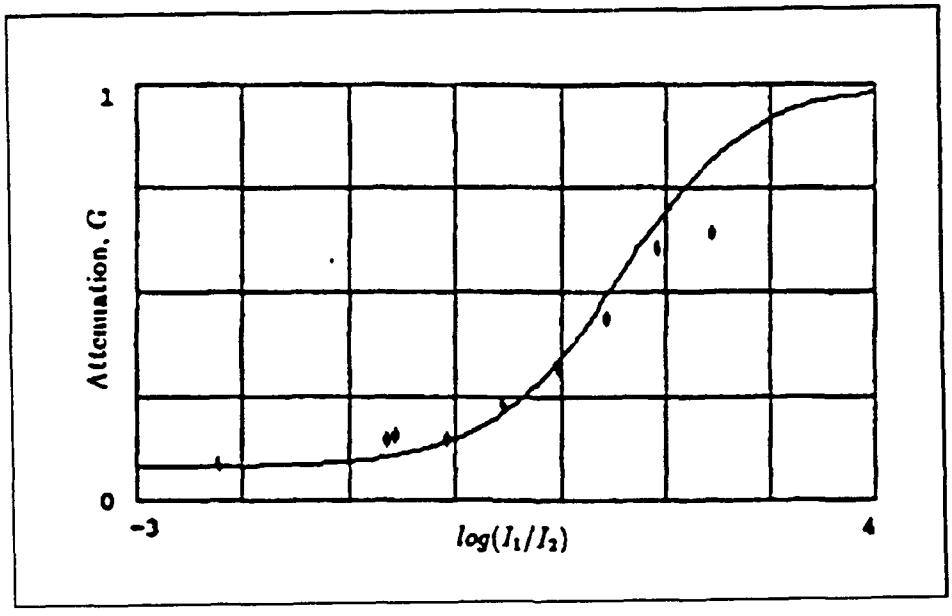

Figure 10. Experimentally obtained curve showing the dependence of a two-wave coupled $BaTiO_3$ on the ratio of the pump and probe beams. I_1 is the signal beam and I_2 is the probe beam. Probe beam intensity is $312\mu W/cm^2$ (35:59).

beam (22). The amount of deflected energy, or gain, is a function of the input external angle, θ_{ext}, the grating vector, β, and the ratio of the pump to probe power. For a z-cut $BaTiO_3$ crystal (i.e., the optic axis is parallel to the crystal face), with $\theta_{ext} = 6.6^o$, $\beta \approx 15^0$, and pump and probe beam intensities of $47.7mW/cm^2$ and $395\mu W/cm^2$ respectively, Wilson was able to achieve a steady state gain of 125 (or $\approx 20dB$) (35:54). Stoll and Lee have reported gains of 32 dB (30:376). However, neither author clearly defines how they measured gain. Wilson's experiments also demonstrated the strong nonlinear relationship between gain, and pump to probe power ratio. The experimentally obtained curve shown in Figure 10 for $\theta = 6.6^o$ and $\beta = 8.2^o$ clearly demonstrates why $BaTiO_3$ is used as a nonlinear thresholding element (35).

Stoll and Lee's first experiment involved the storage and recall of two, non-orthogonal views of an M-1 tank. Even presenting a heavily obscured version of one of the views, they were able to obtain complete recall in $\approx$ 3 seconds. In their second experiment, they stored two top views of a T-62 tank in a horizontal and vertical orientation and rotated the input to determine the rotation invariance of the network. "The dominant vertically oriented view was recalled for stimuli rotated

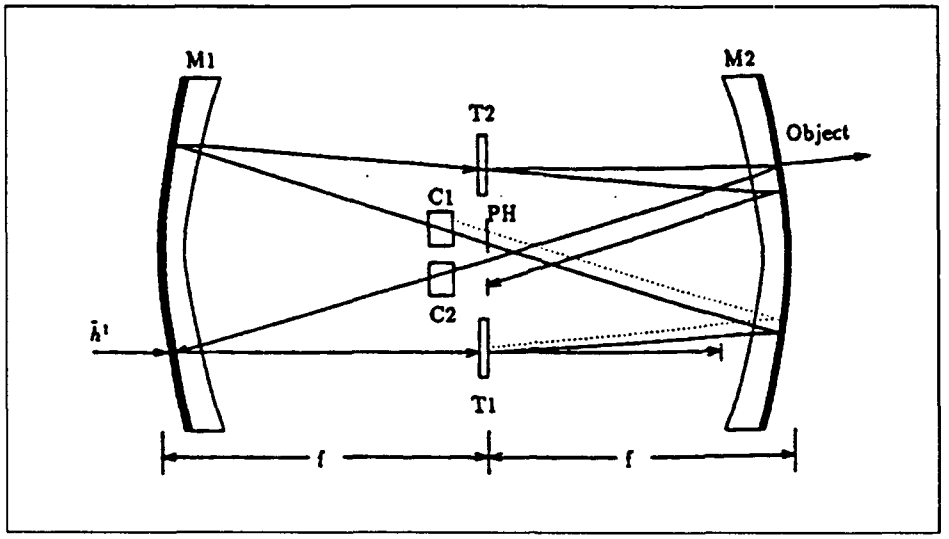

Figure 11. Fabry-Perot confocal resonator associative memory as proposed by Wilson (35:27).

between $\sim 45^o$ and $\sim 90^o$ from the horizontal, and the horizontally oriented view was recalled for stimuli rotated between $\sim 0^o$ and $\sim 30^o$ from the horizontal." (31:164)

By replacing Paek and Psaltis' spatial light modulator and thermoplastic holograms with photorefractive crystals, Stoll and Lee were able to improve the network's ability to adaptively store and recall new memories as well as its overall reliability. However, the ring resonator architecture is certainly not compact, and would therefore be impractical for use on an airborne platform. Thus, Wilson proposed placing the internal components of the architecture inside a compact Fabry-Perot confocal resonator (35).

2.4.5 J. Wilson - Fabry-Perot Confocal Resonator Associative Memory. Like Stoll and Lee, Wilson also uses $BaTiO_3$ gain and nonlinear thresholding elements. The primary difference between the two architectures is the manner in which feedback is achieved. Wilson proposes to reduce the space required to implement Stoll and Lee's ring resonator by placing the processing elements inside a Fabry- Perot confocal resonator. A diagram of Wilson's architecture is shown in Figure 11.

When a distorted input illuminates the first hologram (T1), correlation terms are generated which are Fourier transformed by M2 into an array of correlation peaks in the midplane of the

resonator. The central region of each peak is "pinholed" and Fourier transformed by M1 to form a plane wave reference beam with a unique spatial frequency. The reference beams combine at the second hologram, T2, to generate an output containing a weighted superposition of the network's stored memories. The network is allowed to oscillate inside the confocal resonator until a steady-state solution is reached. Wilson was able to construct the confocal resonator and characterize the gain and thresholding behavior of the z-cut $BaTiO_3$ crystal.

The confocal resonator constructed and characterized by Wilson (confocal because the focal points of both mirrors are located at the same point) consists of a Burleigh 6 inch resonator and two identical Mangin mirrors with effective focal lengths of 35 cm (35). Wilson chose the confocal resonator for his feedback system because it offers a compact optical processing environment containing two separate image and Fourier planes. The optical processing capability of the resonator was demonstrated by Cederquist et al., who showed by placing optical processing elements in the Fourier planes (e.g., pinholes, nonlinear crystals, etc.) the resonator is able to rapidly solve complex partial differential equations (5).

Wilson was able to further improve the resonator's processing power by using Mangin, rather than spherical mirrors (35:8). Unlike spherical mirrors that suffer from aberrations caused by defocused non-paraxial rays, Mangin mirrors are designed to focus paraxial and non-paraxial rays at the same location in space. Their use in a confocal resonator was first investigated by Fainman et al., who found they significantly improved the space-bandwidth and resolution properties of the confocal system (8).

Wilson's investigation of the image amplification and nonlinear properties of z-cut $BaTiO_3$ crystals (Section 2.4.4) confirm their utility as associative memory gain and thresholding elements. Additionally, Wilson's construction and characterization of the Fabry-Perot confocal resonator laid the groundwork for the follow- on work contained in this thesis.

2.5 Conclusion

The basic principles of an associative memory were presented as a foundation for understanding the Hopfield neural network. The Hopfield neural network was described in terms of an outer product learning rule and a dynamic memory recall equation. It was shown the

network's behavior can also be modeled by a mathematically equivalent inner product operation characteristic of modern optical associative memories. Several inner product optical associative memory architectures were compared in terms of their memory storage and recall, feedback and nonlinear thresholding properties. Design features that improved system performance and reliability were highlighted, including 1) $Fe : LiNbO_3$ volume holograms, 2) correlation plane pinholes, 3) edge-enhanced images, 4) two-wave coupled $BaTiO_3$ gain and thresholding elements, and 5) a confocal resonator feedback system. The next chapter discusses in detail how each of these features contributes to the operation of Wilson's proposed confocal Fabry-Perot associative memory architecture.

III. Theory

3.1 Introduction

Chapter 2 summarized the concept of an associative memory and presented several approaches used in the past to implement optical associative memories. The chapter concluded with an overview of the Fabry-Perot Confocal Resonator Optical Associative Memory (F- OAM) investigated in this thesis. The purpose of this chapter is to first explore in more detail the theory behind the operation of each of the F-OAM's components including the confocal resonator, $BaTiO_3$ gain and thresholding elements, and $LiNbO_3$ holographic storage media. The theoretical behavior of the ensemble operation is then developed from a Fourier optics perspective and comparisons are drawn between the Hopfield associative memory model and the behavior of the F-OAM.

3.2 Fabry-Perot Confocal Resonator

3.2.1 Optical Feedback. Optical feedback systems, like their electronic counterparts, combine a system input with a processed version of the system's output to gain a processing capability not achievable in single pass operation. Figure 12 shows a block diagram of an optical feedback system.

Assuming the system is coherent (i.e., the round trip path length is shorter than the coherence length of the laser), the input and output, $i(x,y)$ and $o(x,y)$, represent complex wavefront amplitudes. Block A serves as a system input element and combines the feedback image leaving block D with the input. Block C allows a portion of the system output to pass and reflects the remainder into feedback element D. Blocks A and C are typically beamsplitters or partially transmitting mirrors. Blocks B and D are optical processing elements used to control the transfer characteristics of the system.

The optical path length of the feedback arm of the optical system determines the phase difference, β, between the input and feedback wavefronts. If the path length is such that $\beta = 2\pi m$, where m is an integer, the feedback is positive. Negative feedback occurs when $\beta = (2m+1)\pi$, while any other value of β provides complex feedback (6:312). Because the transfer function of the optical feedback loop is a function of the phase difference between the input and feedback

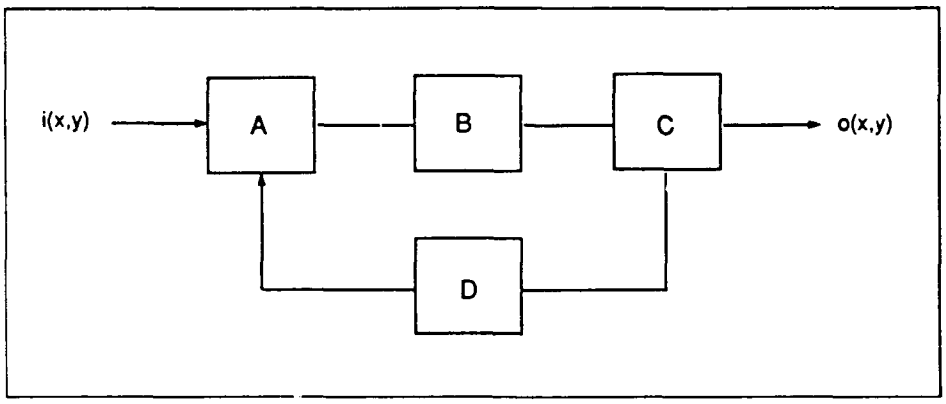

Figure 12. Block diagram of an optical feedback loop (6:312).

beams, the feedback path length must be carefully controlled in order to maintain a stable processing environment.

3.2.2 Fabry-Perot Confocal Resonator Optical Feedback System. The Fabry-Perot Confocal Resonator (FPCR) optical feedback system is shown in Figure 13.

The system consists of two Mangin mirrors, rigidly mounted in a Burleigh 6 inch resonator. Mangin mirrors were chosen because, unlike conventional spherical mirrors, they correct for spherical aberrations in non-paraxial rays (35:9). Each mirror is coated to provide 99% reflectivity over one half of its surface and 94% over the other half at a wavelength of 514.5 nm. M2, is connected to three piezo-electic crystals driven by a Burleigh DAS- 10 Data Acquisition/Stabilization system. The DAS-10, together with a ramp generator and an oscilloscope, stabilizes the spacing between the mirrors in order to control the phase difference between the input and feedback waves.

Now consider the behavior of a coherent object beam as it traverses the resonator cavity. Assume the beam enters the cavity a distance y_i below the cavity centerline as shown in Figure 14. Also assume its zero spatial frequency component is tilted with respect to the optic axis by an amount θ. If the Fourier transform of the object is imaged at point A in the first Fourier plane of the resonator, M2 will produce an inverted image at point B, or the resonator's first image plane, located in the midplane of the resonator. The image is then processed by the element $f(u,v)$

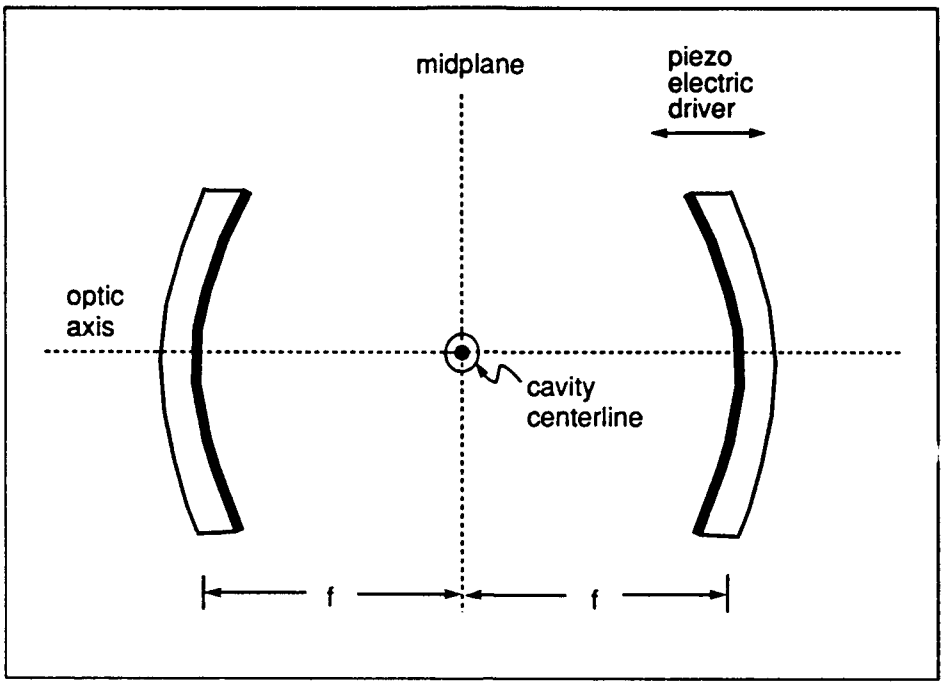

Figure 13. Fabry-Perot Confocal Resonator. Cavity centerline extends out of the paper.

and Fourier transformed by M1 to yield an inverted Fourier transform in the resonator's second Fourier plane located at point C. The beam then travels to M2 where a portion is transmitted through the low reflectivity half of the mirror to form a system output. The remainder is inverse Fourier transformed by M2, processed by the element $g(u,v)$ at point D and fed back onto the input at M1.

The spatial dimensions of the processing elements determine the separation distance between points B and D in the resonator midplane. The separation distance is a function of the input bias angle and can be determined by considering the transmission- reflection-trasmission matrix, T, formed by the input as it enters the cavity, reflects off M1 and travels to point B. Assuming the input enters the cavity a distance y_i below the cavity centerline and the mirror separation equals the radius of curvature, R, of the mirrors, the T matrix is given by (33):

$$T_R = \begin{bmatrix} 1 & R/2 \\ 0 & 1 \end{bmatrix} \begin{bmatrix} 1 & 0 \\ -2/R & 1 \end{bmatrix} \begin{bmatrix} 1 & R \\ 0 & 1 \end{bmatrix} \tag{9}$$

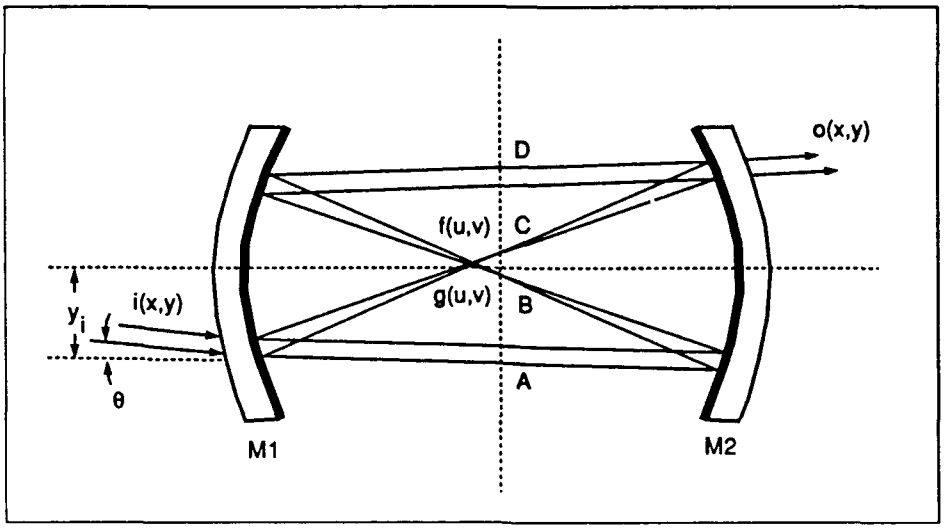

Figure 14. Round trip path taken by a beam entering the Fabry-Perot Confocal Resonator cavity. Input beam is at an angle θ to separate Fourier and image planes in midplane of resonator.

$$= \begin{bmatrix} 0 & R/2 \\ -2/R & -1 \end{bmatrix} \tag{10}$$

The location of the beam in the first Fourier plane, y_{F1}, can be found by multiplying the input position/angle vector, (y_i, θ_i) by the T matrix. Thus,

$$\begin{bmatrix} y_{F1} \\ \theta_{F1} \end{bmatrix} = \begin{bmatrix} 0 & R/2 \\ -2/R & -1 \end{bmatrix} \begin{bmatrix} y_i \\ \theta_i \end{bmatrix} \tag{11}$$

$$\Longrightarrow \quad y_{F1} = \frac{R\theta}{2} \tag{12}$$

where θ_{F1} is the angle of the beam in the first Fourier plane. Equation 12 indicates a positive input bias angle places the first Fourier plane a distance $R\theta/2$ above the centerline; while a negative input bias angle places the Fourier plane below the cavity centerline. Because points B and D are equidistant from the centerline, the separation distance between the two Fourier planes equals $R\theta$. Interestingly, note that the Fourier plane separation does not depend on the input position above or below the cavity centerline.

The coherent transfer function of the FPCR is given by

$$h = t^2 r^2 f a_i + r^4 f g a_o e^{i\beta} \tag{13}$$

where t is the amplitude transmittance of the mirrors, r is the amplitude reflectance of the mirrors, f and g are optical processing elements, β is the phase shift of the beam inside the cavity when it rejoins the input at M1, and a_i and a_o are the system input and output (5:944). Equation 13 indicates the phase shift, β, must be held constant in order to maintain a stable coherent transfer function. However, when a bundle of rays of finite size traverses the FPCR, each ray will have a slightly different path length. Path length differences in turn produce phase variations across the width of the beam that degrade the FPCR's ability to process large amounts of parallel information (8:536). Assuming these phase variations can never be completely eliminated, the goal is to find a mirror alignment that reduces them as much as possible.

Fainman et. al. developed the following expression for the phase variation across the width of a plane wave as it traverses the cavity

$$\Delta\beta(y,\theta) = \frac{2\pi}{\lambda} R \left[\frac{y^2}{R^2} \left(\frac{y^2}{R^2} + 4\epsilon - 2\frac{\theta^2}{4} \right) + \left(\frac{4\epsilon}{R} + \frac{\theta^2}{4} \right) \frac{\theta^2}{4} \right] \tag{14}$$

where R is the mirror's radius of curvature, ϵ is an incremental distance in the mirror separation, y is the distance above the cavity centerline, and θ is the input bias angle of the plane wave (8). A plot of the theoretical phase variation as a function of distance from the cavity centerline (y = 0) for several different mirror separations is shown in Figure 15.

y_{min} represents the boundary between the Fourier and image planes in the midplane of the resonator and is located a distance $R\theta$ above and below the centerline. y_{o1} is the distance to the first fringe from the cavity centerline as shown in Figure 16.

Notice that the phase variation in Figure 15 for negative values of mirror spacing, ϵ, exhibits a fairly broad extremum while the phase variation increases rapidly for positive values of ϵ. By setting the mirror spacing to a distance slightly less than the effective focal length of the mirrors, the location of the first fringe lies further from the cavity centerline than it does when the mirrors are separated by distances greater than or equal to the confocal separation. Thus, by setting the

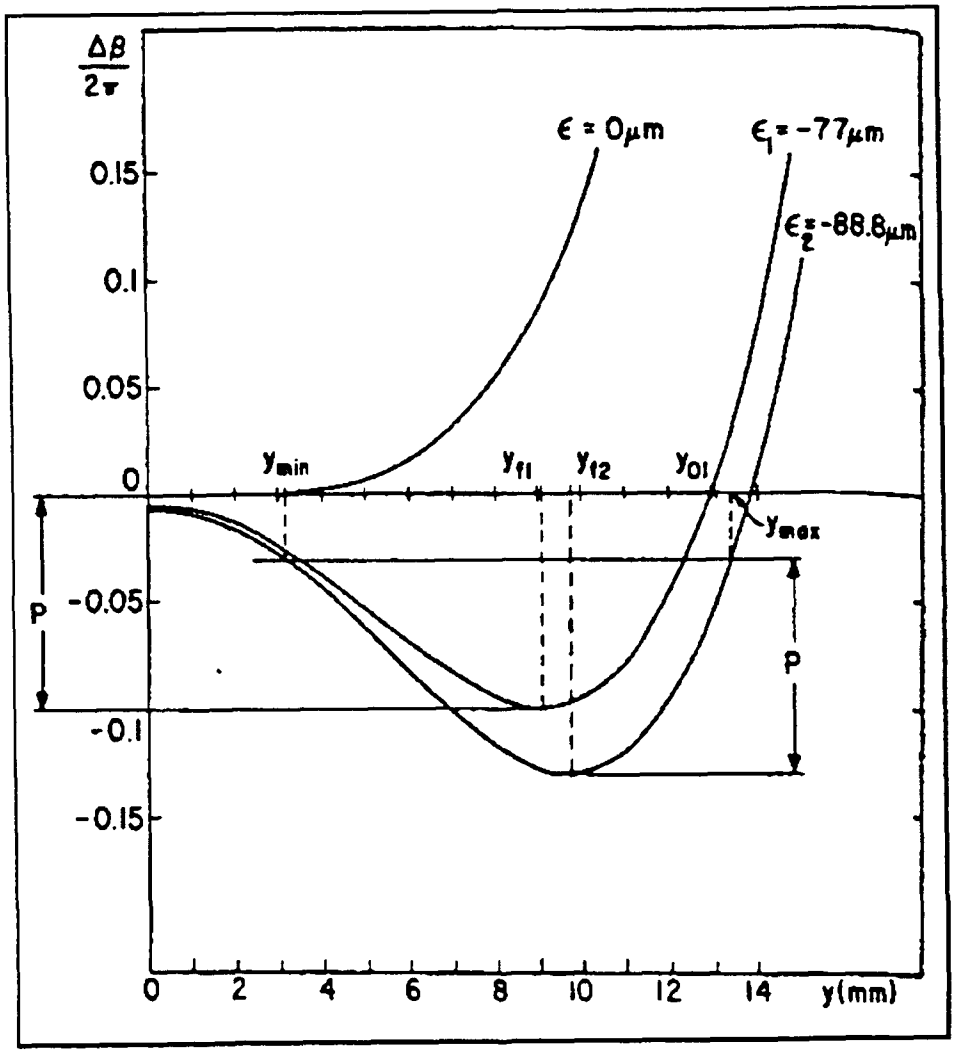

Figure 15. Phase variation, $\Delta\beta$, evaluated for different values of mirror separation. Note that negative values of ϵ (corresponding to a mirror spacing slightly less than R) reduces the phase error to p percent of 2π (8:536).

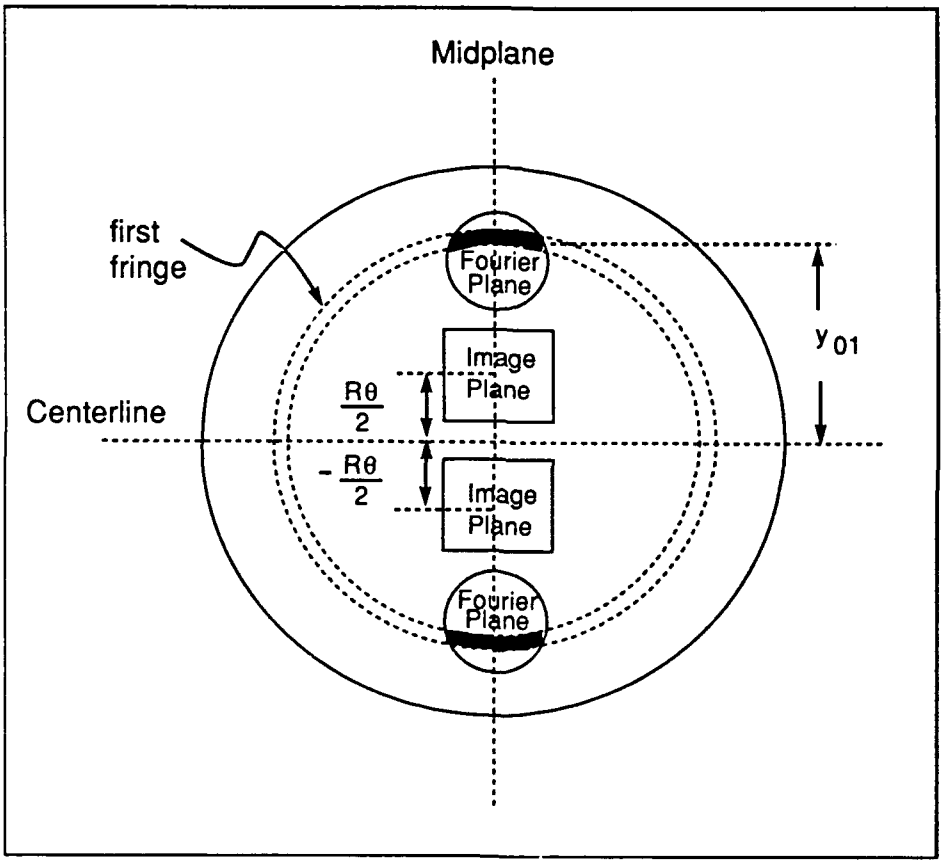

Figure 16. Fourier and image planes in a Fabry-Perot Confocal Resonator as contained in a planar slice taken through the midplane of the resonator.

mirror separation slightly less than R, one can increase the amount of information to be parallel processed in the cavity and still expect the phase across the cavity's processing environment to remain within some fixed percentage, p, of 2π as determined by the value of ϵ (8). As a result, the mirror separation of the resonator investigated in this thesis was set to a distance slightly less than the radius of the mirrors.

The FPCR described above was used to implement an optical associative memory consisting of two $BaTiO_3$ gain and thresholding elements and two $LiNbO_3$ holographic memory storage and recall devices. Early in the experimental stage of the thesis, a single $BaTiO_3$ crystal was placed in the first image plane of the FPCR in order to observe its image processing characteristics. The number of stray beams present in the FPCR due to reflections off the $BaTiO_3$ crystal made it difficult to accurately identify and observe the behavior of the various image, feedback and pump beams inside the FPCR. Because this problem is compounded when four crystals are operated simultaneously in the resonator, it was deemed best to first explore the gain and read/write behavior of the crystals in a processing environment that offered more room and flexibility. Therefore, a large, "unfolded" version of the FPCR was constructed using discrete optical components.

3.2.3 Discrete Model of a Fabry-Perot Confocal Resonator Optical Feedback System

The FPCR mirrors can be modeled by an equivalent lens waveguide consisting of four Fourier transforming lenses as shown in (Figure 17) (33). Assuming the input is imaged onto the first image plane of the FPCR, as shown in Figure 1, Fourier transforming lenses L1 through L4 in Figure 8 perform the same function as the FPCR's Fourier transforming mirrors. The feedback behavior of the resonator is simulated by using plane mirrors to direct the output of the lens waveguide back onto its input. Such a system was contructed for this thesis and is shown in Figure 44.

When a plane wave illuminates a transmission pattern located at the input image plane, the resulting wave will pass through the beamsplitter and undergo four successive Fourier transforms by lenses L1 through L4. M1 through M3 direct the feedback beam back onto the input at the beamsplitter. A portion of the internal beam exits the loop at the beamsplitter and is imaged onto a screen or camera. L1 through L4 are Fourier transforming lenses that provide two Fourier and two image planes. L1 and L4 have a focal length of 50 cm and L1 and L2 have a focal length of

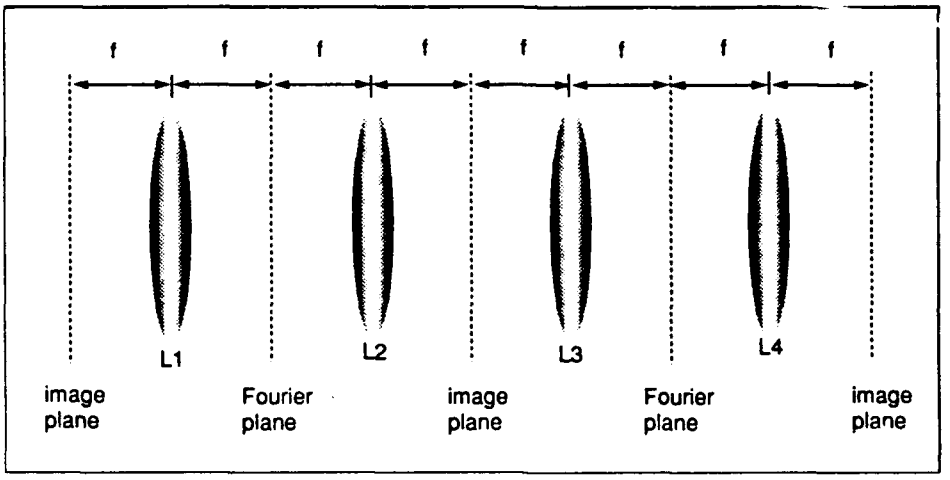

Figure 17. Equivalent lens waveguide for a single pass in a Fabry- Perot Confocal Resonator.

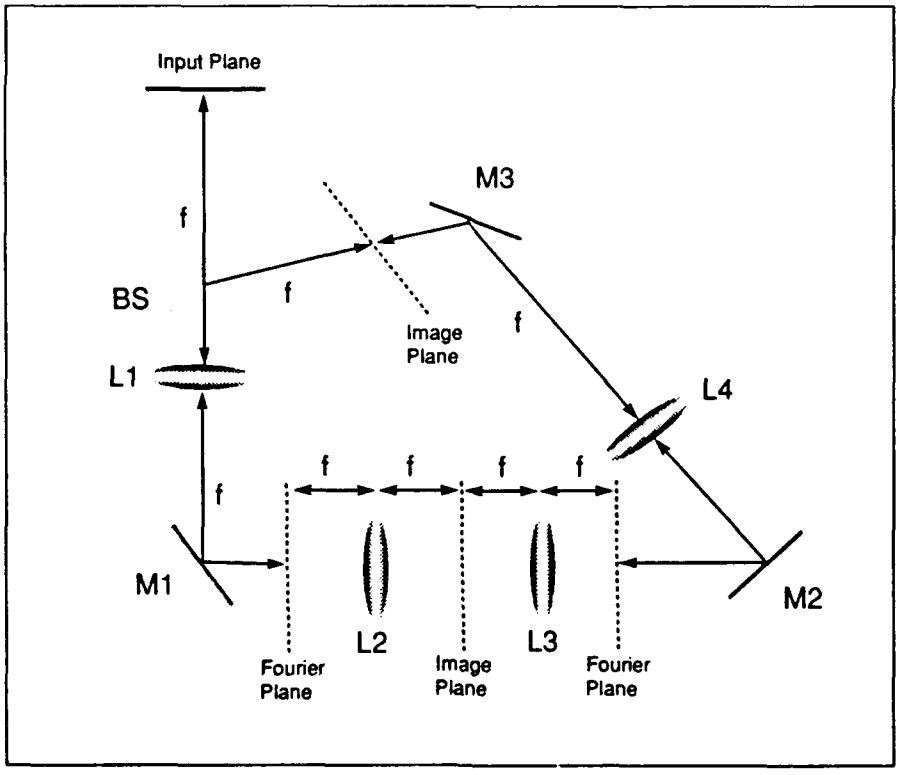

Figure 18. Optical feedback loop made from discrete components designed to simulate the behavior of a Fabry-Perot Confocal Resonator.

10 cm. M1 through M3 are plane mirrors and B1 is a 50/50 beamsplitter. All optical elements have a diameter of 5 cm and are rigidly mounted to maintain a standard beam height and to reduce vibrations that cause beam fluctuations.

The focal lengths of L1 through L4 are chosen to ensure the input and feedback beams are the same size when they combine at the beam splitter. In this case, lenses L1 and L2 reduce the size of the input object at the first image plane to 1/5 its original size (f2/f1 = 1/5). Lenses L3 and L4 restore the input to its original size at the second image plane. M3 is positioned so that the second image plane and the input image plane are equidistant from the beamsplitter (not a trivial task). A more detailed explanation of the discrete resonator's alignment procedures is provided in Chapter 4.

3.3 Two-Wave Coupling in Barium Titanate - $BaTiO_3$

Optical associative memories that employ feedback typically use gain and thresholding elements to amplify strong feedback signals and attenuate weak ones. Because of its large Pockel's coefficients, $BaTiO_3$ has exhibited small-signal gain characteristics exceeding 10^4 (26). Additionally, by reversing the crystal geometry used to achieve high gain, $BaTiO_3$ has been shown to act as a small-signal attenuator (35). Therefore, two $BaTiO_3$ crystals were used in the OAM investigated in this thesis. One crystal provided sufficient gain to overcome the losses introduced by elements in the feedback loop; while, the second crystal acted to attenuate weak feedback signals corresponding to incorrect associations made between the distorted input and each of the stored memories.

$BaTiO_3'$s ability to amplify and attenuate optical signals arises from a phenomenon known as two-wave coupling. Two-wave coupling is an energy transfer process in which energy from a pump beam is transferred to energy in a mutually coherent signal beam when both beams combine to form an interference pattern inside a photorefractive crystal. The term "photorefractive" refers to non-linear materials that exhibit changes in their refractive indices (or equivalently, their dielectric properties) when exposed to light (16:204). Both Wilson and Keppler provide a fairly detailed explanation of the process of two-wave coupling (22) (35). Therefore, this portion of the thesis will focus more on the externally controlled geometric parameters that affect gain/attenuation

performance, and refer the reader to Wilson and Keppler for a more detailed explanation of the physics of the two-wave coupling process.

3.3.1 Crystal and Beam Geometry. The gain/attenuation obtained from a photorefractive crystal depends on several variables including its material properties (e.g., Pockel's coefficients) and the intensities and geometrical alignment of the signal beam and pump beam with respect to the c- axis of the crystal. Before presenting the equation that describes two-wave coupling gain, it will be helpful to first introduce two geometrical parameters that play a significant role in the two wave coupling process: the separation angle, θ, between the internal signal and pump beams, and the internal angle, β, between the refractive index grating vector and the c+ axis.

A typical two-wave coupling geometry for a z-cut $BaTiO_3$ crystal (i.e., the c-axis lies parallel to crystal face) is shown in Figure 19. When two coherent beams separated by an angle $2\theta_{ext}$ combine inside a $BaTiO_3$ crystal as shown in Figure 19, their interference pattern modulates the index of refraction of the material so that energy is deflected in the direction of the c+ axis (in this case, from the pump to the signal beam). The interference grating vector, $\bar{k}_g = \bar{k}_1 - \bar{k}_2$, which identifies the magnitude and direction of the interference grating formed in the crystal, lies perpendicular to the bisector of the beams' internal separation angle, θ. The internal separation angle is given by

$$\theta = \frac{\alpha_1 + \alpha_2}{2} \tag{15}$$

where α_1 and α_2 are the internal angles between the normal to the crystal face and the signal and pump beams respectively. As shown in Figure 19, the interference grating vector also lies at an angle β from the c-axis of the crystal where,

$$\beta = \frac{\alpha_1 - \alpha_2}{2} \tag{16}$$

Using Snell's Law to express θ and β in terms of the crystal orientation and external beam separation angle gives

$$\theta = \frac{1}{2}\left\{\arcsin\left[sin\frac{\theta_{ext} - \gamma}{n_e}\right] + \arcsin\left[\sin\frac{\theta_{ext} + \gamma}{n_e}\right]\right\} \tag{17}$$

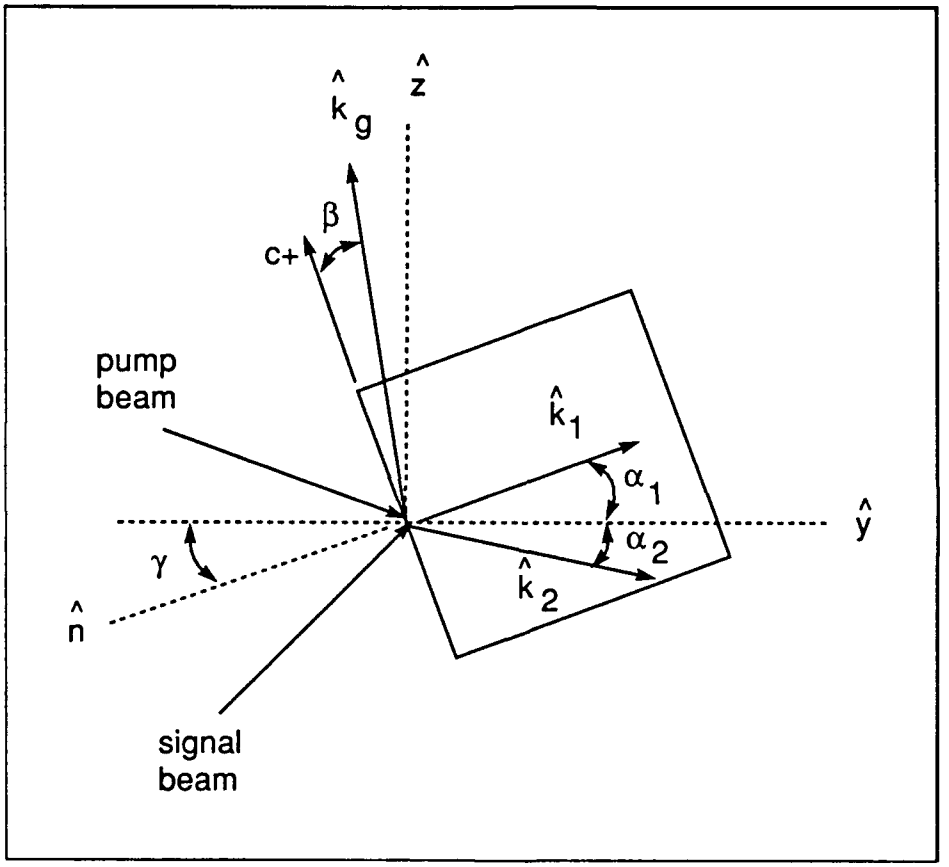

Figure 19. Two-wave coupling geometry in $BaTiO_3$. Coherent pump and signal beams interfere inside the crystal to create an interference grating, $\bar{k}_g$, perpendicular to the bisector of the two beams and at an angle β to the c+ axis. γ represents the angle between the external bisector and the normal to the crystal face.

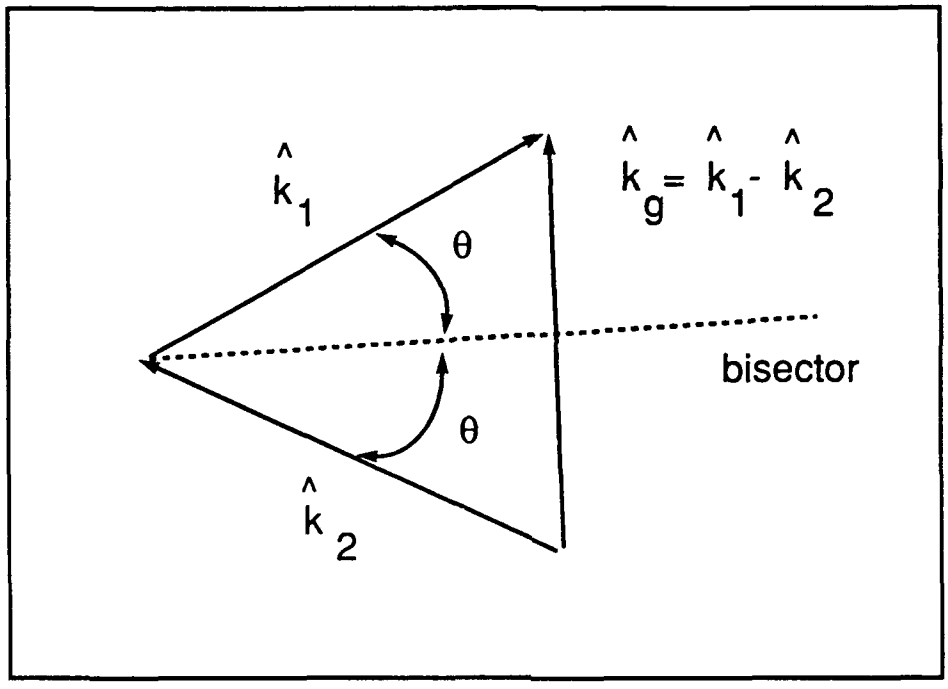

Figure 20. Grating vector formed when signal and pump beams form an interference pattern inside a photorefractive crystal.

$$\beta = \frac{1}{2}\left\{\arcsin\left[\sin\frac{\theta_{ext}-\gamma}{n_e}\right] - \arcsin\left[\sin\frac{\theta_{ext}+\gamma}{n_e}\right]\right\} \tag{18}$$

where γ is the angle between the bisector of the external signal and pump beams and the normal to the crystal face, and n is the extraordinary index of refraction of the crystal (assuming both the signal and pump beams are *extraordinarily* polarized). If θ_{ext} and γ are small, the above equations reduce to $\theta \approx \frac{\theta_{ext}}{n_e}$ and $\beta \approx \frac{\gamma}{n_e}$.

The grating vector is a function of both the internal beam separation angle, θ and the grating vector angle, β. From the geometry shown in Figure 20,

$$\sin\theta = \frac{\frac{1}{2}|\bar{k}_g|}{\frac{2\pi n}{\lambda}} \tag{19}$$

which, when rearranged, yields the following expression for the magnitude of the grating vector

$$k_g = \frac{4\pi n}{\lambda} \sin\theta \tag{20}$$

The direction of the grating vector, found by separating the vector in Figure 20 into y and z components, is given by

$$\hat{k}_g = (0, \sin\beta, \cos\beta) \tag{21}$$

3.3.2 Two-Wave Coupling Gain. The two-wave coupling gain of a photorefractive crystal is most often expressed in the literature as the ratio of the output signal with the pump beam to the output signal without the pump beam. Note that this is *not* what is typically defined as an input-output gain. Instead, this definition accounts for Fresnel reflections off the crystal faces. The gain equation most commonly found in the literature is

$$G = \frac{(1+r)\, e^{\Gamma L_{eff}}}{1 + r e^{\Gamma L_{eff}}} \tag{22}$$

where r is the intensity ratio of the input signal and pump beams, Γ is the crystal gain coefficient and L_{eff} is the effective interaction length of the signal and pump beams inside the crystal (9) (16) (11) (20) (21). Each of these three parameters will now be separately discussed to gain an insight into how the externally controlled variables r, θ and β can be manipulated to enhance crystal gain.

3.3.2.1 Intensity Ratio - r. Figure 21 was obtained by plotting Equation 22 while varying the signal to pump beam intensity ratio, r. The flat region to the left of the knee in the curve is generally referred to as the linear operating region of the crystal (i.e., a plot of the output vs input signal intensity in this region would be linear). Notice that for small r, Equation 22 reduces to

$$G_{sat} = e^{\Gamma L_{eff}} \tag{23}$$

where G_{sat} is known as the *saturated gain* condition of the crystal.

Figure 22 contains a plot of crystal gain for three different saturated gain conditions (i.e., three different values for ΓL_{eff}). These curves show that as the saturated gain increases, the knee

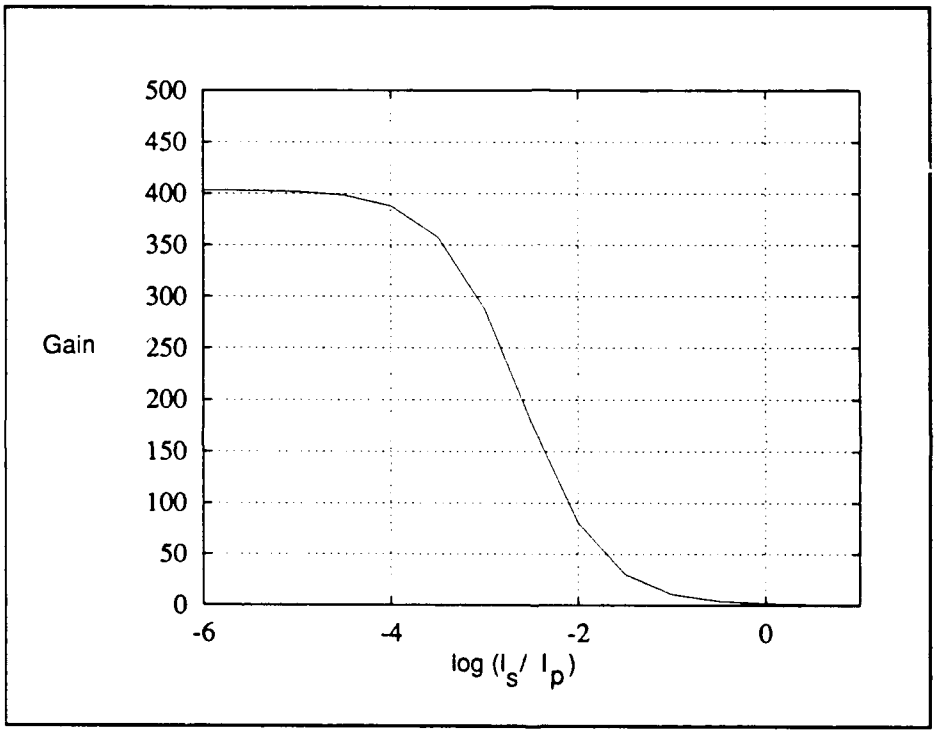

Figure 21. Typical gain profile of a $BaTiO_3$ crystal vs input signal to pump beam intensity ratio. The flat portion of the curve to the left of the knee is referred to as the linear operating region of the crystal. The plot assumes θ and β are constants.

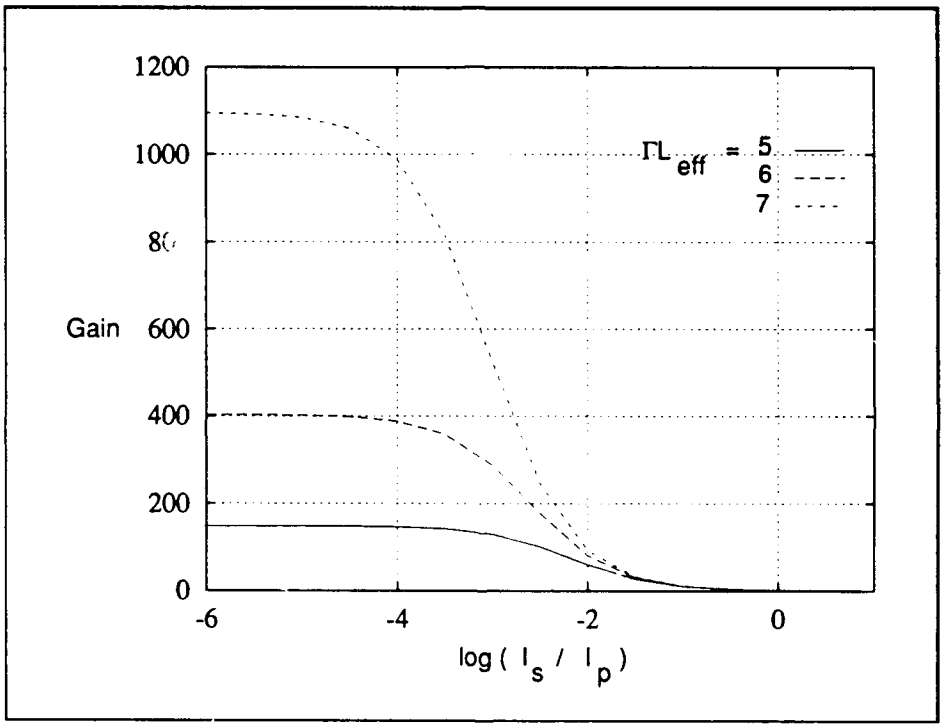

Figure 22. Gain profile of a $BaTiO_3$ crystal vs input signal to pump beam intensity ratio for three different saturated gain conditions.

in the curve shifts to the left. The knee represents the point at which the output signal intensity equals the input pump intensity. Once this condition is reached, the pump beam has transferred all the energy it is capable of transferring (called a "depleted pump" condition). Further increases in input signal intensity have no additional affect on output signal intensity (34). In the associative memory, the input signal intensity is fixed by the diffraction efficiency of the $LiNbO_3$ crystal; therefore, r is controlled by adjusting the intensity of the pump beam. To achieve maximum gain, the pump intensity is set to "bias" the $BaTiO_3$ crystal to operate in the linear, or, saturated gain, region of the gain curve.

3.3.2.2 Effective Interaction Region - L_{eff}. The effective interaction region represents the length of photorefractive material through which the signal and pump beams interact to form an interference pattern. It is typically a function of θ and β and the width of the crystal. However, for small values of θ, the effective interaction region can be approximated by

$$L_{eff} = \frac{d}{\cos\beta} \tag{24}$$

where d is the thickness of the crystal (9). Figure 23 depicts a signal and pump beam interacting as they travel through a photorefractive crystal with length d. The pump beam is significantly larger than the signal beam to ensure both beams interact through the entire length of the crystal. The gain equation depends exponentially on the effective interaction length; therefore, small changes in crystal length, either by increasing the nominal crystal width, d, or by rotating a thin crystal so the beams interact over an effectively longer crystal region, can have a dramatic effect on crystal gain.

3.3.2.3 Gain Coefficient - Γ. When the pump beam intensity is set so that the crystal is biased to operate in its saturated gain regime (i.e., small r), Equation 23 shows the intensity ratio no longer plays a role in the saturated gain profile of the crystal. Instead, assuming L_{eff} is fixed, the gain coefficient, Γ, determines the magnitude of the saturated gain. Γ, which is normally expressed in inverse millimeters, describes the amount of energy "coupled" between the pump and signal beams (9). It consists of several terms, each of which depend on β and θ. Fainman

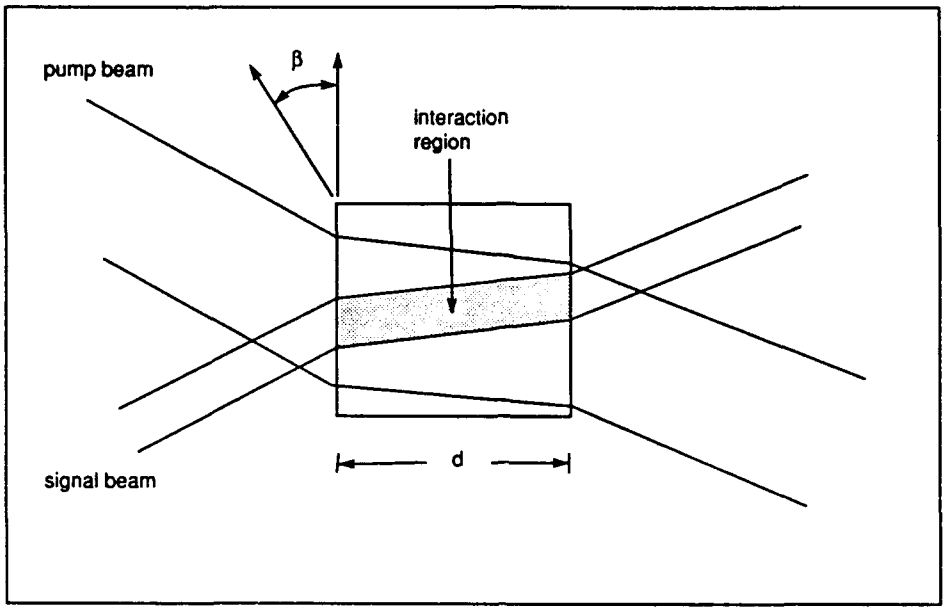

Figure 23. Interacton region formed by overlapping pump and signal beams as they pass through a $BaTiO_3$ crystal.

gives the following expression for the gain coefficient of a $BaTiO_3$ crystal,

$$\Gamma = \frac{2\pi n}{\lambda} E_{sc}\, r_{eff}\, \frac{1}{\cos\theta} \tag{25}$$

where n is the index of refraction "seen" by the signal and pump beams, λ is the wavelength, and E_{sc} is the static electric field created in the crystal in the absence of any intrinsic or applied electric fields (9). The term r_{eff} is the effective electro-optic coefficient and, for extraordinarily polarized beams, is given by

$$\begin{aligned} r_{eff} &= \frac{1}{2}\cos\beta\left[n_o^4 r_{13}\,(\cos 2\theta - \cos 2\beta)\right. \\ &+ 4n_e^2 n_o^2 r_{42} sin^2\beta \\ &+ \left. n_e^4 r_{33}\,(\cos 2\theta + \cos 2\beta)\right] \end{aligned} \tag{26}$$

where r_{ij} are the electro-optic coefficients and n_o and n_e are the ordinary and extraordinary indices of refraction (9).

The static electric field, E_{sc}, is a function of the beam and crystal geometry and can be expressed by the equation

$$E_{sc} = \frac{k_B T}{q} \frac{k_g}{1 + \left(\frac{k_g}{k_o}\right)^2} \hat{e}_s \cdot \hat{e}_p^* \tag{27}$$

where $k_B T$ is the crystal lattice energy, q is the charge of the dominant charge carrier, k_g is the magnitude of the grating vector, and $\hat{e}_s$ and $\hat{e}_p$ are unit polarization vectors for the signal and pump beams respectively (9). k_o is a material constant that depends on the available number of mobile charge carriers, N, according to

$$k_o = \left(\frac{Nq^2}{\epsilon \epsilon_o k_B T}\right)^{\frac{1}{2}} \tag{28}$$

where ϵ_o is the free space permittivity and ϵ is the effective dielectric constant of the material in the direction of the grating vector. Its value is given by $\epsilon = \hat{k_g} \cdot \bar{\epsilon} \cdot \hat{k_g}$ where $\bar{\epsilon}$ is the dc dielectric tensor of the material (9). Using the expression for k_g derived above and the dc dielectric tensor for $BaTiO_3$ given by Yariv (36:233),

$$\bar{\epsilon} = \begin{pmatrix} \epsilon_1 & 0 & 0 \\ 0 & \epsilon_2 & 0 \\ 0 & 0 & \epsilon_3 \end{pmatrix} \tag{29}$$

where $\epsilon_1 = \epsilon_2 = 3600$ and $\epsilon_3 = 135$, the effective dielectric constant in the direction of the grating vector is then

$$\epsilon = \epsilon_2 \sin^2\beta + \epsilon_3 \cos^2\beta \tag{30}$$

From Figure 19, the unit polarization vectors are

$$\hat{e}_s = (0, -\sin\alpha_1, \cos\alpha_1) \tag{31}$$

$$\hat{e}_p = (0, \sin\alpha_2, \cos\alpha_2) \tag{32}$$

which, since $\hat{e}_p$ is real (i.e., $\hat{e}_p = \hat{e}_p^*$), yield the following expression for the dot product of the unit polarization vectors

$$\hat{e}_s \cdot \hat{e}_p^* = \cos\alpha_1 \cos\alpha_2 - \sin\alpha_1 \sin\alpha_2$$

$$= \cos(\alpha_1 + \alpha_2)$$

$$= \cos 2\theta \tag{33}$$

A three dimensional plot of Γ vs θ and β is shown in Figure 24. The plot was obtained by inserting Equations 26 through 33 into Equation 25 and varying θ and β from $O°$ to 40° and 0° and 90° respectively. The crystal was assumed to be ideal and the following "typical" values provided by Fainman were used for material and beam constants,

$n_e = 2.424$

$n_o = 2.488$

$\lambda = 514.5 \cdot 10^{-9} m$

$T = 300K$

$k_B = 1.3807 \cdot 10^{-23} JK^{-1}$

$q = 1.6 \cdot 10^{-19}$ coulombs

$\epsilon_2 = 3600 Fm^{-1}$

$\epsilon_3 = 135 Fm^{-1}$

$r_{13} = 8 \ \ 10^{-12} mV^{-1}$

$r_{42} = 820 \cdot 10^{-12} mV^{-1}$

$r_{33} = 28 \cdot 10^{-12} mV^{-1}$

$N = 2 \cdot 10^{22} m^{-3}$

The curve of $\Gamma(\theta, \beta)$ monotonically increases to a peak located near $\theta = 2^o$ and $\beta = 45^o$, indicating the crystal exhibits its highest theoretical gain when the grating vector and internal beam separation angles are set at these values. The curve decreases monotonically as θ and β move away from this region due to poor coupling with the r_{42} coefficient. This plot agrees with the curves obtained by Fainman et. al. (9).

Another useful plot for visualizing the gain characteristics of the crystal is shown in Figure 25. The curves in Figure 25 also agree with those provided by Fainman (9). Obtained by varying β in Equation 25 for constant values of θ, the curves clearly illustrate how the theoretical gain

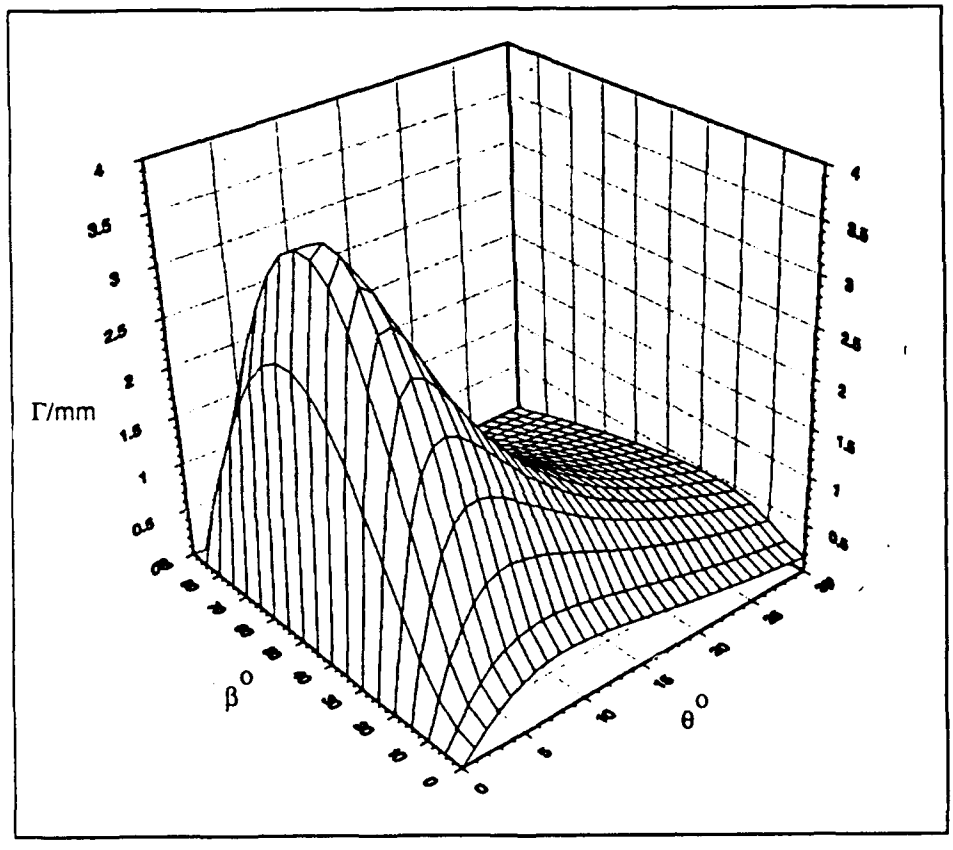

Figure 24. Plot of ideal $BaTiO_3$ crystal gain coefficient, Γ vs grating vector angle, β, and internal beam separation angle, θ. Note the sharp peak in the curve for small values of θ and $\beta \approx 45^o$.

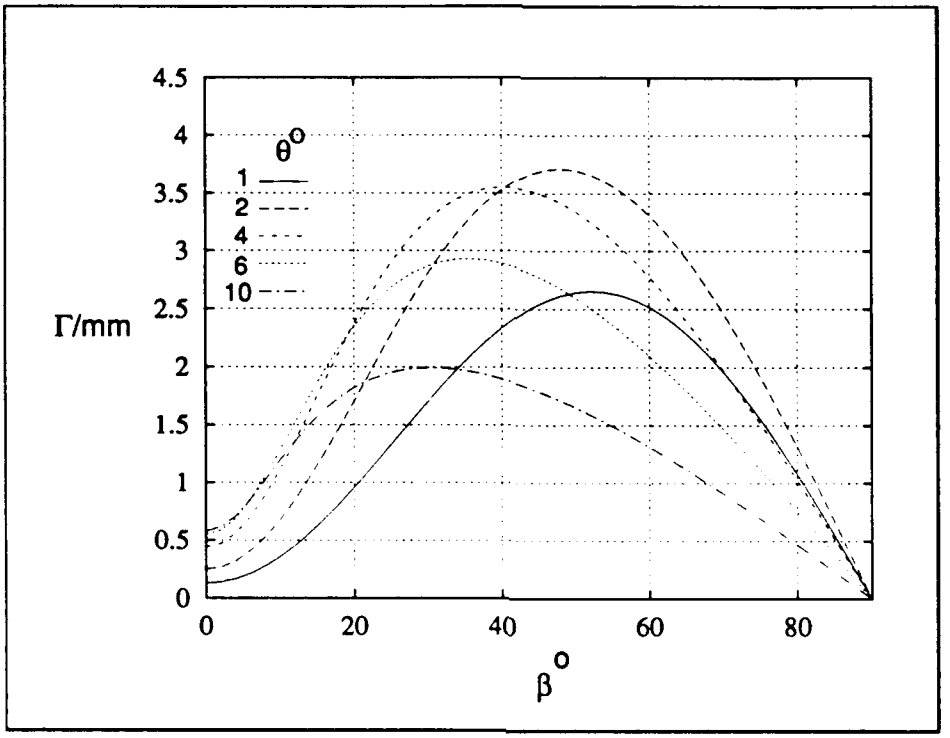

Figure 25. Plot of ideal $BaTiO_3$ crystal gain coefficient, Γ, vs grating vector angle, β, for various values of internal beam separation angle, θ.

coefficient of an ideal crystal varies as a function of the grating vector angle (i.e., the "rotation" of the crystal). Again, the peak theoretical gain occurs for small internal separation angles ($\theta \approx 2^o$) and a grating vector angle of approximately 45 degrees. However, as Keppler noted, values of β greater than approximately 20 degrees "could not be achieved with a z-cut crystal due to the high index of refraction, and, consequently the large bending of the input light beams" (22:18). In other words, when the crystal is rotated far enough to achieve large values of β, the high index of refraction causes the input beams to "bend" and exit the crystal through its sides. Thus, Wilson and Keppler were led to investigate the gain properties of 45 degree cut crystals (i.e., the optic axis lies at a 45 degree angle from the crystal face). They found the gain profile of these crystals was time dependent, where the gain reached a large peak value during the first few seconds of operation, and then quickly decayed until reaching a steady state gain level much lower than the peak value. The results obtained using a 45 degree cut crystal in the discrete model of the FPCR associative memory are contained in Chapter 4.

3.3.3 Attenuation. The expression for two-wave coupling gain given by Equation 25 was derived from the appropriate charge transport and coupled wave equations used to model the two-wave coupling process (21). Two important equations that result from this derivation describe the change in intensity of the signal beam, I_s, and pump beam, I_p, as they propagate through a photorefractive crystal. Using the notation previously developed in this chapter, Vogel gives these equations as

$$I_p(d) = \frac{I_o}{1 + re^{\Gamma L_{eff}}} \tag{34}$$

$$I_s(d) = \frac{I_o}{1 + \frac{1}{r}e^{-\Gamma L_{eff}}} \tag{35}$$

where $I_o = I_s(0) + I_p(0)$, $r = I_s(0)/I_p(0)$, $I_s(0)$ is the input signal intensity, and $I_s(d)$ is the pumped output signal intensity (34). Both equations assume 1) their are no absorption losses as the beams travel through the crystal and 2) the c+ axis points in the direction of the output signal beam.

Equation 22 was obtained by dividing Equation 35 by the unpumped output signal intensity for a crystal geometry in which the c+ axis points in the direction of the output signal beam. Now, however, consider the opposite crystal orientation, where the c+ axis points in the direction of the output pump beam as shown in Figure 27. The direction of the c+ axis in this geometry causes energy to transfer from the signal to the pump beam. Thus, the signal now behaves like a pump beam and the pump behaves like a signal beam. As before, the signal gain can be determined by dividing the pumped output signal by the input signal. However, Equation 34, rather than Equation 35, now models the behavior of the signal beam, so that the signal gain (or, more precisely, the signal attenuation) is given by

$$\begin{aligned} G &= \frac{I_s(d)}{I_s(0)} \\ &= \frac{I_o}{I_s(0)\,(1 + re^{\Gamma L_{eff}})} \end{aligned} \tag{36}$$

To the best of this author's knowledge, this relationship, hereafter referred to as the "attenuation equation," is not explicitly stated in the current two-wave coupling literature. It is plotted in Figure 27 as a function of the intensity ratio between the input signal and pump beams, r. A somewhat similar plot is provided by Wilson, but he does not explain how he obtained it

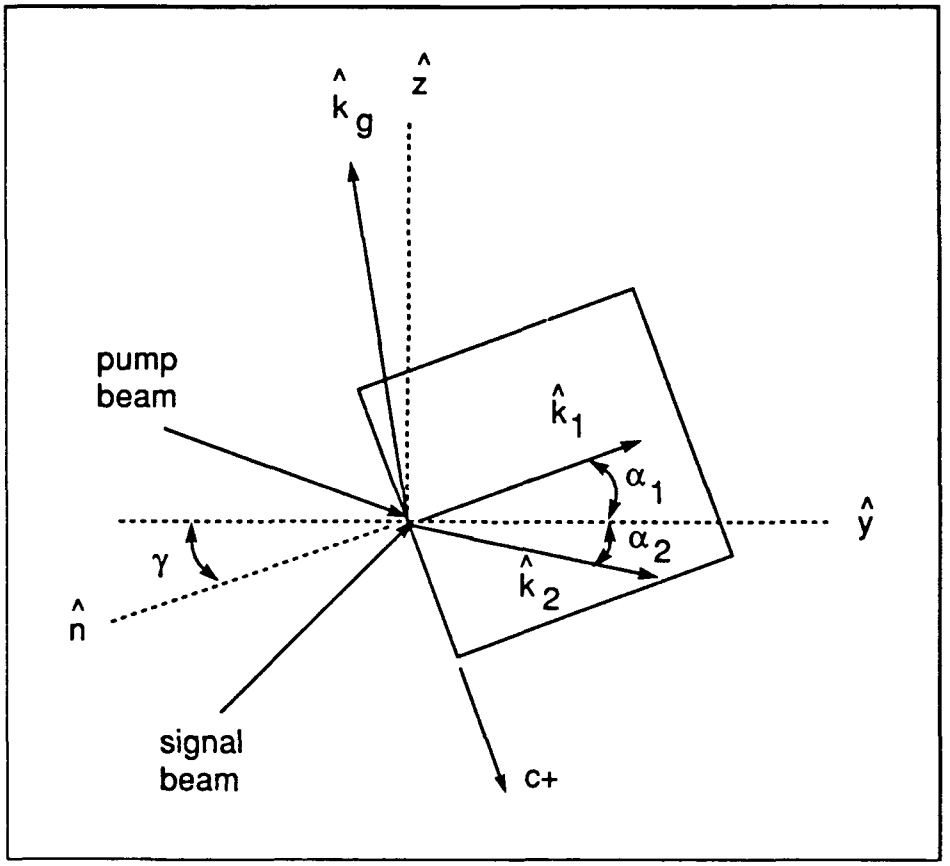

Figure 26. $BaTiO_3$ crystal geometry for small signal attenuation. Note the c+ axis points towards the output pump beam.

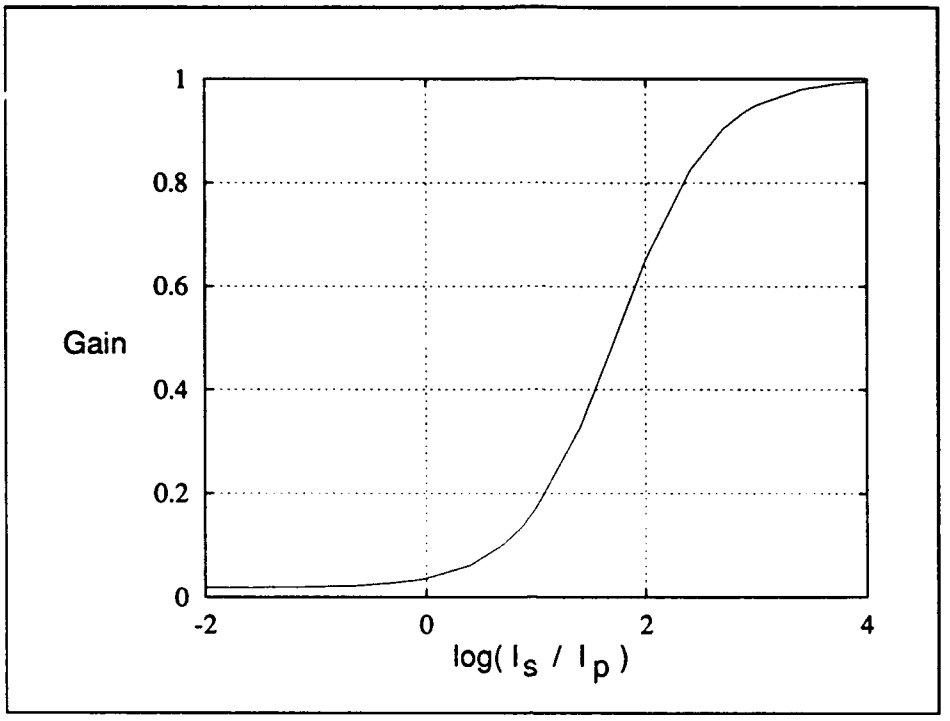

Figure 27. Signal gain for the crystal geometry in which c+ axis points towards output pump beam. In this geometry, small signals are attenuated ($G < 1$) and large signals are passed unattenuated ($G \approx 1$.

(35:59).

When the signal intensity is small compared to the pump intensity, a large percentage of the signal energy relative to its total energy is transferred to the pump. Under this condition, the gain is small ($G < 1$), or, equivalently, the attenuation is large. When the signal intensity is large compared to the pump intensity, more energy is transferred from the signal to the pump than in the small signal condition; however, *as a percentage of the total signal energy, the energy transferred from the signal to the pump beam is relatively small.* Thus, the gain under the large signal condition is large ($G \approx 1$) while the attenuation is small. In other words, small signals are attenuated as they pass through the crystal while large signals pass relatively unattenuated.

The location of the large and small signal attenuation conditions in Figure 27 depend on the intensity of the pump beam. Large pump intensities shift the curve to the right, while low pump intensities shift it to the left. Thus, in the associative memory, the average signal intensity of the

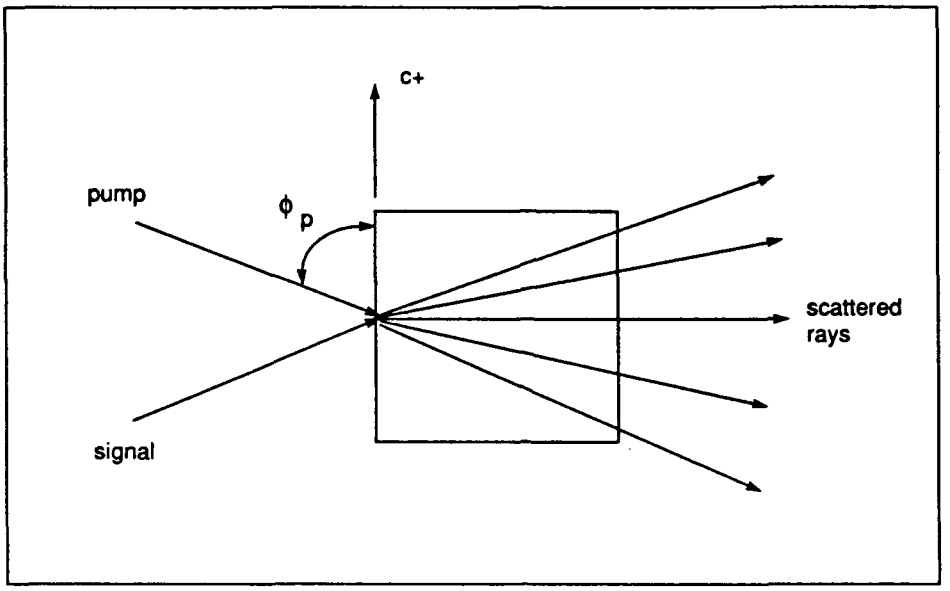

Figure 28. Beam fanning in a $BaTiO_3$ crystal. Impurities in the crystal scatter high intensity pump beam rays which are amplified through 2-wave coupling phenomenon.

strong and weak feedback beams must be accurately predicted to determine how to "bias" the pump to ensure strong signals are allowed to pass and weak signals are attenuated.

3.3.4 Beam Fanning A portion of the energy in a single beam passing through a photorefractive crystal is scattered out of the beam before it reaches the output face of the crystal. This phenomenon, known as beam fanning, removes useful energy from a two-wave coupled pump beam, and can severely degrade the quality of an amplified object pattern. Although the precise mechanism responsible for beam fanning is unknown, many researchers believe the scattering effect is caused by impurities or imperfections in the crystal (22). Keppler reviews the topic of beam fanning in some detail, therefore this discussion will focus only on those aspects of beam fanning that affect the operation of the associative memory.

When a single beam passes through a $BaTiO_3$ crystal, a percentage of the energy contained in the beam is scattered in many different directions as shown in Figure 28. Each ray in the scattered portion of the pump beam is coherent with the remainder of the pump beam and, through the process of two-wave coupling, is amplifed before leaving the crystal. The amount of amplification, or gain, depends on the direction the scattered ray is traveling. Assuming the

angle of the pump beam relative to the c+ axis is fixed at some value ϕ_p (as shown in Figure 28), each scattered ray traveling at an internal angle θ_{ray} to the pump will have a unique angle β_{ray} determined by (34)

$$\beta_{ray} = \phi_p + \theta_{ray} - 90^o \tag{37}$$

If the direction is such that the angles β_{ray} and θ_{ray} lie in the high gain region of the three dimensional gain profile in Figure 24, the scattered ray will be significantly amplified. This has two important consequences for the associative memory. First, assuming a signal beam is also passing through the crystal with θ_{signal} and β_{signal} set to achieve high signal gain, the scattered, amplified noise combines with the amplified signal and degrades the signal-to-noise ratio of the output beam. When the output beam is then used to read out holographic memories stored in a $LiNbO_3$ crystal, the beam fanning noise accelerates the erasure of the stored memories. Second, when energy is fanned out of the pump beam, less energy is available to provide useful gain to the signal. High signal gain is imperative in an associative memory in order to overcome losses in the feedback process and to sustain resonant behavior.

No method was found during the course of this thesis, either experimentally or in the literature, for eliminating or even reducing beam fanning noise in a less than perfect crystal. However, its effect on the erasure of holographic gratings was lowered by blocking a large portion of the stray beam fanning noise leaving the $BaTiO_3$ gain crystal. The modification to Wilson's proposed associative memory architecture required to block the noise is explained more fully in Chapters 4 and 5.

3.4 Holographic Storage and Recall in Iron doped Lithium Niobate - $Fe : LiNbO_3$

An associative memory must have mechanisms for storing and retrieving associated patterns. In an optical associative memory, pattern storage and recall are typically accomplished with the aid of holograms. In the past, holograms were typically made from photographic plates which had to be removed and carefully reinserted each time a memory was added or deleted from the associative memory. Modern associative memories achieve memory storage and recall with volume holograms made from photorefractive materials. Volume holographic material, such as the $LiNbO_3$ crystals used in this thesis, offer several advantages over photographic plate holograms

including dynamic memory storage, and greater storage capacity (28). Because pattern storage and recall in $LiNbO_3$ has already been extensively investigated by Frye (13), no attempt will be made here to duplicate his efforts. Instead, this section will review some of Frye's key theory and results insofar as they help the reader understand the operation of the F-OAM.

3.4.1 Memory Storage in a Volume Hologram. An architecture for recording a Fourier space volume hologram is shown in Figure 29. The arbitrary input pattern, $v(y,z)$, and its associated reference delta function, $r(y,z)$, are transformed from object space to Fourier space by L1. Assuming the input pattern is arbitrary and the reference beam is a delta function, the beams at the crystal face can be expressed by

$$\bar{V}(f_y,f_z) = \mathcal{F}\{v(y,z)\} = V(f_y,f_z)e^{-j2\pi\alpha f_z} \tag{38}$$

$$R(f_y,f_z) = \mathcal{F}\{r(y,z)\} = Ae^{+j2\pi\beta f_z} \tag{39}$$

where the time factor, $e^{j\omega t}$, has been suppressed, A is a constant amplitude, α and β are spatial frequencies given by

$$\alpha = \frac{\sin\theta}{\lambda} \tag{40}$$

$$\beta = \frac{\sin\zeta}{\lambda} \tag{41}$$

and θ and ζ are the directional angles of the object and reference beam respectively. A directional "bias" was added to the beams to simulate conditions in the F-OAM where the input beams enter off axis in order to separate the Fourier and image domains in the resonator's midplane.

When a coherent object and reference beam combine inside a $LiNbO_3$ crystal, the process by which the holographic grating is formed is identical to the grating formation process responsible for two-wave coupling in $BaTiO_3$. The object and reference beams combine to form an interference pattern inside the crystal. The interference pattern causes charges to migrate which creates an internal electric field. The internal field modulates the crystal's indices of refraction via the electro-optic effect which in turn creates a holographic grating in the crystal. Frye has shown the

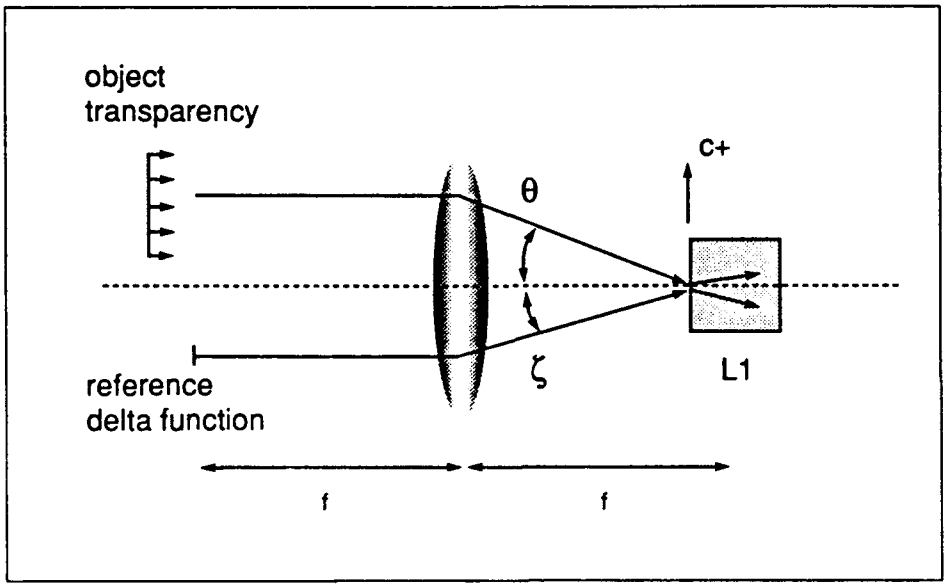

Figure 29. Crystal and beam geometry used to form holographic gratings in a $LiNbO_3$ crystal.

complex transmittance of single object hologram formed by this process is

$$\begin{aligned} T &= 1 + j\gamma\left(|R|^2 + |\bar{V}|^2 + R^*\bar{V} + R\bar{V}^*\right) \\ &= 1 + j\gamma\left(|R|^2 + |\bar{V}|^2 + AVe^{-2\pi(\beta+\alpha)f_s} + AV^*e^{+2\pi(\beta+\alpha)f_s}\right) \end{aligned} \tag{42}$$

where γ is a proportionality constant related to the diffraction efficiency of the grating (explained later), $*$ denotes complex conjugaton, and the coordinate system notation has been dropped for convenience (13).

Now consider a volume hologram containing M memories. If the memories were recorded using an angle multiplexing scheme wherein each memory is paired with a unique reference beam, the complex transmittance of the crystal is (13)

$$\begin{aligned} T &= 1 + j\sum_{k=1}^{M}\gamma^k\left(\left|R^k\right|^2 + \left|\bar{V}^k\right|^2 + R^{k*}\bar{V}^k + R^k\bar{V}^{k*}\right) \\ &= 1 + j\sum_{k=1}^{M}\gamma^k\left(\left|R^k\right|^2 + \left|\bar{V}^k\right|^2 + A^kV^ke^{-2\pi(\beta^k+\alpha)f_s}\right. \\ &+ \left. A^kV^{k*}e^{+2\pi(\beta^k+\alpha)f_s}\right) \end{aligned} \tag{43}$$

where the directional bias of the M object beams was held at a constant angle θ and the spatial frequency of each reference beam was varied as

$$\beta^k = \frac{\sin \zeta^k}{\lambda} \tag{44}$$

3.4.2 Memory Retrieval from a Volume Hologram.

Suppose now that a crystal containing M memories is illuminated by the object beam carrying the $k$oth object pattern stored in the crystal. If the memories were recorded in the crystal as shown in Figure 30 (i.e., the c+ axis points in the direction of the output reference beam), the crystal grating corresponds to the fifth term in Equation 43. The fourth term does not satisfy the Bragg scattering constraint and will not deflect energy from the input beam (13:35). Thus, concentrating our attention on the fifth term only, the field just past the crystal is given by

$$\begin{aligned} E'_{out} &= T \cdot E_{in} \\ &= V^{ko} e^{-j2\pi\alpha f_x} j \sum_{k=1}^{M} A^k V^{k*} e^{+2\pi(\beta^k+\alpha)f_x} \\ &= \gamma^{ko} \left|V^{ko}\right|^2 A e^{+j2\pi\beta^{ko}} + j \sum_{k\neq ko} A V^{k*} V^{ko} e^{+2\pi\beta^k f_x} \end{aligned} \tag{45}$$

The first term in Equation 45 represents a scaled version of the reference beam used to record the $k$oth object. The additional terms represent the remaining reference beams used in the angle multiplex recording process. The magnitude of each reference beam is determined by the strength of the interconnection formed between the $k$oth object and the kth grating as defined by the proportionality constant γ^k. In an ideal hologram, γ^{ko} would equal unity and and $\gamma^{k\neq ko}$ would equal 0.

In order to recreate the reference or object patterns stored in the crystal, the field just past the crystal must be Fourier transformed. Thus, using L2 in Figure 30 as a Fourier transforming lens, the output of the holographic recall process will consist of M recreated reference patterns (in this case, delta functions), each scaled in intensity and spread over a finite area. To see this more clearly, consider the "shorthand" description of the recall process. Assuming the stored grating is

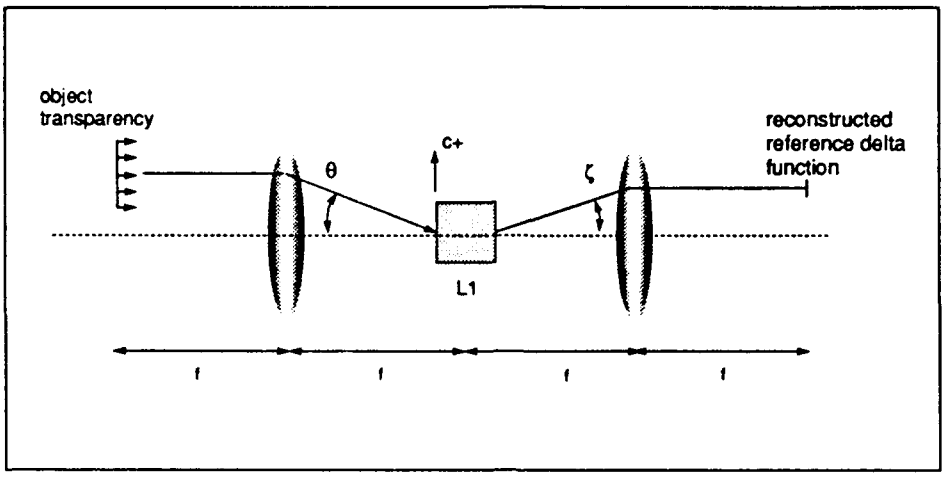

Figure 30. Crystal and beam geometry used to recreate reference pattern stored as a holographic gratings in a $LiNbO_3$ crystal.

described by $T = \gamma^k R^k V^{k^*}$, the field in the output object plane is given by

$$\begin{aligned} E_{out} &= \mathcal{F}\{E'_{out}\} \\ &= \gamma^{ko} r^{ko} * \left(v^{ko} \star v^k\right) + \sum_{k \neq ko} \gamma^k r^k * \left(v^{ko} \star v^k\right) \end{aligned} \tag{46}$$

where $*$ and $\star$ denote convolution and correlation respectively. Assuming the reference patterns are delta functions, the output plane then consists of M delta functions separated by an amount $\beta^k \lambda f$ (15:177). The correlation between the input object pattern and each of the stored object patterns acts as a point spread function that imposes a finite width (noise) on each delta function. The point spread function in the first term in Equation 46 is considered auto-correlation noise, while the remaining terms are treated as cross-correlation noise (25).

Goodman has shown the width of the noise associated with each correlation term equals the sum of the widths of the input object pattern, $\bar{v}^{ko}(y, z)$, and each stored object pattern, $\bar{v}^k(y, z)$. As shown in section 3.5, this width plays an important role in determining the minimum required separation angle between each plane wave reference beam, and ultimately, the maximum number of object patterns that can be stored in the F-OAM.

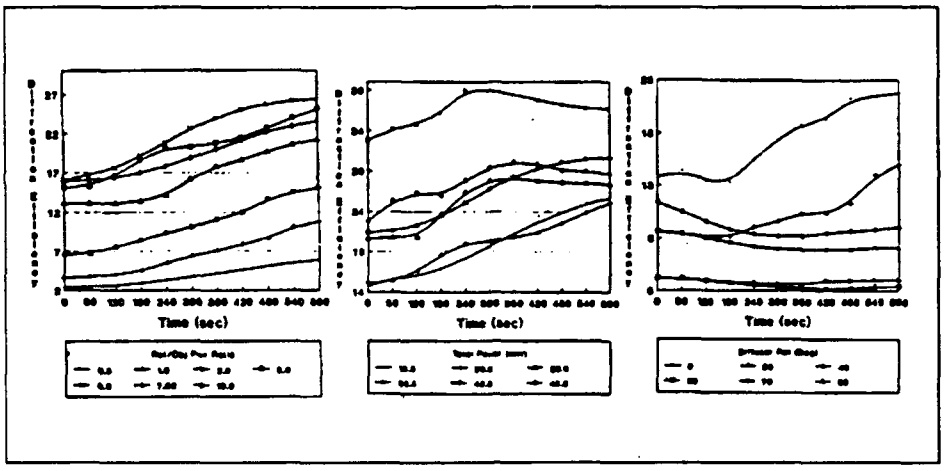

Figure 31. Results of diffraction efficiency experiments performed by Frye for a) reference to object beam power ratio b) total incident power, and c) read beam polarization (13)

3.4.3 Diffraction Efficiency. The term γ^k present in the above equations, in a general sense represents the diffraction efficiency of the kth holographic grating. That is, if the $k$oth object pattern illuminates the crystal, γ^{ko} represents the amount of energy the $k$oth grating deflects in the direction of the $k$oth reference beam. Frye investigated the diffraction efficiency of a 0.015% iron doped $LiNbO_3$ crystal with respect to three input beam parameters: 1) the incident reference to object beam power ratio, 2) the total incident power, and 3) the polarization of the object beam. His results are contained in Figure 31.

Frye obtained the results in Figure 31 by recording his holograms using the geometry shown in Figure 29, where the crystal is oriented so that the c^+ axis is perpendicular to the bisector of the internal object and reference beams and pointed in the direction of the output reference beams. After recording a hologram, he would illuminate the crystal with the object beam used in the recording process and measure, over time, the energy diffracted in the reference beam direction. Defining the diffraction efficiency of a grating as the power diffracted in the original reference beam direction divided by the power of the incident object beam, Frye achieved three important results (13:23). First, the optimum input object-to- reference beam power ratio is 6-to-1. Second, the optimum total incident power is 36.5 mW. And third, the polarization of the read beam has a significant effect on diffraction efficiency and should be extraordinarily polarized to

achieve maximum diffraction efficiency. These parameters were used as guidelines throughout the experimental portion of this thesis.

Frye also investigated the diffraction efficiency of multiple objects stored in a $Fe : LiNbO_3$ crystal. Three different objects were stored and their diffraction efficiencies were measured by successively illuminating the crystal with each object pattern and measuring the diffracted power in the object's unique reference beam direction. Frye achieved his best results using a "time reduction" storage technique in which the recording time of each successive hologram was reduced. The first hologram was stored for 60 seconds, the second was stored for 40 seconds and the third was stored for 20 seconds. However, experimental results showed the diffraction efficiency of the first object stored in the crystal was significantly larger than that of the second object which in turn was larger than the third object (13:51).

In order for an associative memory to correctly identify the stored object pattern that most closely resembles a distorted input pattern, the diffraction efficiency of each stored object grating must be approximately equal. Although Frye's time reduction storage method led to improved diffraction efficiencies for subsequently stored holograms, it did not yield equal diffraction efficiencies for all stored objects. A time storage method was also used by Psaltis et. al. to record multiple object holograms in $LiNbO_3$. And, unlike Frye's exposure time schedule, which appears to be somewhat arbitrary, Psaltis' time schedule is derived from a mathematical expression for the diffracted amplitude of the kth object stored in a crystal (28). Maniloff has demonstrated this technique is capable of yielding at least 10 holograms with equal diffraction efficiencies in a $Fe : LiNbO_3$ crystal.

Letting A^k be the amplitude of the kth recorded hologram, Psaltis assumes that after a total of M exposures,

$$A^k = A_o \left[1 - \exp\left(\frac{-t^k}{\tau_r}\right)\right] \exp\left(-\sum_{k'=k+1}^{M} \frac{t_{k'}}{\tau_e}\right) \tag{47}$$

where A_o is the saturation amplitude of a hologram recorded in the crystal, t^k is the exposure time of the kth hologram, τ_e is the crystal's characteristic erasure time constant and τ_r is the crystal's characteristic recording time constant (28:1756). Both constants can be determined by "observing the dynamics of the recording and erasure processes" (24:228). The time schedule used to achieve equal diffraction efficiencies for each of M holograms stored in the crystal can be

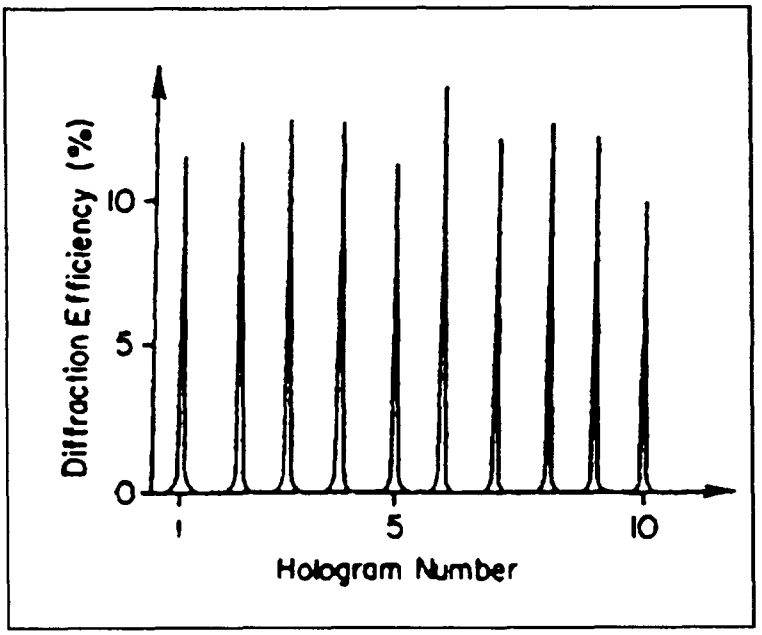

Figure 32. Maximized diffraction efficiencies for 10 plane-wave holograms stored in a 0.005 percent Fe doped $LiNbO_3$ crystal. (24:228)

found by setting the amplitude of the kth recorded hologram equal to the amplitude of the $k+1$th recorded hologram. Thus (24),

$$\left[1-\exp\left(\frac{-t_{m+1}}{\tau_r}\right)\right]=\left[1-\exp\left(\frac{-t^k}{\tau_r}\right)\right]\left[\exp\left(\frac{t_{m+1}}{\tau_e}\right)\right] \tag{48}$$

If the erasure and recording characteristic time constants are equal, and $t^k >> t_1$, Psaltis has shown the solution to the above equation for the exposure time of the kth hologram is

$$t^k=\tau_e \ln\left(\frac{k}{k-1}\right) \tag{49}$$

for $k > 1$ (28:1757). For $\tau_e \neq \tau_r$, the time schedule, t^k, can be determined through a numerical solution of Equation 49 (24:228). Maniloff was able to store 10 holograms in a 0.005 percent Fe doped $LiNbO_3$ crystal with roughly a 10 percent diffraction efficiency for each hologram. His results are shown in Figure 32. The storage time schedule developed for the $LINbO_3$ crystals used in this thesis is based on Psaltis' approach and is discussed further in Chapter 4.

3.5 *A Fourier Optics Model for the Fabry-Perot Confocal Resonator Optical Associative Memory*

This section seeks to combine the theory behind the operation of each component described in the previous three sections into a mathematical model that describes the operation of the F-OAM. The section begins with a brief, macroscopic view of the F-OAM in order to familiarize the reader with the general principles underlying its operation. The overview is followed by a more detailed analysis of the F-OAM in an effort to develop a Fourier optics model that suitably describes its operation. Finally, the model is compared to the inner-product implementation of Hopfield's neural network associative memory as discussed in Chapter 2.

3.5.1 Operational Overview. The F-OAM architecture investigated in this thesis is illustrated in Figure 33. It consists of two $Fe : LiNbO_3$ crystals, L1 and L2, that form a holographic interconnect matrix between the F-OAM's input and output. The object patterns stored in L1 and L2 are identical. Two $BaTiO_3$ crystals, B1 and B2, serve respectively as gain and thresholding devices. B1 is biased to operate in its saturated gain regime. B2 is aligned to attenuate weak signals and pass strong signals. Spatial filters (pinholes) placed in the midplane of the resonator are arranged to pass only the high intensity peaks associated with correlations between the input object and each of the objects stored as holograms in L1.

The architecture shown in Figure 33 is similar, but not identical to the architecture proposed by Wilson (35). In Wilson's architecture, the location of crystal B1 and B2 were reversed. However, after xperimenting with Wilson's configuration in the discrete optical associative memory, it was discovered placing the attenuation crystal before L2 did not provide enough signal gain to read out holograms stored in L2. Thus, the crystals were placed in the configuration shown here to take advantage of the high gain offered by B1.

The operation of the F-OAM is initiated when the Fourier transform of a distorted object (e.g., noisy, incomplete) is imaged onto L1. The holographic gratings stored in L1 produce wavefronts traveling in the direction of the object beam and in the direction of each of reference beams used in the recording process. The wavefronts traveling in the object beam direction are blocked, and the remaining beams are allowed to travel to the midplane of the resonator after undergoing a Fourier transformation by M2. If M holograms were stored in L1, the Fourier transformation yields M reference beams. The intensity of each beam is proportional to the

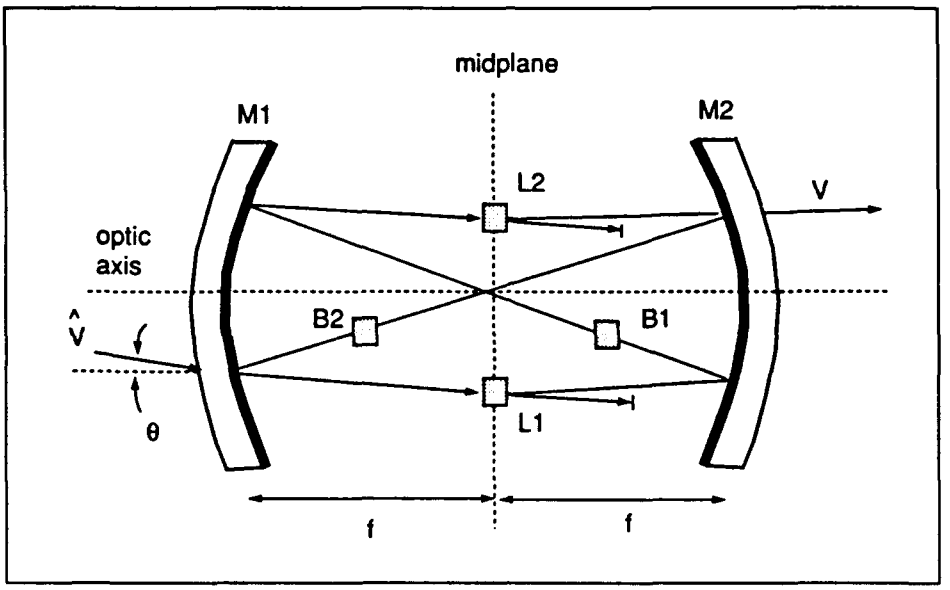

Figure 33. Fabry-Perot Confocal Resonator Optical Associative Memory. L1 and L2 are $LiNbO_3$ crystals, B1 and B2 are $BaTiO_3$ crystals.

degree of correlation between the input pattern and the object pattern recorded at that reference beam angle; therefore, the brightest beam corresponds to the strongest correlation. Each beam is then equally amplified by the saturated $BaTiO_3$ crystal, B1. Next, a pinhole placed in front of each correlation beam only allows its central, high intensity peak to pass. The peaks, which approximate optical delta functions, are Fourier transformed by M1 into plane waves. They arrive at L2 with unique spatial frequencies determined by the location of each pinhole in the mid (or correlation) plane of the resonator.

Each reference beam reads out its corresponding object pattern from L2. One of the wavefronts exiting L2 travels in the object beam direction and is comprised of a superposition of the Fourier transform of each object pattern stored in L2. The magnitude of each pattern is determined by the strength of the reference beam used to read it out, or, equivalently, by the degree of correlation between the input and the same pattern stored in L1. The other wavefronts exiting L2 (as described by Equation 43) are blocked. A portion of the output wavefront exits the resonator at M2 and is Fourier transformed onto a CCD camera. The remaining portion is Fourier transformed by M2 and directed onto B2. B2 passes the strongest images contained in

the wavefront and inhibits the weaker ones. M1 Fourier transforms the images exiting B2 and directs them back onto the distorted input where the strongest Fourier transform in the feedback wavefront adds to, or "fills in", the missing portions of the distorted wavefront. The reference beam exiting L1 whose corresponding object pattern most closely matches the input is now enhanced and the system undergoes another iteration. After many iterations, the strongest object eventually dominates the competition for gain in B2, causing the system to converge on the stored object that most closely matches the distorted input.

3.5.2 Fourier Optics Mathematical Model. The modeling process begins by assuming M, phase encoded, Fourier space holograms have been recorded in L1 and L2 using plane wave reference beams in an angle multiplexing scheme. The crystals are oriented so that their c+ axes both point in the positive z direction. Thus, from section 3.4, the complex transmittances of the $LiNbO_3$ crystals, T1 and T2, are given by

$$\begin{aligned} T_1 &= 1 + j\sum_{k=1}^{M} \gamma^k \left\{ \left|R^k\right|^2 + \left|\bar{V}^k(f_y, f_z)\right|^2 \right. \\ &+ \left. AV^k(f_y, f_z)e^{-j2\pi(\beta^k+\alpha)f_z} + AV^{k^*}(f_y, f_z)e^{+j2\pi(\beta^k+\alpha)f_z} \right\} \end{aligned} \tag{50}$$

$$\begin{aligned} T_2 &= 1 + j\sum k = 1^M \gamma^k \left\{ \left|R^k\right|^2 + \left|\bar{V}^k(-f_y, -f_z)\right|^2 \right. \\ &+ \left. AV^k(-f_y, -f_z)e^{+j2\pi(\beta^k+\alpha)f_z} + AV^{k^*}(-f_y, -f_z)e^{-j2\pi(\beta^k+\alpha)f_z} \right\} \end{aligned} \tag{51}$$

where the reference beams used to record the objects in L2 are the conjugate of the beams used for L1, and the Fourier transforms stored in L2 are inverted relative to those stored in L1. The phase encoded, Fourier space object beams are obtained by placing a phase diffuser directly behing the input object transparency and Fourier transforming the resulting wavefront with a lens located outside the resonator and positioned a focal length from L1. As before, the input enters the resonator at an angle θ in order to separate the image and Fourier domains in the midplane of the resonator.

Now assume a distorted version of the koth stored object is presented to the associative memory. If the distorted input object is described by

$$\hat{\tilde{V}}^{ko} = \hat{V}^{ko} e^{-j2\pi\alpha f_z} \tag{52}$$

then the field just past L1 is

$$\begin{aligned} E_{L1} &= \hat{\tilde{V}}^{ko} \cdot T1 \\ &= \hat{V}^{ko} e^{-j2\pi\alpha f_z} + j\sum_k \gamma^k \left|R^k\right|^2 \hat{V}^{ko} e^{-j2\pi\alpha f_z} \\ &+ j\sum_k \gamma^k \left|\bar{V}^k\right|^2 \hat{V}^{ko} e^{-j2\pi\alpha f_z} \\ &+ j\sum_k \gamma^k A V^k \hat{V}^{ko} e^{-j2\pi(\beta^k+2\alpha)f_z} \\ &+ j\sum_k \gamma^k A V^{k^*} \hat{V}^{ko} e^{+j2\pi\beta^k f_z} \end{aligned} \tag{53}$$

where the fourth term does not propogate because of phase mismatch and the first, second and third terms are blocked as they exit the crystal. The field represented by the fifth term then reflects off the Fourier transforming mirror, M2, and travels to the midplane of the resonator where the field just before the spatial filters (pinholes) is given by

$$\begin{aligned} E_p^- &= \mathcal{F}\{FifthTerm\} \\ &= \mathcal{F}\left\{j\sum_k \gamma^k A V^{k^*} \hat{V}^{ko} e^{+j2\pi\beta^k f_z}\right\} \\ &= j\sum_k \gamma^k A \cdot v^{k^*}(y,z) * \hat{v}^{ko}(-y,-z) * \delta\left(z - \frac{R\zeta^k}{2}\right) \end{aligned} \tag{54}$$

where $*$ denotes convolution, R is the radius of curvature of M2 and ζ^k is the bias angle of each of the M unique reference beams. Following Gaskill, the Fourier transform of the exponential term in Equation 54 was obtained in the following manner

$$\begin{aligned} \mathcal{F}\left\{e^{+j2\pi\beta^k f_z}\right\} &= \delta(z+\beta^k \lambda f) \\ &= \delta\left(z - \frac{\sin\zeta^k}{\lambda}\lambda\frac{R}{2}\right) \end{aligned}$$

$$= \delta\left(z - \frac{R\zeta^k}{2}\right) \tag{55}$$

where $f = \frac{R}{2}$, and, using the small angle approximation, $\sin\zeta \approx \zeta$ (14).

In order to more clearly see the effect of the pinholes on the field in the resonator's midplane, Equation 55 can be expanded into its integral form to yield

$$\begin{aligned} E_p^- &= j\sum_k \gamma^k A \int\int_{-\infty}^{+\infty} v^{k*}(\xi, eta)\hat{v}^{ko}(\xi - y, \eta - z)d\xi d\eta * \delta\left(z - \frac{R\zeta^k}{2}\right) \\ &= j\sum_k \gamma^k A \int\int_{-\infty}^{+\infty} v^{k*}(\xi, eta)\hat{v}^{ko}(\xi - y, \eta - z - \frac{R\zeta^k}{2})d\xi d\eta \end{aligned} \tag{56}$$

where use was made of the relationship $f(x) * \delta(x + x_o) = f(x + x_o)$. Assuming the pinholes are sufficiently small, they may be approximated as optical delta functions located at $\frac{R\zeta^k}{2}$. This approximation then yields the following expression for the combined field just past the pinhole array

$$\begin{aligned} E_p &= j\sum_k \gamma^k A \int\int_{-\infty}^{+\infty} v^{k*}(\xi, \eta)\hat{v}^{ko}(\xi - y, \eta - z - \frac{R\zeta^k}{2})d\xi d\eta \cdot \delta\left(z - \frac{R\zeta^k}{2}\right) \\ &= j\sum_k \gamma^k A \int\int_{-\infty}^{+\infty} v^{k*}(\xi, \eta)\hat{v}^{ko}(\xi, \eta)d\xi d\eta \cdot \delta\left(z - \frac{R\zeta^k}{2}\right) \end{aligned} \tag{57}$$

Note that the double integral in Equation 57 is a constant, and equal to the zero-shift correlation between the distorted input and each of the stored objects. Thus, if we let

$$\int\int_{-\infty}^{+\infty} v^{k*}(\xi, \eta)\hat{v}^{ko}(\xi, \eta)d\xi d\eta = c^k(0, 0) \tag{58}$$

then Equation 57 can be written as

$$E_p = j\sum_k \gamma^k A c^k(0, 0)\delta\left(z - \frac{R\zeta^k}{2}\right) \tag{59}$$

Equation 59 shows the combined wavefront just past the pinholes is a collection of optical delta functions, each weighted by the zero-shift correlation between the distorted input and its respective stored object. This equation assumes the delta functions are separated by a distance greater than

the sum of the widths of the stored and distorted object beam. If the distance were less than the width of the auto-correlation noise, the intensity of a correlation peak corresponding to the wrong object pattern would be artificially increased and the associative memory might converge to the wrong solution.

The optical delta functions in the midplane are equally amplified by B1 and then transformed by M1 into plane waves. The spatial frequency of each plane wave is uniquely determined by the location of its corresponding optical delta function in the resonator's midplane. The planes intersect at L2, yielding the following expression for the combined field just before L2

$$E_{L2}^{-} = j \sum_{k} \gamma^{k} A c^{k}(0,0) e^{-j2\pi\beta^{k} f_{z}} \tag{60}$$

Because the gain introduced by B1 is linear, it has no affect on the mathematics of the Fourier optics model and is not included in the field expression given by Equation 60.

The wavefront exiting L2 can be modeled as the product of the crystal's complex transmittance, T2, with the combined field illuminating L2. Assuming Equation 60 represents the input, the field just past the crystal is then

$$\begin{aligned}
E_{L2} &= E_{L2}^{-} \cdot T_2 \\
&= j \sum_{k} \gamma^{k} A c^{k}(0,0) e^{-j2\pi\beta^{k} f_{z}} \\
&+ j \sum_{k} \gamma^{k} A c^{k}(0,0) e^{-j2\pi\beta^{k} f_{z}} j \sum_{k'} \gamma^{k'} \left| R^{k'} \right|^{2} \\
&+ j \sum_{k} \gamma^{k} A c^{k}(0,0) e^{-j2\pi\beta^{k} f_{z}} j \sum_{k'} \gamma^{k'} \left| \bar{V}^{k'} \right|^{2} \\
&+ j \sum_{k} \gamma^{k} A c^{k}(0,0) e^{-j2\pi\beta^{k} f_{z}} j \sum_{k'} \gamma^{k'} A V^{k} e^{+j2\pi(\beta^{k}+\alpha) f_{z}} \\
&+ j \sum_{k} \gamma^{k} A c^{k}(0,0) e^{-j2\pi\beta^{k} f_{z}} j \sum_{k'} \gamma^{k'} A V^{k'^{*}} e^{-j2\pi(\beta^{k}+\alpha) f_{z}}
\end{aligned} \tag{61}$$

where, this time, the fifth term does not propogate due to phase mismatch and the first, second and third terms are blocked as they exit the crystal.

If we now assume the coupling strength between the kth reference beam and the k'th object stored in L2 is minimal for $k \neq k'$, then for $k = k'$, the field just past L2 can be expressed as

$$E_{L2} = \sum_k \gamma^k A^2 c^k(0,0) V^k e^{+j2\pi\alpha f_x} \tag{62}$$

Equation 62 implies the field just past L2 is a superposition of all Fourier transformed, phase encoded object patterns stored in L2 where the magnitude of each pattern is proportional to the correlation between the distorted input and the stored object.

The field described by Equation 62 travels to M2 where a portion exits as output. The remaining portion reflects off M2 and arrives, Fourier transformed, at B2. B2 passes the high intensity object patterns and attenuates the low intensity patterns. Assuming the attenuation characteristics of B2 can be described by a single function $f(\cdot)$, the field just past B2 is

$$E_{B2} = f\left(\sum_k \left[\gamma^k A^2 c^k(0,0) v^k\right] * \delta(z - \frac{R\theta}{2})\right) \tag{63}$$

Crystal M1 Fourier transforms the combined field described by Equation 63 and directs it back onto the input wavefront. After many iterations in the FPCR, the nonlinearity introduced by B2 will eventually attenuate all object patterns in Equation 62, except the object displaying the highest correlation with the distorted input. In this sense, the behavior of the F- OAM is very similar to that of Hopfield's neural network associative memory. In fact, the following section describes how the F-OAM implements an inner-product version of the Hopfield algorithm.

3.5.3 Inner-Product Implementation of the Hopfield Neural Network Associative Memory Algorithm. Recall from Chapter 2, that the inner product implementation of the Hopfield algorithm resulted in the following expression for the steady state output of each node in the Hopfield architecture

$$V_i = f\left(V_i^{ko}(V^{ko}, \hat{V}^{ko}) + \sum_{k \neq ko} V_i^k(V^k, \hat{V}^{ko})\right) \tag{64}$$

where $\hat{V}^{ko}$ is a distorted version of V^{ko}, $(\cdot,\cdot)$ denotes the inner product operation, and f is a nonlinear function that passes strong signals and attenuates weak ones. In order to show the

operation of the F-OAM can be described by a similar equation, we begin by examining the integral form of the combined field just after it exits B2. Expanding equation 63 gives

$$\begin{aligned} E_{B2} &= f\left(\sum_k \left[\gamma^k A^2 c^k(0,0) v^k\right] * \delta(z - \frac{R\theta}{2})\right) \\ &= f\left(\sum_k \left[\gamma^k A^2 v^k \int\int_{-\infty}^{+\infty} v^{k^*}(\xi,\eta)\hat{v}^{ko}(\xi,\eta)d\xi d\eta\right] * \delta(z - \frac{R\theta}{2})\right) \end{aligned} \tag{65}$$

Note that the zero-shift correlation between the stored object pattern, v^{k^*}, and the distorted version of the input object, $\hat{v}^{ko}$, is simply the vector dot product of the two functions. Thus, Equation 65 can be rewritten as

$$E_{B2} = f\left(\sum_k \left[\gamma^k A^2 v^k (v^{k^*}, \hat{v}^{ko})\right] * \delta(z - \frac{R\theta}{2})\right) \tag{66}$$

where, again, $(\cdot,\cdot)$ implies dot product. Dropping the delta function since it only imposes an arbitrary location on the wavefront, and assuming: 1) the reference beams are of unit amplitude ($i.e., A = 1$), 2) the diffraction efficiencies of all stored gratings are equal ($\gamma^k = constant = \gamma$), and 3) the combined object field located before the pinholes is real so that $v^{k^*} = v^k$, the above expression reduces to

$$\begin{aligned} E_{B2} &= f\left(\gamma \sum_k v^k (v^k, \hat{v}^{ko})\right) \\ &= f\left(\gamma v^{ko}(v^{ko}, \hat{v}^{ko}) + \gamma \sum_{k \neq ko} v^k (v^k, \hat{v}^{ko})\right) \end{aligned} \tag{67}$$

Equation 67 shows that the field exiting B2 is the weighted sum of all stored objects where the weights equal the inner product of each object with the distorted input. Additionally, B2 acts as a nonlinear attenuator that passes high signals and attenuates low signals. Therefore, with the exception of the diffraction efficiency constant, γ, a comparison of Equations 64 and 67 indicates the F- OAM implements a spatially continuous, inner product version of the discrete, Hopfield neural network associative memory algorithm.

3.6 Conclusion

This chapter begar by examining the behavior of the three major components in the F-OAM. The optical feedback properties of the FPCR were discussed which included an analysis of its feedback phase characteristics. The two-wave coupling behavior of $BaTiO_3$ was examined and it was shown how one can control its gain and attenuation behavior by adjusting the crystal and beam geometry. $Fe : LiNbO_3$'s holographic storage and recall properties were also discussed and equations were provided which model the complex transmittance that results when an angle multiplexing scheme is used to record M objects in a $LiNbO_3$ crystal placed inside the FPCR. A Fourier optics mathematical model was then developed that described the behavior of the F-OAM at various points in its operation. Finally, the F-OAM was shown to implement an inner product version of the Hopfield neural network associative memory algorithm. The next chapter presents experimental results obtained from the construction and operation of an optical associative memory built from discrete optical components that models the behavior of the F-OAM.

IV. A Discrete Model of the Fabry-Perot Confocal Resonator Optical Associative Memory.

4.1 Introduction

The original plan for the experimental portion of this thesis called for a separate investigation into the operational characteristics of the F-OAM's three major components: the $BaTiO_3$ gain and attenuation elements, the $LiNbO_3$ memory storage and recall elements, and the Fabry-Perot confocal resonator (FPCR). The results of these investigations were to then be used to guide the construction and operation of the F-OAM system. However, after observing the behavior of a single $BaTiO_3$ crystal placed in the Fourier plane of the resonator, it was evident the FPCR's limited processing environment would make it difficult to observe and control the ensemble operation of the holographic storage and recall process. Therefore, a large scale model of the F-OAM was constructed from discrete optical components (i.e., lenses, mirrors and beamsplitters) that provided the space and flexibility required to adequately investigate the operation of the F-OAM's internal components.

The second section of this chapter presents the results obtained from preliminary investigations into the two-wave coupling gain and attenuation process. It also examines the phase encoded Fourier transform holographic storage and recall process and discusses a phase encoding technique used to improve the process. The results of these experiments are then used to develop and implement a system design.

The chapter's third section describes in detail the development and construction of the discrete system design. It focuses first on the construction and alignment of the discrete optical feedback loop and the manner in which the internal components were arranged in the loop to model Wilson's original design. The results of initial system tests are then described which led to modifications in Wilson's original design. The final system design, incorporating these modifications, is discussed last.

Section four focuses on the methodology and procedures used to train the system. The angle multiplex storage scheme used to store objects in the system is presented, followed by a detailed explanation of the procedures used to train the system to recognize a single object.

The last section examines the operation of each phase of the associative memory by following the distorted input as it passes through each component in the system. The section then provides an analysis of overall system results and concludes with recommendations for improving the complete system design.

4.2 Preliminary Experiments

All four $BaTiO_3$ and $LiNbO_3$ crystals play a key role in determining how well the associative memory is able to recall a complete object when presented with a partial version of the object. Among other things, their performance characteristics determine how much pump beam bias must be applied to achieve maximum gain and attenuation, and what object and reference beam parameters are required to accurately store and recall information. Since every photorefractive crystal is unique, these performance characteristics, or profiles, must be obtained empirically. Unfortunately, empirical data was not available for either $BaTiO_3$ crystal and one of the $LiNbO_3$ crystals. Therefore, the preliminary experiments presented in this section had to be performed before finalizing a system design.

4.2.1 Experimental Measurements of $BaTiO_3$ Gain and Attenuation Elements. Keppler and Wilson both experimentally investigated the gain and attenuation characteristics of several z-cut and 45°-cut crystals. It was assumed one or more of these crystals would eventually be used in the F-OAM. However, preliminary gain measurements conducted here showed neither type of previously investigated crystal was able to provide the steady state gain characteristics required for system operation. The z-cut crystals investigated by Wilson did not provide the gain required to overcome cavity losses. The 45° cut crystals investigated by both Wilson and Keppler were unacceptable due to the unstable nature of their gain profile. System tests conducted with the 45° crystals showed the gain profile and the quality of the signal beam were adversely affected by high beam fanning losses. These results agreed with those reported by Wilson and Keppler (35) (22).

It was clear from the above experimental results that the crystals investigated by Wilson and Keppler would not provide the stable gain profile needed to successfully operate the associative memory. Therefore, a pair of z-cut $BaTiO_3$ crystals, larger than those used by Wilson, were obtained from the AFIT Physics Dept. Preliminary gain measurements obtained from the larger of

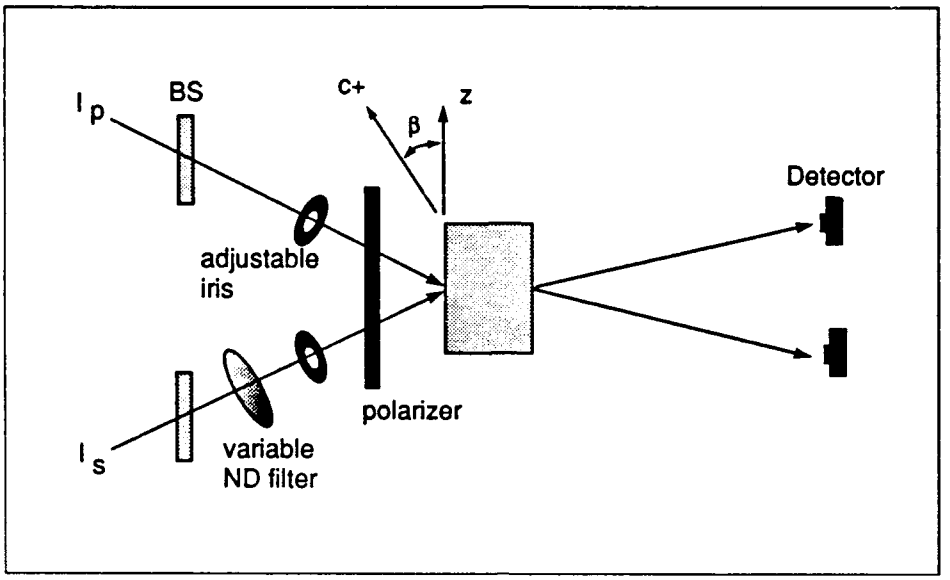

Figure 34. Experimental setup used to measure $BaTiO_3$ gain and attenuation characteristics. I_p and I_s are the input pump and signal beams respectively.

the two crystals demonstrated it was potentially capable of providing steady state gain values large enough to overcome losses in the associative memory feedback loop. The gain characteristics of the second, smaller, crystal were not as large as the first crystal; however, they were still larger than the crystals investigated by Wilson. Therefore, the second crystal was chosen as a candidate for the associative memory attenuation element.

4.2.1.1 Gain Measurements - $BaTiO_3$ Crystal # 164- E. The experimental setup used to characterize the behavior of the $BaTiO_3$ gain element is shown in Figure 34. Beamsplitters are placed in the signal and pump beam paths to check for phase conjugate returns, while a polarizer ensures both beams are polarized in the crystal's extraordinary direction. Two variable neutral density filters are placed in the path of the signal beam to control its intensity over a wide range of values, and adjustable circular irises control the size of the input signal and pump beams. Detectors are used to record the output signal and pump beams before, during and after each two-wave coupling measurement. The Argon-Ion laser used in the experiment is a Coherent Innova 100 with an internal etalon and prism that restrict its operation to a single longitudinal mode at 514.5 nm.

The first step in the gain experiment was to locate the c^+ axis of the crystal. Recall from

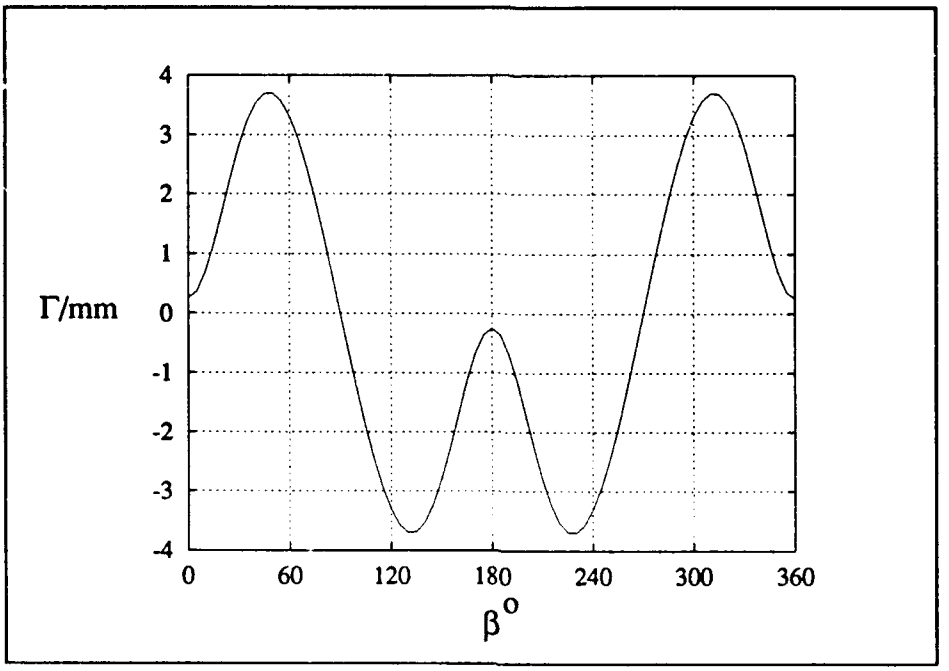

Figure 35. Variations in two wave coupling gain coefficient as β is varied between 0 and 360°.

Chapter 3 that output energy in a two wave coupling process is transferred in the direction of the c^+ axis. Also recall that the magnitude of the gain coefficient is a function of the grating vector angle β, where β is varied by rotating the crystal. The theoretical behavior of the gain coefficient for $\beta = 0$ to 360° (i.e., one full rotation of the crystal) is shown in Figure 35. This curve shows that when the crystal shown in Figure 34 is rotated in a counter-clockwise direction, the two wave coupling process should yield a) a positive signal gain for $\beta = 0$ to 90°, b) a negative signal gain for $\beta = 90$ to 270°, and a positive signal gain for $\beta = 270$ to 360°. Measuring the output signal gain for different crystal orientations between $\beta = 0$ and 360°, then provides a gain pattern from which the direction of the positive c axis can be deduced.

Ideally, one would conduct this experiment by measuring the output signal gain at regular intervals, say every 45°, as the crystal is rotated one full turn. However, the crystal can only be rotated approximately 20° on either side of $\beta = 0, 90, 180$ and 270° because its large index of refraction (≈ 2.5) causes the signal beam to "bend" out the side of the crystal. Thus, signal gain measurements were made at crystal orientations of $0 \pm 20°, 90 \pm 20°, 180 \pm 20°$ and $270 \pm 20°$.

The input pump to signal beam intensity ratio was set at approximately 10,000 to 1 and the pump beam spot size was large enough to ensure both beams interacted throughout the length of the crystal.

The signal gain generally behaved in the manner predicted by the theoretical curve shown in Figure 35, and the results were used to deduce the positive c axis of the crystal. However, the signal gain behaved anomalously between what was eventually determined to be $\beta = 0$ and 20^o. For these orientations, the gain would quickly grow to a peak value and then slowly decay to a steady state intensity less than the input signal intensity. Repeated observations of the crystal's gain behavior at $\beta = 20^o$ revealed the decay in output signal intensity was caused by the gradual creation of a pump beam phase conjugate return inside the crystal. The phase conjugate beam removes pump beam energy available for two wave coupling and, therefore, makes this orientation undesirable for achieving the high gain values required in the associative memory.

In order to avoid the problem described above, yet still achieve two wave coupling gain, the crystal was rotated to $\beta = 270^o$ as shown in Figure 36. Rotating the crystal counter clockwise from this location points the c + axis in the direction of the output signal beam, causing energy to transfer from the pump to the signal beam.

Because it was initially assumed the crystal orientation used to achieve gain in the associative memory would require β to vary between 0 and 90^o, the theoretical gain curves provided in Chapter 3 were developed for these values of β. The new crystal orientation, however, varies β between 270 and 360^o. In order to verify and predict the gain for these values of β, new theoretical gain curves were developed. The new gain curve obtained by varying β between 270 and 360^o, for fixed values of θ, is shown in Figure 37. This curve shows the gain behavior for the range of new β values is almost identical to the behavior predicted for $\beta = 0$ to 90^o. These results theoretically verify the gain potential of the new crystal orientation.

Gain values for the above crystal orientation were empirically verified in two different experiments. In the first experiment, signal gain was measured as a function of the input signal to pump beam ratio, r. The beam diameters of the plane wave signal and pump beams were $2mm$ and $1mm$ respectively, corresponding approximately to the beam diameters predicted in the associative memory. The power in the pump beam was held constant at 5 mW. Signal to pump

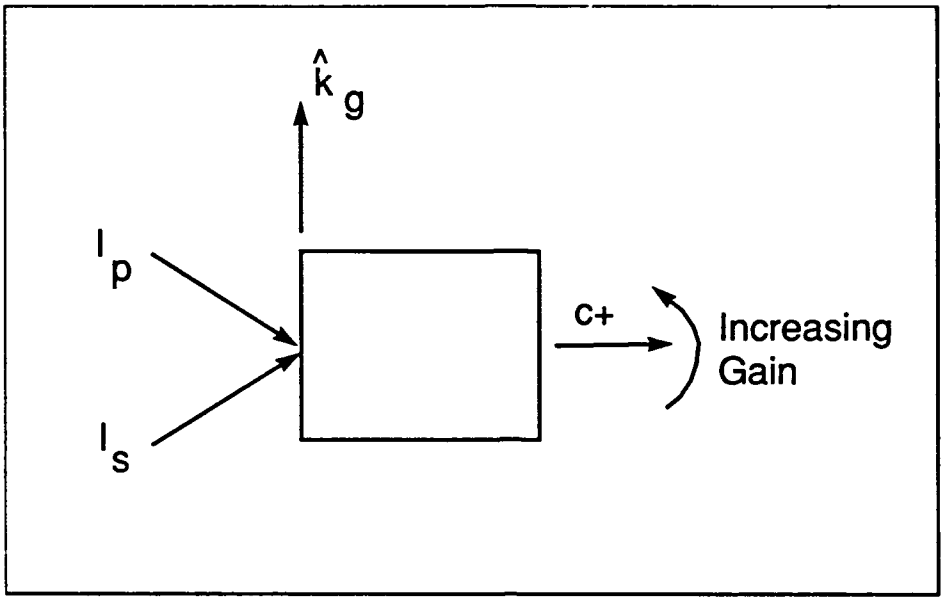

Figure 36. Crystal orientation used to provide gain in the associative memory. Gain is increased by rotating the crystal counter clockwise as shown.

beam intensity ratios between approximately 10^{-5} and 1 were obtained by varying the neutral density filters placed in the path of the input signal beam. The internal separation angle, θ, and the grating vector angle, β, were fixed at 3^o and 10^o respectively. For each value of r, the following parameters were measured: the power in the output signal beam without the pump beam (I_s^-), , the power in the output signal with the pump beam (I_s^+), the beam fanning noise deflected in the direction of the signal beam (N_{bf}), and the power in the output pump beam without the signal beam (I_p).

The input pump beam to signal beam ratio, r, was calculated from the ratio

$$r = \frac{I_s^-}{I_p} \tag{68}$$

where it's assumed the absorption and scattering losses through the crystal are small enough that the output powers provide an accurate estimation of the input beam powers after reflection losses at the crystal face. Beam fanning noise in the output signal direction was measured by removing the signal beam after the internal grating had formed, allowing the pump beam to erase the grating,

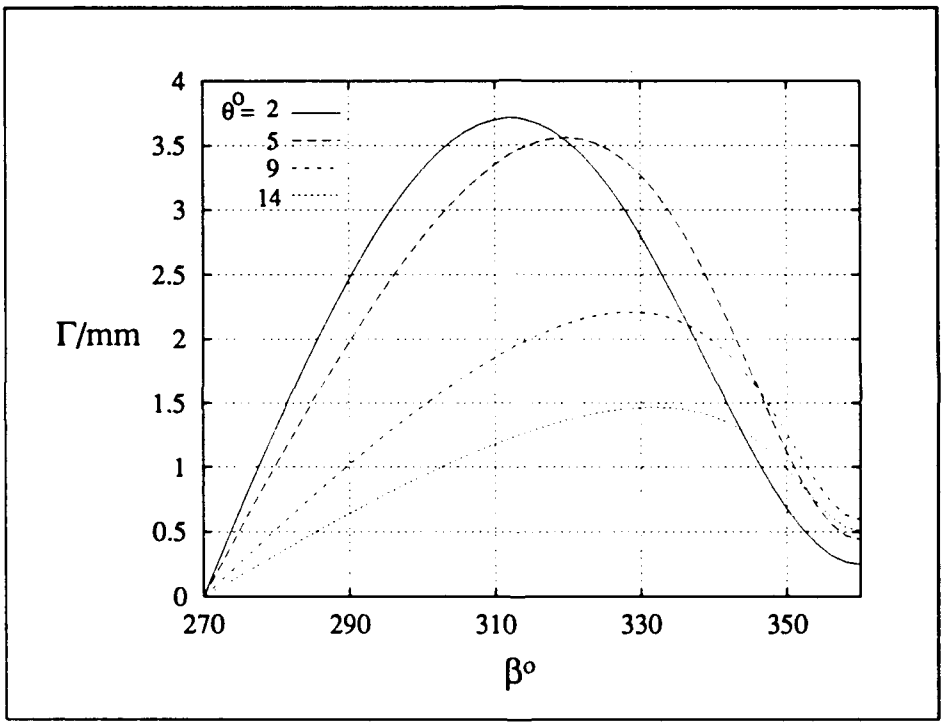

Figure 37. Plot of ideal $BaTiO_3$ crystal gain coefficient, Γ, vs grating vector angle, β, for various values of internal beam separation angle, θ.

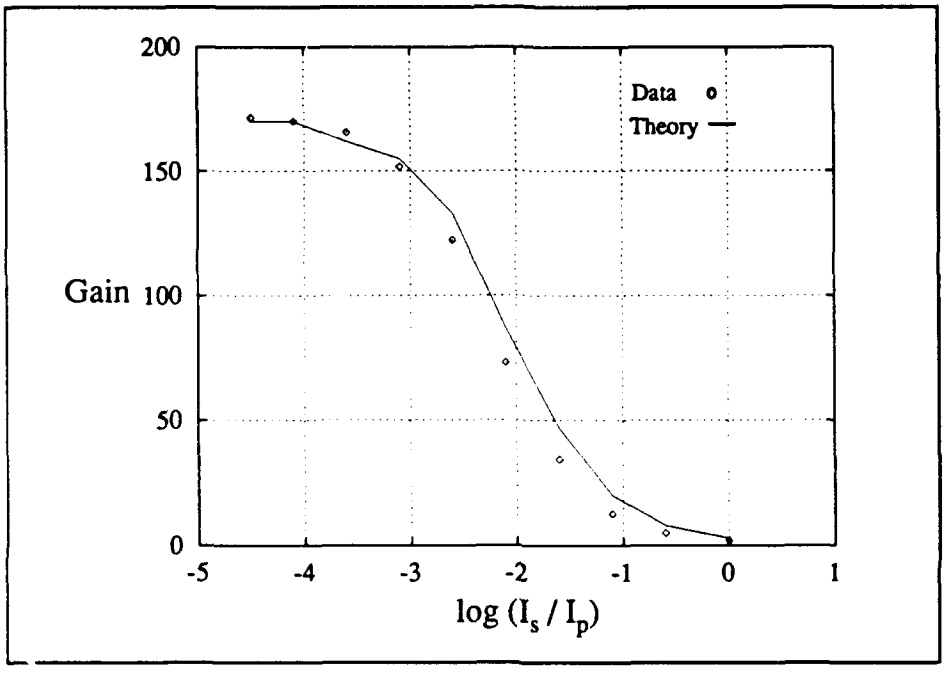

Figure 38. Experimental and theoretical output signal gain vs input signal beam, I_s, to input pump beam, I_p ratio. Internal beam separation angle, θ, was 3° and grating vector angle, β, was 10°. Measurements account for Fresnel reflection losses at the crystal face and beam fanning noise in the direction of the output signal.

and measuring the fanned energy over an area equal to the size of the output signal beam. The crystal gain, G, was then calculated using the following equation:

$$G = \frac{I_s^+ - N_{bf}}{I_s^-} \tag{69}$$

The experimental gain data shown in Figure 38 matches the predicted behavior presented in Chapter 3. The saturated gain region is flat up to an input signal to pump beam ratio of approximately 10^{-4}. The gain then decreases rapidly until flattening out again at a ratio of approximately one. The theoretical curve from Chapter 3 is plotted over the experimental data

to demonstrate how closely the experimental and theoretical gain trends match. The theoretical curve was obtained using the same constants specified in Section 3.3.2.3., with the exception of N, the number of available charge carriers. Here, N was chosen to be one half the value used in Chapter 3, or $1x10^{22}\,m^{-3}$ in order to approximately match the theoretical curve to the experimental results. It should be noted here, that the purpose of the experiment was not to verify that the experimental data matched a particular theoretical gain profile, only that it followed the theoretical gain trend. Thus, the theoretical curve shown here is meant only to demonstrate the agreement between experimental and theoretical gain trends.

Besides verifying theoretical predictions about the crystal's gain behavior, these experimental results also yield the pump beam intensity required to "bias" the two wave coupling process for operation in the saturated gain regime of the crystal. The experimental data in Figure 38 shows that in order to bias the crystal to operate in the flat region of the gain curve, the pump beam should be set so that the ratio between the strongest reconstructed reference beam exiting C1 and the pump beam is approximately 10^{-4}.

The second $BaTiO_3$ experiment was conducted to verify that the crystal gain followed the theoretical trend predicted for variations in grating vector angle, β. The input signal to pump beam ratio was set at 10^{-5} to ensure the crystal was biased to operate in its saturated gain regime. The internal separation angle between the signal and pump beams was again approximately 3^o. The crystal was placed on a rotating turntable accurate to within 0.5^o, and the pump and signal beam spot sizes were adjusted to ensure the beams interacted throughout the length of the crystal. As β was varied by two degree increments between 269 and 285^o, the following parameters were measured: the power in the output signal beam without the pump beam, the power in the output signal with the pump beam, and the beam fanning noise deflected in the direction of the signal beam.

Figure 39 plots the experimentally determined gain coefficient, Γ, as a function of the grating vector angle β. The expression for saturated gain introduced in Chapter 3 was used to compute the gain coefficient values. The theoretical curve provides a comparison between the predicted and measured gain trends. As before, the theoretical curve was obtained using the constants provided in Chapter 3 with N set at $1x10^{22}\,m^{-3}$. For β slightly less than 270^o, the c+ axis point in the direction of the output pump beam, causing energy to transfer from the signal to

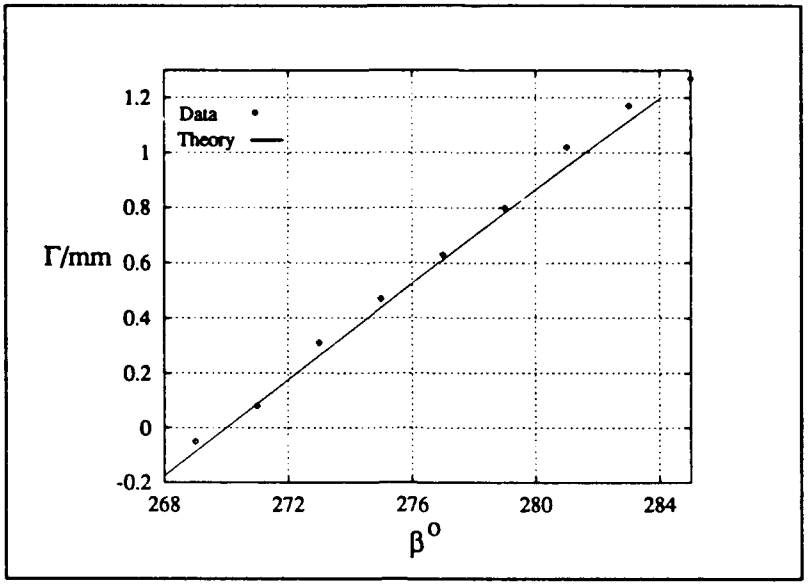

Figure 39. Theoretical and experimental curves for gain coefficient, Γ, as a function of grating vector angle, β. Experimental values obtained using $\theta = 3^o$ and an input signal to pump beam ratio of 10^{-5}.

the pump beam. Thus, as the theoretical and experimental curves both show, the gain coefficient is negative. For β between 270^o and 286^o, the c+ axis points in the direction of the signal beam, and the theoretical and experimental behavior of the gain coefficient is positive and nearly linear.

4.2.1.2 Attenuation Measurements - $BaTiO_3$ Crystal # 119-D. The attenuation theory in Chapter 3 predicts that when the c+ axis of a $BaTiO_3$ crystal points in the direction of the output pump beam, high intensity signals are passed and low intensity signals are attenuated. Although Wilson previously characterized the attenuation profile of a thin, z-cut $BaTiO_3$ crystal, it was believed a larger crystal might provide improved attenuation performance for the same reasons it provides higher gain. Therefore, a larger z-cut crystal (by approximately 1 mm in each dimension) was tested to determine if its attenuation characteristics exceeded those measured by Wilson. The experimental setup used to measure crystal gain was also used to measure the crystal's attenuation characteristics. However, the continuously variable neutral density filters were placed in the path of the pump, rather than the signal beam, in order to control pump beam intensity. The internal beam separation angle and the external grating vector angle were set at 3^o

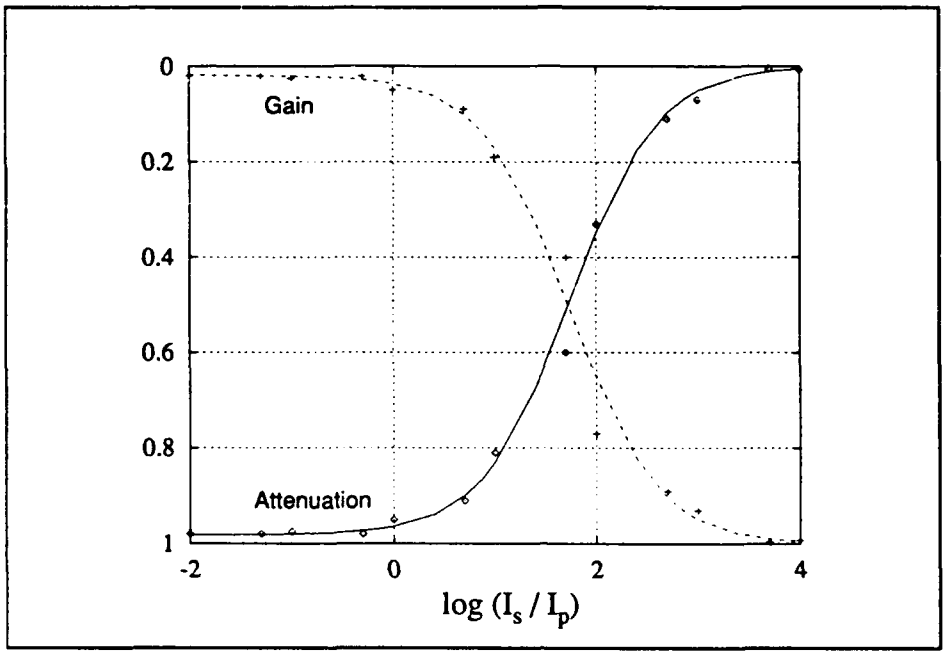

Figure 40. Theoretical and experimental gain, G, and attenuation, A = 1 - G, as a function of input signal to pump beam intensity ratio for $\beta_{ext} = 190^o$ and $\theta_{int} = 3^o$.

and 190° respectively. The input beam intensities were adjusted to yield a range of signal to pump beam intensity ratios of 10^{-3} to 10^3. The ratio was then varied in increments of 10 and, as before, the following parameters were measured at each increment: the power in the output signal beam without the pump beam, the power in the output signal with the pump beam, the beam fanning noise deflected in the direction of the signal beam, and the power in the output pump beam without the signal beam. The signal to pump beam ratios and the signal gain were then calculated using Equations 68 and 69. The signal attenuation, A(r), was obtained by subtracting each gain value from unity (i.e., A(r) = 1 - G(r)). The results are shown in Figure 40.

The theoretical curve and experimental data points for signal gain are plotted as a function of r on the plot's left axis. The attenuation is plotted on the right axis. The theoretical curves were obtained using the attenuation equation developed in Chapter 3.3.3. with $\Gamma L_{eff} = 3$. Again, the theoretical curves were not used to predict the experimental data, only to demonstrate that the data follows the theoretical attenuation trend. The experimental data clearly shows the crystal attenuates low intensity input signals and passes high intensity signals. Additionally, a side by

side comparison of this crystal and the crystal Wilson tested for use in the associative memory (see Figure 41 below) shows the larger crystal more closely approximates the theoretical attenuation behavior for large input signal to pump ratios. And, more importantly, the higher gain coefficient achieved with the larger crystal results in a steeper slope in the transition phase of the curve between low and high input signal intensities. A steep slope is particularly important in the associative memory where one attempts to bias the crystal to pass a single high intensity reference beam and attenuate the remaining, lower intensity reference beams. Thus, based on the above experimental results, the larger crystal was chosen as the associative memory attenuation element.

4.2.2 Phase Diffuse Fourier Transform Holograms in $LiNbO_3$. When an object and reference beam interfere in a $LiNbO_3$ crystal to form a volume hologram, each bit of information in the object pattern is stored in the form of a localized diffraction grating in the crystal. If the crystal contains imperfections in the area in which one piece of object information is stored, or if that portion of the object contains noise, the diffraction grating formed in the crystal (if one is formed at all) will not accurately reconstruct that bit of object information. Fourier transforms, rather than objects, are often used to form holograms because information about each piece of the object is spread out over the entire Fourier transform. If localized imperfections in the crystal fail to form a distorted holographic grating for one spatial frequency component, information about a piece of the object will be reconstructed from other frequency components whose holographic gratings are formed elsewhere in the crystal volume (2)

One problem encountered when storing Fourier transforms in a photorefractive crystal is that most of the object intensity is contained in the object's central, or DC, frequency component. Because, the intensities of higher spatial frequency components are small compared to the DC component, the diffraction efficiency of the localized gratings formed from these components is quite small. Thus, when the object is reconstructed from a normal Fourier transform hologram, many of the spatial frequency components are missing and the object resolution can be considerably diminished. Therefore, if one wishes to form a high quality hologram, the light in the Fourier transform must be spread more evenly over the recording plane. One method for doing this is to place a phase mask directly behind the object transparency.

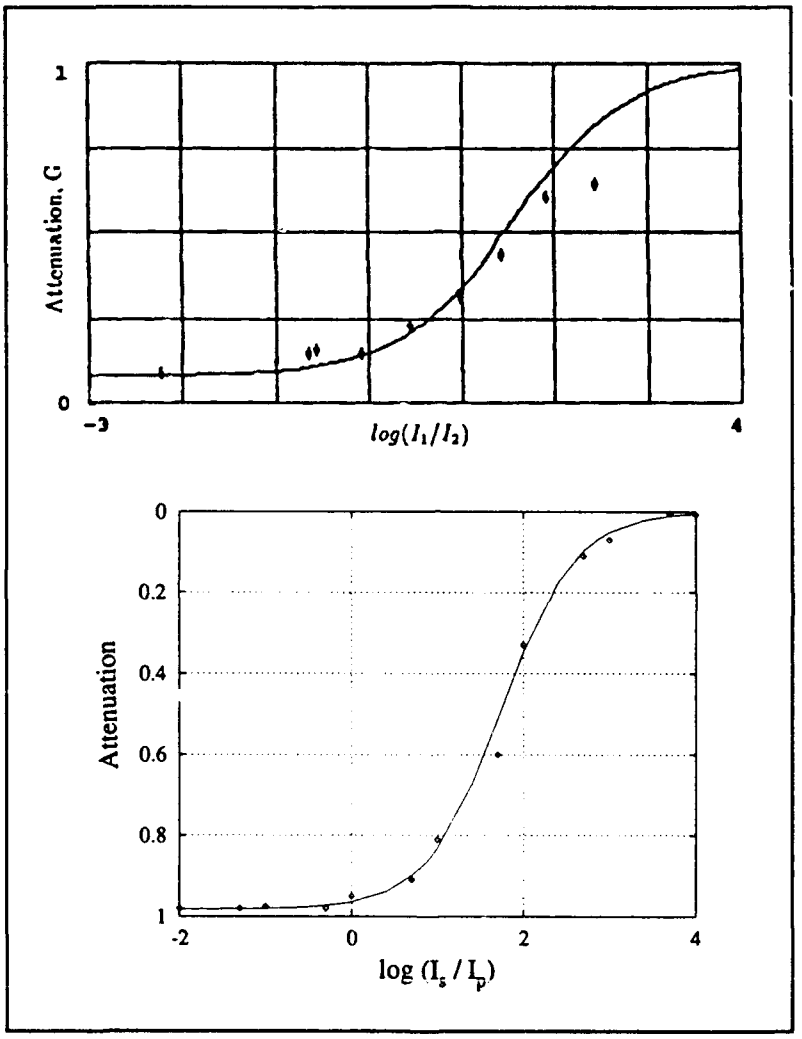

Figure 41. a) Attenuation data collected by Wilson for z-cut crystal # 119-B. b) Attenuation data collected here for z-cut crystal # 119-D. The steep slope in the attenuation curve of crystal # 119-D makes it more suitable than 119-B as an associative memory attenuation element (35:59).

A phase mask, or phase encoder, applies a random phase shift to light incident on it. And, by doing so, spreads the energy out of an object's high intensity DC spatial frequency component into its higher spatial frequency components. Phase encoders are typically constructed from etched glass, where the depth of the etched pattern determines the amount of the phase shift. The etching process is generally well controlled in order to impose a precise phase shift on an incident light beam (2).

An ideal phase diffuser would spread the energy in the DC term in a uniform manner over a desired recording region without spreading wasted energy into spatial frequency components that lie outside the physical dimensions of the recording medium. In a telephone conversation with Dr. H. Stoll from Hughes Research and Technology Center in Palos Verdes Peninsula, CA, it was learned that several thousand dollars were spent to design and fabricate a phase diffuser that approximates ideal behavior for use in their optical associative memory. Because of the limited availability of funds for this thesis project, initial experiments conducted in the discrete F-OAM employed a plastic bag phase diffuser similar to the one used by Frye.

The results of initial system tests using the plastic bag (discussed in detail later in this chapter) were discouraging. When the complete object stored in the associative memory was presented to the system, a dim blur of light was produced at the output that had the same general outline of the stored object, but lacked any edge definition. After repeated system tests continued to produce the same results, the second $LiNbO_3$ crystal was removed from the system and used to conduct separate, "off line" holographic storage and recall experiments designed to pinpoint the cause of the problem.

In these experiments, a phase encoded Fourier transform hologram was recorded in the crystal using the same experimental setup and procedures employed by Frye (13:17). The recording parameters were similar to those measured at the second crystal during system operation and included a total input beam power of $7mW$, input object and reference beam powers of 5 and $2mW$ respectively, and an beam separation angle of 12^{o}. The beam diameter of both beams was $6mm$ and the recording time was approximately 60 seconds. After recording the hologram, the crystal was illuminated with the reference beam used in the recording process and the reconstructed object was observed on a screen.

After several experiments, it was found the blurred system output could be duplicated by varying two reference beam parameters: intensity, and spot size. As expected, reducing the reference beam intensity also reduced the intensity of the reconstructed object; however, even when the input intensity was so low the output was barely discernable (as in the operational experiment), the edges of the reconstructed object were clearly visible. When the spot size of the reference beam was then reduced to approximately the same size as the reference beam reconstructed at the first $LiNbO_3$ crystal, the output lost its edges and clearly resembled the "blob" observed during system operation.

It was evident from these experiments that the beam diameter of the reference beam reconstructed at the first $LiNbO_3$ crystal during system operation was too narrow to illuminate, and therefore reconstruct, the higher spatial frequency components stored in the second $LiNbO_3$ crystal. The beam diameter was narrow because the higher spatial frequency components in the phase encoded Fourier transform did not possess the intensity required to form a diffraction grating in the crystal over the outer regions of the plane wave reference beam. In order to improve the quality of the image reconstructed at the second $LiNbO_3$ crystal, the size of the intense central portion of the phase encoded Fourier transform used in the recording process would have to be enlarged. This was accomplished by increasing the strength of the phase diffuser.

Several types of phase diffusers were tested for their ability to spread the energy in the object DC component more uniformly over a larger area. These included a multi-layered plastic bag, sand blasted glass and an opal coated diffuser purchased from Edmund Scientific Co. Each diffuser spread more energy over a larger area than the single layer of plastic, however, none proved suitable for use in the associative memory. As Frye noted, the plastic bag phase diffuser is anisotropic. Polarization measurements made on the object beam with and without the bag showed the bag's anisotropic material converted linearly polarized light with an extinction ratio of 90 to 1 into elliptically polarized light with an extinction ratio of 40 to 1. As additional layers of plastic bag were added, the extinction ratio dropped even further, causing significant losses in object beam energy when the beam was extraordinarily polarized for holographic recording. The sand blasted glass and opal coated phase diffusers also caused substantial object beam energy losses by spreading an excessive amount of DC energy beyond the dimensions of the $LiNbO_3$ crystal. In both cases, the maximum obtainable power in the useful portion of the object beam

was less than $1mW$.

Some degree of control over the DC energy distribution was finally achieved using phase diffusers formed by swirling glass microscope slides in a 40% percent hydrofluoric acid solution for varying periods of time. Four phase diffusers were created this way using incremental exposure times of 30, 60, 90 and 120 seconds. Polarization measurements performed on each slide showed they had no effect on object beam polarization. Photographs of the phase encoded Fourier transforms produced by the acid etched slides are shown in Figure 42. The photographs were obtained by placing a Calumet camera loaded with 400 ASA film directly behind a large piece of diffuse plastic placed in the phase encoded object's Fourier plane. The camera's f# and exposure time were set at 1.6 and 1/15 seconds respectively.

The photographs do not capture much of the detail in the Fourier transforms (the intensity across the central bright region in each of the photographs is not as uniform as it appears), however they do show how the diffusers spread energy out of the object's intense DC component into its higher spatial frequencies components. And, more importantly, they show how the DC energy distribution can be controlled by varying the etching exposure time. Because the maximum object beam energy obtained using the 120 second phase diffuser was significantly less than the object beam energy recommended by Frye for maximum diffraction efficiency, stronger acid etched phase diffusers were not investigated. However, this area is strongly recommended for future graduate research at AFIT.

4.3 Discrete Optical Associative Memory System Design

The first step in this phase of the thesis was to construct a discrete model of the F-OAM architecture based on Wilson's original design proposal. Initial system tests were then performed which uncovered practical and theoretical deficiencies in the original design. The majority of these deficiencies were corrected through design modifications. The problems that were not corrected are believed to be caused by fundamental design constraints imposed by the FPCR optical processing environment.

4.3.1 Discrete Optical Feedback Loop. The discrete optical feedback system was designed and constructed using optical elements presently available at AFIT. Although the performance

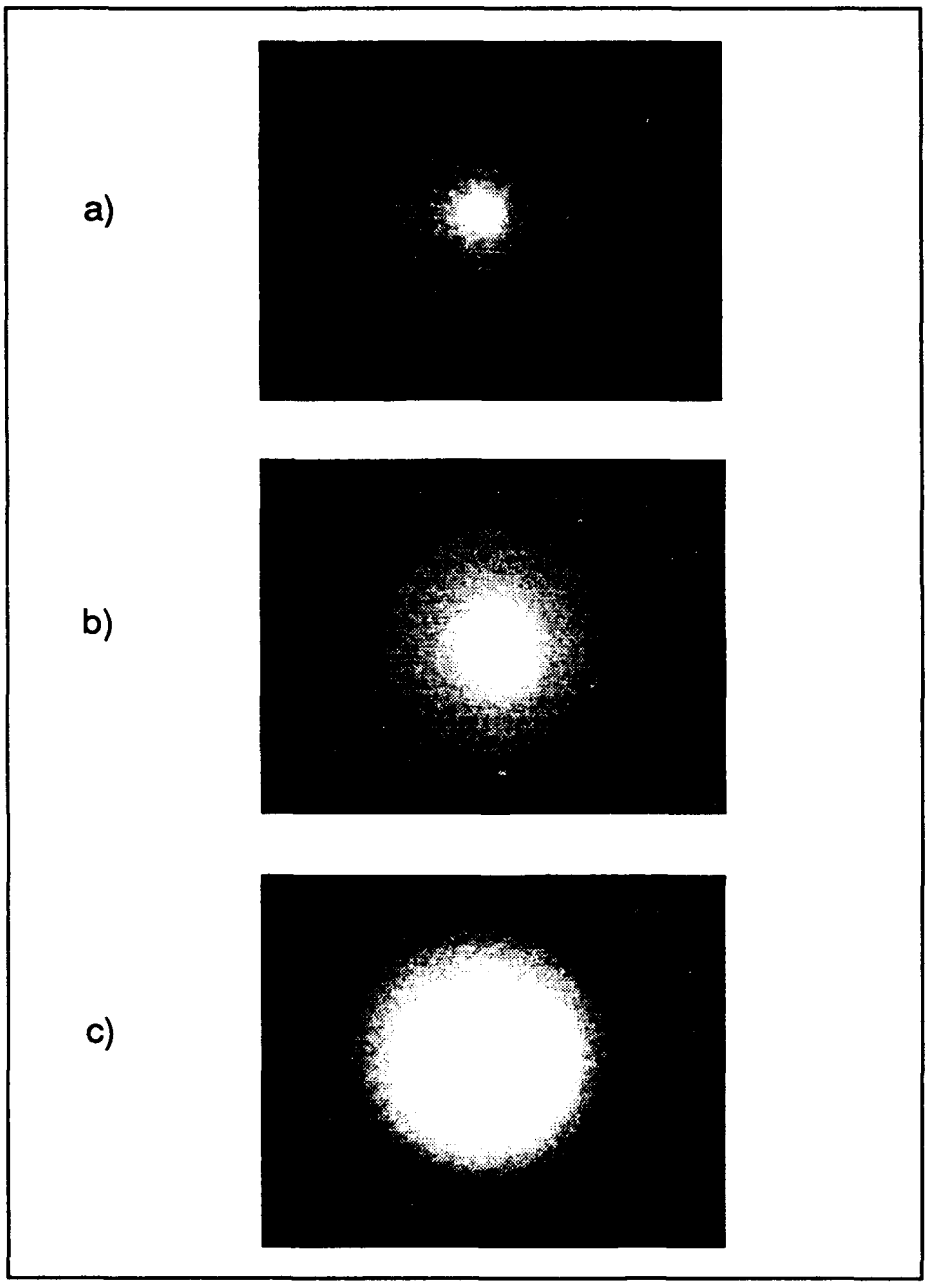

Figure 42. Phase diffuse Fourier transforms of an AF resolution chart using three different acid etched glass phase diffusers. a) A single glass slide etched for 60 seconds, b) 90 seconds, and c) 120 seconds.

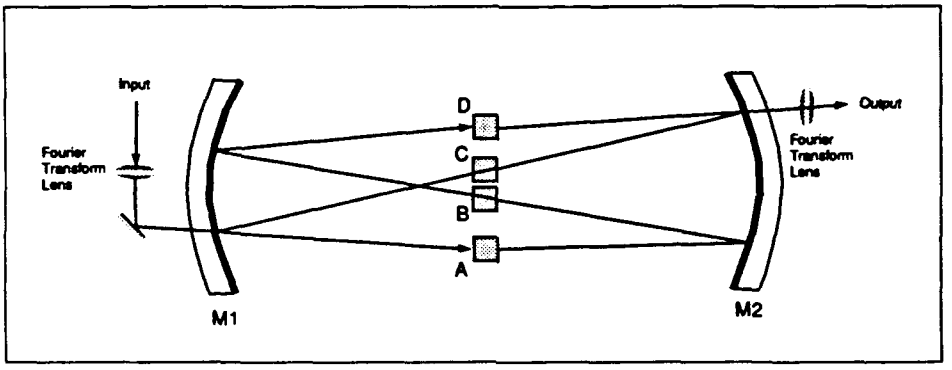

Figure 43. Fabry-Perot Confocal Resonator showing external Fourier transforming lenses.

of the system would undoubtedly improve by using lenses and beamsplitters with $f^{\#}$'s and transmission characteristics custom made for this application, the components used here proved more than adequate as a "test bed" for exploring the feasibility of Wilson's proposed associative memory design. A slightly modified version of the FPCR diagram provided in chapter 3 is reprinted in Figure 43 as a reference for the reader throughout the following discussion of the design, construction and alignment of the discrete optical feedback loop.

4.3.1.1 Design. When an object (e.g., a plate glass transmission pattern illuminated by a plane wave) is presented to the FPCR, an external lens generates the object's Fourier transform at point A in the lower feedback arm of the resonator. As described in Chapter 3, the mirrors M2 and M1 then produce a sequence of imaging, Fourier transforming and imaging operations at points B, C and D respectively. The output of the FPCR is produced by using an external Fourier transforming lens to generate an image from the object Fourier transform located at point C. M1 acts as a feedback element by coupling the Fourier transform of the image located at point D with the Fourier transform of the input object generated by the external lens.

As long as the beam path in the FPCR is not altered by an internal processing element, mirrors M1 and M2 will *always* redirect the feedback beam onto the input beam at M1 regardless of the input location and bias angle (assuming the internal beam does not exit the resonator). Additionally, because the focal lengths of M1 and M2 are identical, the size of the overlapping input and feedback Fourier transforms at point A are equal. Thus, the discrete optical feedback

loop design must simulate the Fourier transforming properties of M1 and M2 while ensuring the feedback beam rejoins the input beam in the proper direction and at the proper size.

The Fourier transforming properties of the FPCR were simulated using four lenses assembled as a lens waveguide as discussed in Chapter 3. The lenses were separated from one another by the sum of their respective focal lengths. The diameter of each lens (5 cm) was constrained by the size of the Oriel optical mounts used in the design. Although faster lenses would have enhanced the resolution of the output image, the Oriel mounts stabilized the gain performance of the $BaTiO_3$ crystal by minimizing beam fluctuations.

Feedback was achieved by using three plane mirrors and a 50/50 beamsplitter as shown in Figure 44. All optics were coated for uniform reflection/transmission characteristics about the operating wavelength of 514.5 nm. The mirrors were used to close the feedback loop as well as to maintain the proper separation distance between the four Fourier transforming lenses. The beamsplitter coupled the input and feedback beams and provided an image of the input object by reflecting roughly half the energy in the object wavefront through an externally placed imaging lens (not shown) and onto a screen. Recall that in the FPCR, M1 coupled the feedback and input beams *and* generated the Fourier transform of the feedback beam at point A in the resonator. The Fourier transform of the input object was generated by an external lens. In order to simulate this process with the discrete loop, the beamsplitter was positioned in the feedback arm so that the image at point D was a focal length away from point C. The beamsplitter then coupled the input object with its feedback image while L1 produced their Fourier transforms at point A.

The size of the images and Fourier transforms produced inside the FPCR is determined by the focal length of its mirrors. Similarly, image size in the discrete optical loop is determined by the focal length of the lenses. When an object is placed a focal length away from a two lens imaging system as shown in Figure 45, the size of the image in the back focal plane of the system equals the initial size of the object, h, times the ratio of the focal lengths of the lenses (i.e. $h \cdot \frac{f_2}{f_1}$). Furthermore, if an object is placed a focal length away from a four lens imaging system, such as our four lens waveguide, the size of the image in the back focal plane of the last lens equals $h \cdot \frac{f_2 f_4}{f_1 f_3}$. This relationship shows that in order to ensure the size of the output image equals the size of the input object (desired for system operation as explained later), the ratio $\frac{f_2 f_4}{f_1 f_3}$ must equal unity.

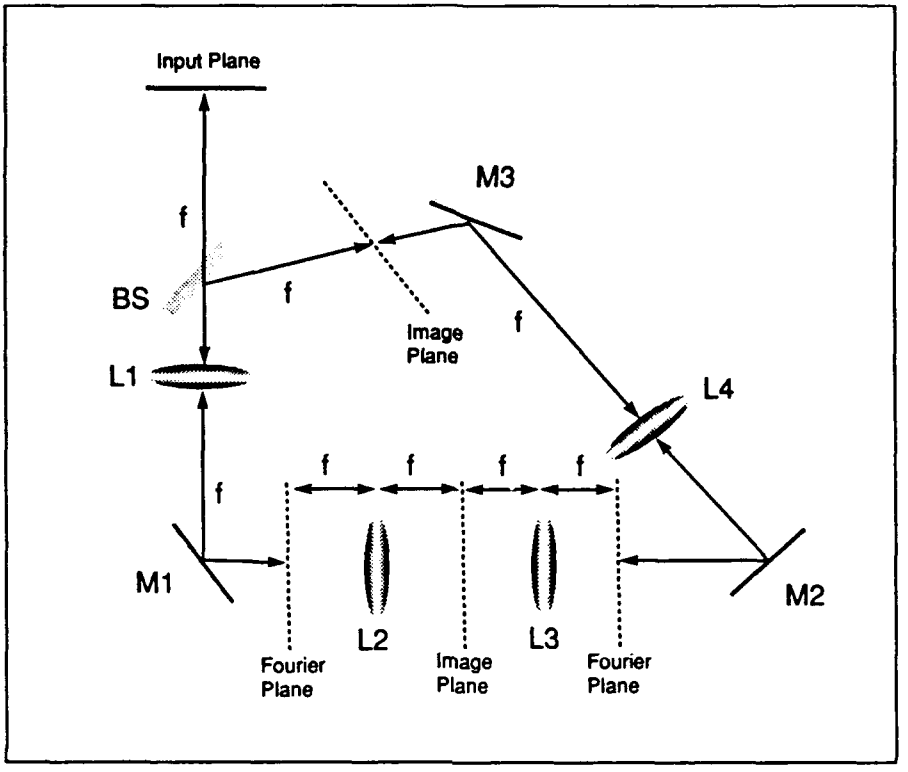

Figure 44. Model of FPCR processing environment constructed from discrete optical components.

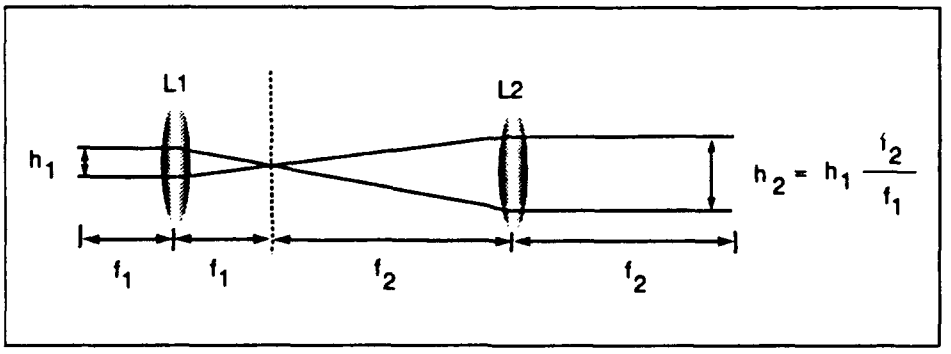

Figure 45. Two lens imaging system. The size of the image is determined by the ratio of the focal lengths of the lenses.

Obviously, a simple way to meet the above condition is to choose four lenses of equal focal length. However, two additional system design constraints preclude this possibility. The first constraint is imposed by the angle of the reference beam used in the holographic recording process. Figure 43 depicts the placement of the first $LiNbO_3$ at point A inside the FPCR. In order to simulate this situation in the discrete resonator, the first $LiNbO_3$ crystal must be placed a focal length in front of L1. As discussed in more detail later in this chapter, the angle multiplex recording scheme used in this thesis requires that the reference beam pass through L1 after it exits the $LiNbO_3$ crystal. If the reference beam angle is too large, or the focal length of L1 is too small, the reference beam will miss the lens. The reference beam angle used in the discrete architecture was approximately 15^o and the diameter of L1 was $2.5cm$; therefore, the maximum focal length for L1 is $10cm$.

A second constraint on the focal length of the lenses is imposed by the initial purpose of this phase of the thesis: to design a processing environment that provides enough space and flexibility to fully investigate the feasibility of Wilson's design. Constructing the system from four 10 cm focal length lenses would greatly reduce the amount of space available to observe and measure the behavior of each component in the proposed design. Therefore, a design was chosen that met the focal length constraint imposed by the 15^o reference beam angle, yet provided enough space to insert and maneuver the processing elements used in the F-OAM. This design (shown in Figure 46) used two 10 cm focal length lenses for L2 and L3, two 50 cm focal length lenses for L1 and L4, and also included a Fresnel beam sampler placed after L4 to simulate the output port in the FPCR architecture.

When a plane wave illuminates an object transparency placed in the input object plane of the discrete optical feedback system, the resulting wavefront travels to the 50/50 beamsplitter where a portion of its energy is reflected and imaged onto a screen. This image is used to monitor the placement of the object transparency inside the circularly shaped plane wave. The remaining energy contained in the input wavefront then passes through the two lens imaging system formed by L1 and L2. L1 produces a Fourier transform of the input object in the Fourier plane located 10 cm in front of L2, which in turn produces an inverted and minified image halfway between L2 and L3. The size of the image is one fifth the size of the input object. The image then travels through a second two lens imaging system comprised of L3 and L4. This imaging system produces a

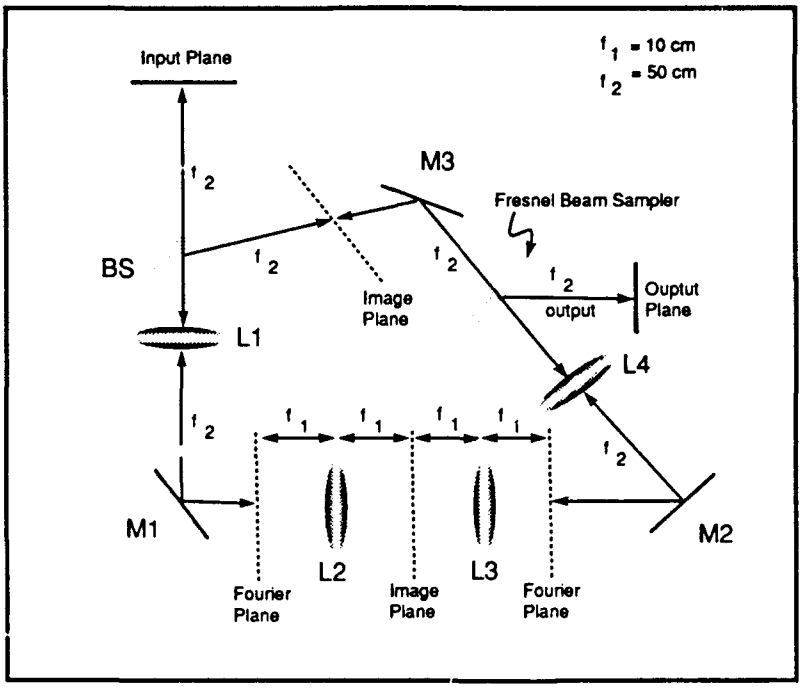

Figure 46. Final design for the discrete optical feedback loop used to model the FPCR architecture.

second Fourier transform, equal in size to the first Fourier transform, 10 cm behind L3. L4 then produces an erect image, equal in size to the input object, a focal length in front of L1. A Fresnel Beam sampler placed after L4 reflects approximately 10 percent of the feedback beam energy and produces an image on a CCD camera placed a focal length away from L4. The intensity of the image entering the camera is controlled by a variable neutral density filter. The image in the second image plane of the resonator is then coupled with the input object at the 50/50 beamsplitter. Because the input and feedback wavefronts are the same size and distance from L1, their Fourier transforms precisely overlap in the first Fourier plane of the resonator.

4.3.1.2 Construction. The optical feedback loop was constructed in three steps. First, the beamsplitter and mirrors were placed in their respective positions in the feedback system. Second, the mirrors were adjusted to provide a standard beam height throughout the feedback cavity. And third, the remaining optical elements were sequentially inserted in the feedback loop.

All optical components were mounted in standard Oriel optical mounts so that the center of each component was the same height above the optical bench. The 50/50 beamsplitter and all three mirrors were then placed as closely as possible to their final positions and firmly fixed to the optical bench with Oriel magnetic bases. An anodized aluminum beam block was placed in the feedback beam path after M1 and the system was illuminated with a spatially filtered and collimated beam wide enough to cover the central portion of each element ($\approx 2cm$). Two input mirrors used to control the direction of the beam exiting the spatial filter/beam expander and entering the feedback loop were then adjusted until the input beam measured the same height at the beamsplitter and M1.

The beam block was placed behind M2, and M1 was adjusted until the beam height at M1 and M2 were identical. This process was repeated with M2 and M3 until the beam traveled a standard height above the optical bench around the entire optical loop (beamsplitter to beamsplitter). The entrance mirror and the three internal mirrors were then adjusted until the beam reflected squarely off the center of each component in the system and the input and feedback beam spots overlapped at the beamsplitter face as shown in Figure 47. The direction the feedback beam travels when it reflects off the beamsplitter is not important at this time.

Having established a standard beam height around the feedback loop, the remaining optical

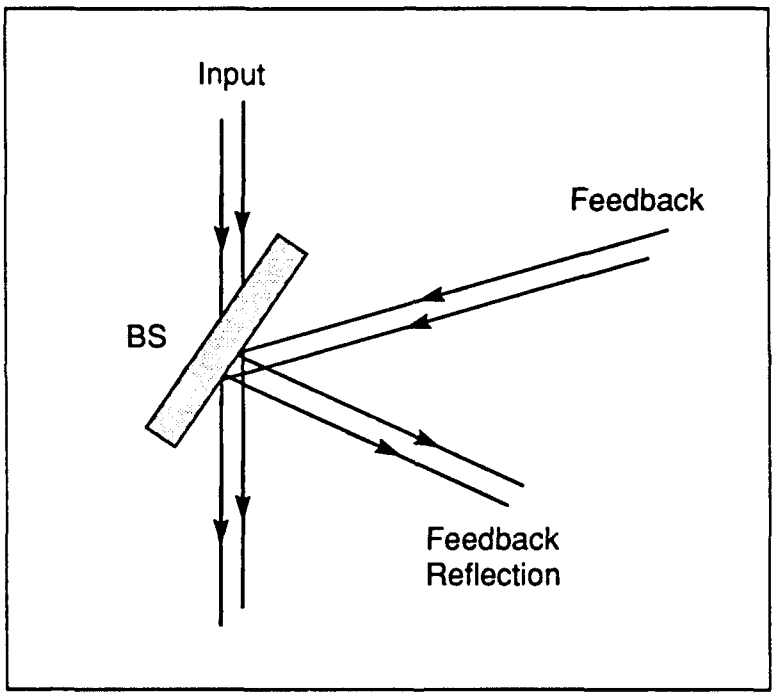

Figure 47. Aligning the input and feedback beams at the beamsplitter

components were added in sequence beginning with L1. L1 was positioned $50cm$ from the input object plane so that the input beam passed directly throughout the center of the lens. The lens was illuminated with the plane wave beam and its tilt was adjusted until the reflection off the lens face traveled directly back along the input beam path. The direction of the reflected beam was monitored by extinguishing the room lights and observing the relative positions of the reflected and input beam spots at the beamsplitter face.

Before adding L2, a $20cm$ diameter, optically flat, plane mirror was placed near the location of L3 and adjusted until the incident and reflected beams traveled along the same path. L2 was then inserted approximately $60cm$ from L1 and centered in the beam path. In order to locate the precise point on the optical bench at which the lenses were separated by the sum of their focal lengths, the spot size of the beam reflected off the optically flat mirror was monitored at the beamsplitter. As shown in Figure 48a), when the separation distance between the lenses does not equal the sum of their focal lengths, the spot sizes of the incident and reflected beams are not equal. However, when the lenses were precisely separated by the sum of their focal lengths, the incident and reflected beam diameters were equal (see Figure 48b). Having located this position, L2 was firmly anchored to the optical bench with a magnetic base and its tilt was adjusted until its incident and reflected beams traveled the same path. The same procedures were then used to add L3 and L4 to the system.

The last optical element added to the system was the Fresnel beam sampler. The beam sampler was positioned in the center of the feedback beam path approximately $10cm$ behind L4. The plane wave input was replaced with an AF resolution chart and the beam sampler's position and tilt were adjusted to direct the output beam onto a Sony CCD camera positioned a focal length way from L4. The lens of the camera was removed and the output was imaged directly onto the CCD array which was monitored on a monochrome television monitor placed above the optical bench. The intensity of the output image was controlled by a continuously variable neutral density filter. The CCD camera was mounted on a micrometer controlled translational stage which was adjusted until the resolution chart was focused on the television monitor. The resolution chart was then replaced with the collimated plane wave and the system was aligned.

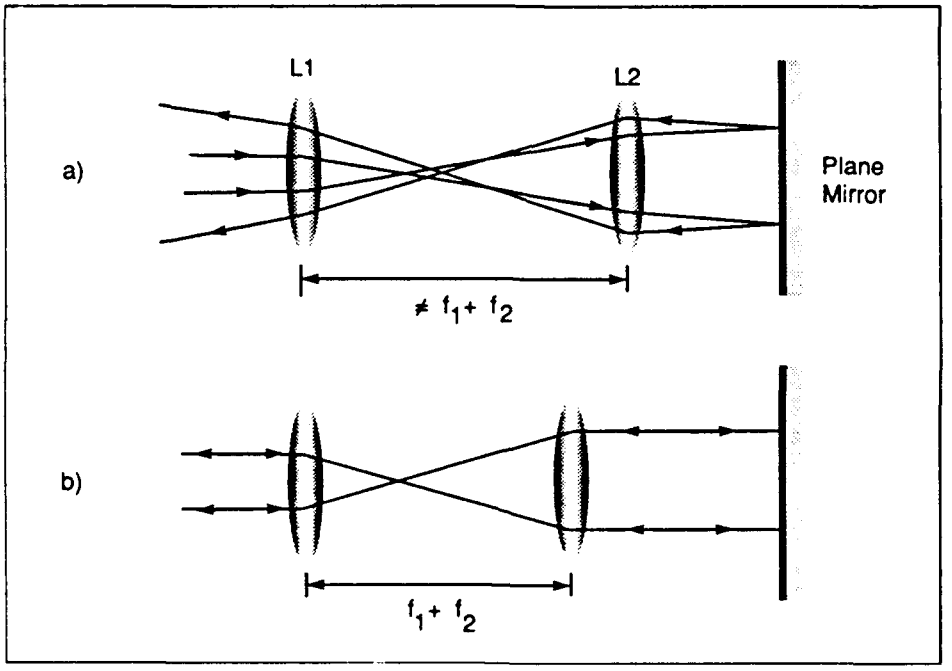

Figure 48. Plane mirror technique used to precisely separate two lenses by the sum of their focal lengths.

4.3.1.3 Alignment. One of the most difficult tasks in constructing an optical feedback loop is aligning the optical elements to ensure the feedback beam is perfectly superimposed (in size and propagation direction) on the input beam. Because the coherence length of the Argon-Ion laser was greater than the optical path difference between the discrete resonator's input and feedback arms, interferometeric principles were used to align the system.

When a plane wave traverses the feedback loop, each ray in the wave will experience a slightly different optical path length than its neighboring light ray. As discussed in Chapter 3, when the feedback and input rays combine at the beamsplitter, the variation in each ray's input and feedback optical path difference causes phase variations across the face of the superimposed beam. These phase variations create interference fringes in the output of the feedback loop. The pattern formed by the interference fringes indicates how well the resonator is aligned.

Figure 49 contains photographs of the resonator output for various alignment conditions. The photographs were obtained by imaging Output 2 in Figure 46 directly onto a frame of 1000ASA Polaroid film located in the back focal plane of a Calumet camera. When the resonator is both longitudinally and angularly aligned, the interference fringes form a bulls-eye pattern with a large circular central fringe. Phase variations across the center of the beam are minimized when the width of the central fringe is maximized. If the resonator is longitudinally misaligned, the central fringe of the bulls-eye pattern is small and the output contains many bright and dark fringes. An angularly and longitudinally misaligned system produces an asymmetric fringe pattern.

Throughout the construction process, the internal mirrors were continuously adjusted to ensure the input and feedback beams approximately overlapped at the beamsplitter. However, the direction the feedback back traveled after it reflected off the beamsplitter was ignored. In order to align the resonator, the input and feedback beams must overlap as they traverse the feedback loop. Therefore, the direction of the feedback beam as it reflects off the beamsplitter must be carefully controlled. This control was eventually achieved by iteratively adjusting the tilt of M3 and the beamsplitter, and the position of the lenses.

Figure 50 shows the fringe pattern observed on the monitor for four different stages in the alignment process. In the first diagram, the beams approximately overlap at the beamsplitter; however, the feedback beam does not reflect off the beamsplitter in the same direction as the input

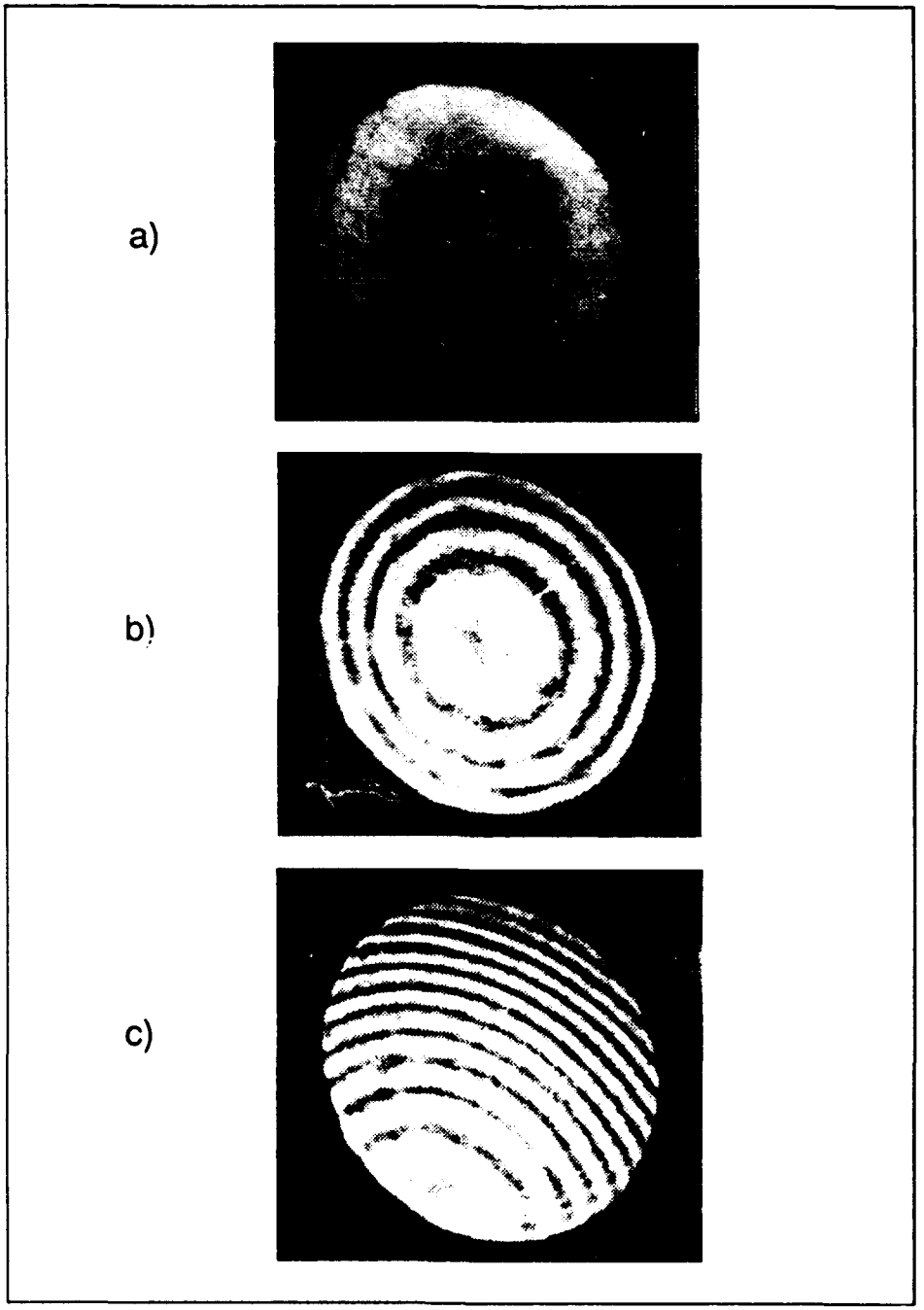

Figure 49. Interference fringes formed when a plane wave input and feedback beam combine in a discrete optical feedback loop that is a) angularly and longitudinally aligned, b) longitudinally misaligned, and c) angularly and longitudinally misaligned.

beam. Thus, no fringe pattern is observed on the monitor. In the second diagram, the beamsplitter tilt has been corrected to direct the feedback beam on top of the input beam; however, the input and feedback beams do not precisely overlap at the beamsplitter. Therefore, the fringe pattern is limited to the area of the beams that overlap. The third diagram depicts the asymmetric fringe pattern observed on the monitor when M3 and the beamsplitter have been adjusted so that the beams precisely overlap at the beamsplitter and throughout the resonator, but one or more of the lenses are not positioned precisely in the center of the beam path. Finally, the fourth diagram shows the bulls-eye pattern formed when the beams completely overlap as they travel along the optic axis of the system.

The central fringe in the bulls-eye pattern was maximized through longitudinal adjustments in the optical path length of the feedback arm. These adjustments were accomplished by mounting the beamsplitter on a micrometer controlled translational stage. By moving the stage in very small increments, while continuously adjusting the tilt of the beamsplitter and M3 and, when necessary, repositioning the lenses, the fringe pattern shown in Figure 49a) was eventually obtained.

The last experiment conducted in the discrete feedback loop before adding the associative memory components was to measure power losses experienced by the feedback beam as it traversed the resonator. A 5 mW, circularly shaped plane wave 1 cm in diameter was used as a system input and its power losses were measured after each optical component in the system. For a normally incident beam, the loss at each lens was approximately 2%. The mirror losses were each approximately 1%, and the losses at the Fresnel beam sampler and the beamsplitter were approximately 10% and 50% respectively. Because the beam reflects off the beamsplitter twice in a single pass (once as it enters the system and once when the feedback beam rejoins the input), the total system loss was approximately 80%.

4.3.2 Discrete Model of the Original System Design. Wilson's original system design was discussed at length in Chapter 3. In summary, the design included two $LiNbO_3$ crystals placed in the Fourier planes of the FPCR, and two $BaTiO_3$ crystals placed in the resonator's image planes. The $BaTiC_3$ attenuation element was placed in the first image plane immediately behind an array of spatial filters. The $BaTiO_3$ attenuation element was placed in the resonator's second image plane. In order to model Wilson's proposed internal alignment in the discrete optical feedback

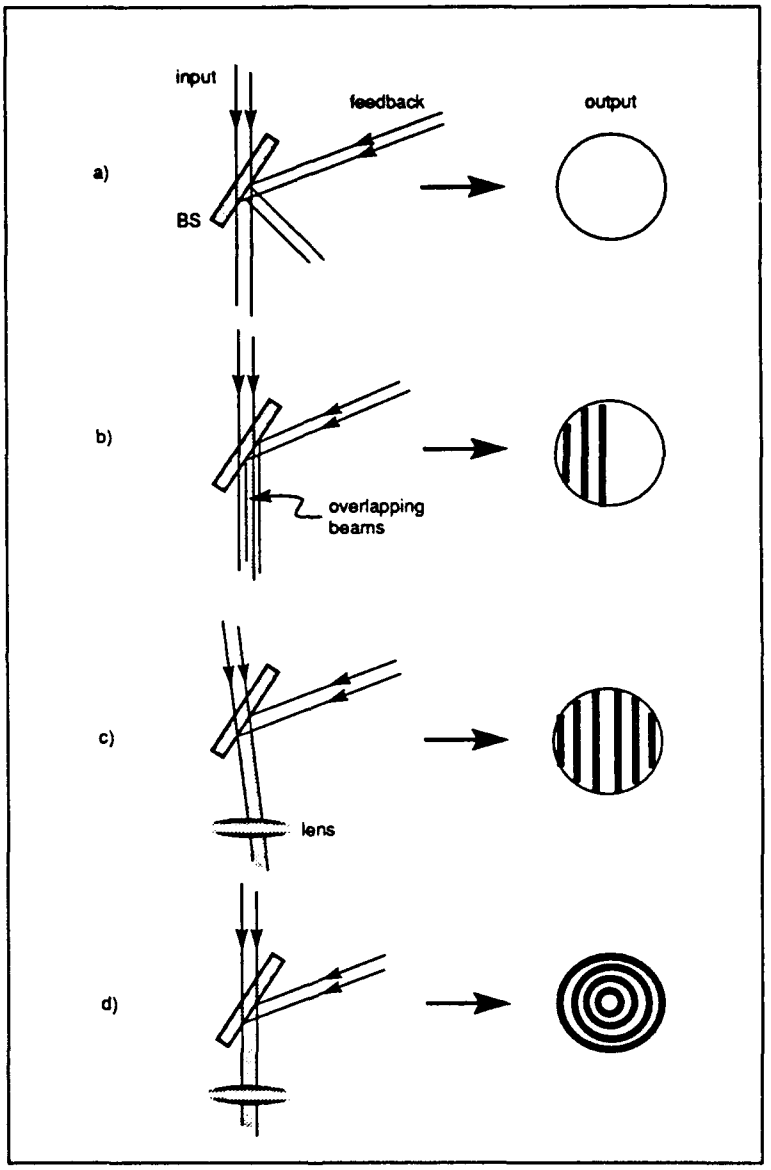

Figure 50. Interference fringes formed at Output 2 for each step overlap in the resonator. b) Beams do not precisely intersect at beamsplitter but overlap in the resonator. c) Beams completely overlap but travel off the optic axis. d) Beams completely overlap and travel down the optic axis.

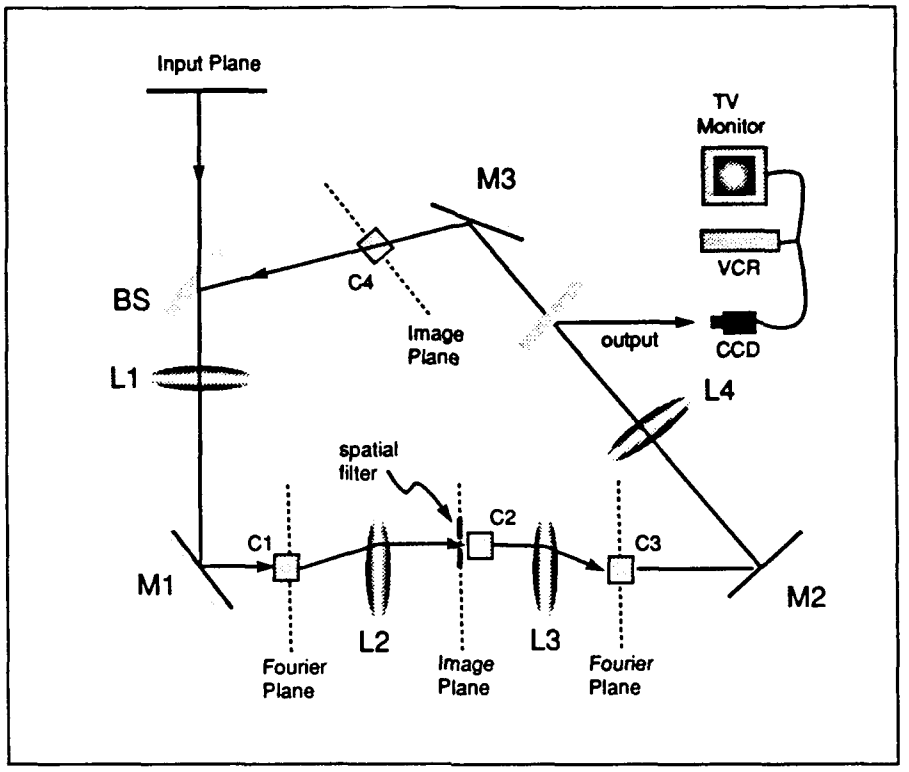

Figure 51. Placement of photorefractive crystals and spatial filter in the discrete system designed to model the F-OAM alignment proposed by Wilson.

loop, the crystals and spatial filters were placed in the locations shown in Figure 51.

A $LiNbO_3$ crystal was placed in the first Fourier plane of the discrete optical feedback loop located a focal length in front of L1. The spatial filter and attenuation element were positioned in the first image plane of the loop halfway between L2 and L3. A second $LiNbO_3$ crystal was placed in the second Fourier plane of the feedback loop located a focal length behind L3. Finally, the $BaTiO_3$ gain element was positioned in the second image plane located a focal length behind L4. The crystals were placed on turntable mounts in order to precisely control the orientation of their optic axes. The spatial filter initially consisted of a small pinhole, $0.71mm$ in diameter, drilled into a thin, rectangular aluminum plate.

4.3.3 Initial Design Tests. After constructing the discrete model of Wilson's proposed design, initial tests were conducted to determine its ability to store and recall a single object

from memory. The manner in which the object was stored in the memory is reported later in the chapter. However, two important test results that led to modifications in Wilson's original design are discussed here. The first test result demonstrates the current architecture cannot provide the gain needed to overcome system losses as the reconstructed reference beam travels from the first to the second $LiNbO_3$ crystal. This problem was eventually corrected by rearranging the internal components of the system. The second test result reveals the F- OAM architecture's inability to store and recall more than a single object from memory. This problem is believed to be a fundamental design limitation imposed by the FPCR optical processing environment and was, therefore, never corrected.

When a partial version of a single object stored in system memory was presented to the system, the reference beam used in the recording process was reconstructed at C1. The measured power in the reconstructed beam was typically no greater than 25% of the power in the distorted input object beam due to reflection and diffraction losses at C1. The reconstructed reference beam then passed through the attenuation element where an additional 55% of its power was reflected off the crystal face and another $10-15\%$ was attenuated in the two wave coupling process. When the reference beam finally reached the second $LiNbO_3$ crystal, experimental measurements showed the power in the reconstructed reference beam was approximately 98% smaller than the $18mW$ reference beam used in the recording process. The measured diffraction efficiency and reflection losses at C3 were $\approx 90\%$ so that the object reconstructed at C3 was barely, if at all, discernable in the optical noise produced during system operation.

In order to verify that the losses encountered as the reconstructed reference traveled between C1 and C3 were indeed the cause of the problem, the system was illuminated by the $18mW$ reference beam used in the recording process. The reference beam traveled through each element of the system, including the pinhole spatial filter, and illuminated C3 with $\approx 300\mu W$ of power. The output object reconstructed at C3 was intense enough to initially saturate the CCD. Thus, it was evident from these test results that system losses between C1 and C3 would have to be reduced and/or the power in the reconstructed reference beam would have to be amplified before it reached C2.

The second problem encountered during initial operational tests concerns the ability of the F-OAM architecture to store and recall more than a single memory. Recall from chapter 3 that

the intensity and size of each reference beam reconstructed at C1 and Fourier transformed into a high intensity peak in the image plane of the resonator is determined by a correlation process between its associated stored object and the distorted input. Because each high intensity peak is surrounded by auto-correlation noise, the separation distance between each reference beam in the resonator's midplane must be large enough to prevent the auto- correlation noise surrounding one peak from overlapping its neighboring peak. Wilson shows the minimum distance required to prevent overlap in the image plane is simply the sum of the widths of the stored and distorted input objects (35:21).

The widths of the stored and distorted objects used in the initial operational experiments were $3mm$ and $1.5mm$ respectively, yielding a minimum separation distance in the discrete resonator's image plane of $4.5mm$. Given that the maximum dimensions of the $BaTiO_3$ attenuation crystal are $5.5x6.5mm$, it's clear no more than one peak can pass through the crystal at a time. The problem even becomes worse when the effective size of the crystal's input face is reduced by rotating the crystal to achieve maximum attenuation. In this sense, the proposed architecture is essentially a single memory system.

4.3.4 Modifications to Original System Design. The experimental measurements described above show that losses sustained by the reconstructed reference beam as it travels between C1 and C3 severely limit the system's ability to recall objects from memory. In order to overcome these losses, the original design was modified by reversing the $BaTiO_3$ gain and attenuation elements. This eliminates losses experienced as the reference beam passes through the attenuation element while simultaneously providing a mechanism to overcome diffraction efficiency and reflection losses at C1 and C2. This arrangement also more closely resembles the architecture used by Stoll and Lee in which a $BaTiO_3$ gain element (as well as several additional Fourier transforming lenses) are placed between C1 and C3 (31). After rearranging the $BaTiO_3$ gain and attenuation elements, several alternatives were explored for expanding the system's capability to store and recall multiple memories within the design constraints imposed by the FPCR processing environment.

The first alternative required placing a separate gain crystal behind each pinhole in the spatial filter array. In this scheme, each crystal would be oriented and biased to so that each

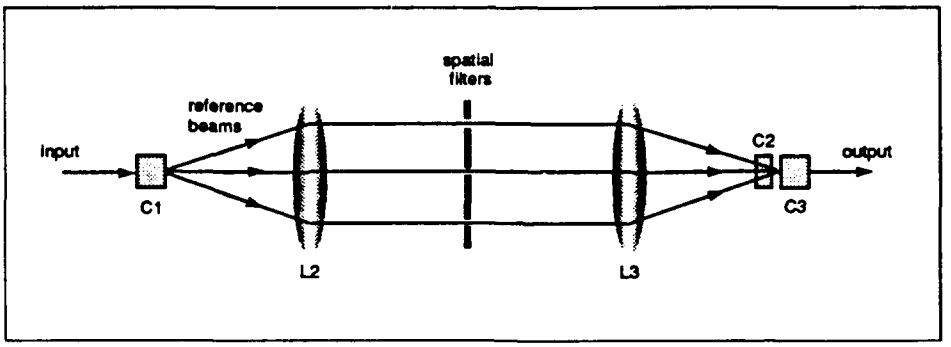

Figure 52. $BaTiO_3$ gain crystal positioned immediately in front of C3 is simultaneously illuminated by all reconstructed reference beams. This architecture was discarded when beam fanning noise generated by the gain element consistently washed out the object pattern reconstructed by C3.

correlation peak is equally amplified. However, based on preliminary experiments with $BaTiO_3$, it was determined the unique composition of each crystal would make it extremely difficult, if not impossible, to match their gain characteristics in order to equally amplify all reference beams. Therefore, a second alternative was explored in which the gain element was placed directly in front of the second $LiNbO_3$ crystal as shown in Figure 52.

Multiple reference beams reconstructed at C1, pass through the two lens imaging system formed by L2 and L3 and are recombined at C3. By placing the $BaTiO_3$ crystal slightly in front of C3, each of the reference beams pass through the gain element before intersecting at C3. In this way, one crystal might simultaneously amplify all reference beams. However, two problems prevent the implementation of the alternative. First, when the gain crystal is rotated to provide enough gain to overcome reference beam losses, the effective input surface area is decreased by the cosine of the rotation angle. This in turn reduces the number of reference beams that can pass through the crystal without reflecting off its sides. An even greater problem, however, is the intense pattern of beam fanning noise generated during the two wave coupling process. Because the $BaTiO_3$ crystal is placed so close to C3, practically all of the beam fanning noise exiting the gain crystal enters the $LiNbO_3$ crystal and quickly degrades the holographic grating formed during the recording process. Single memory experiments conducted with this architecture showed the reconstructed output was indistinguishable from the beam fanning noise. Because

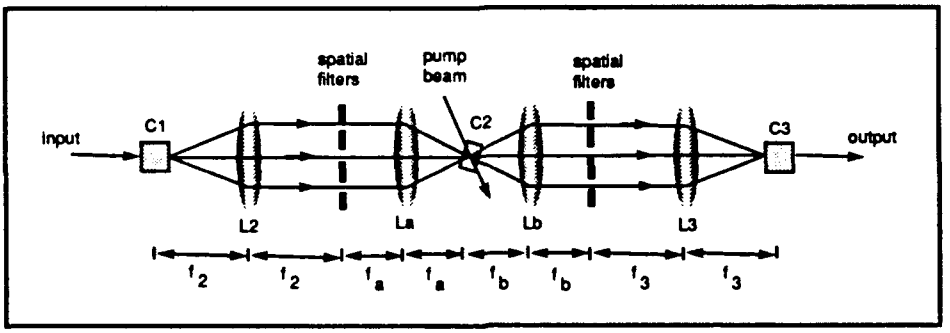

Figure 53. Major components in the $BaTiO_3$ gain element used by Stoll and Lee in their associative memory. The design ensures all reference beams intersect in the gain element.

beam fanning is a natural, and uncontrollable consequence of the two wave coupling process, this design alternative was discarded.

A third alternative for amplifying multiple reference beams with a single gain crystal is shown in Figure 53. A similar design was originally implemented by Stoll and Lee in 1988. (30). When multiple reference beams are generated by C1 in the above architecture, they are Fourier transformed into correlation peaks and spatially filtered just as they are in Wilson's design. However, a combination of two additional Fourier transforming lenses, La and Lb, are used to focus the reference beams onto a single, saturated gain crystal and then to transform them back into correlation peaks at the second spatial filter array. The peaks are then spatially filtered and focused by L3 onto the second $LiNbO_3$ crystal. Placing the gain crystal in front of the second spatial filter also serves to block the beam fanning noise before it reaches C3.

Although the above gain architecture could have been easily incorporated into the design of the discrete optical feedback loop, a practical way of incorporating the architecture into the FPCR processing environment was never found. Therefore, the gain architecture was never implemented in this thesis. However, one aspect of the architecture was employed to reduce the effects of beam fanning noise: the gain crystal was moved to a position just behind L2 in order to use the spatial filter array as a beam fanning noise block.

4.3.5 Final System Design. The placement of the internal processing elements in the final design of the discrete optical associative memory architecture is shown in Figure 54. As described above, the locations of the gain and attenuation elements are reversed from those proposed by Wilson in order to amplify the reconstructed reference beams leaving C1 before they reach C3. Also, the $BaTiO_3$ gain element, C2, is placed between L2 and the spatial filter in order to use the spatial filter as a beam fanning noise block. Note that the reference beam entering the gain element at this location is still converging. In Wilson's design the attenuation crystal was placed immediately behind the spatial filter so that the signal beam entering the crystal was essentially a high intensity point of light, capable of saturating the crystal gain medium. In the new configuration, the intensity of the still converging signal beam remains small enough to prevent the amplifier from saturating. As discussed above, the drawback to placing the gain crystal in this position is that only one reference beam can be amplified at a time. This precludes using this system for multiple memory storage and recall.

Each crystal is placed on a rotating turntable that allows precise control over the orientation of its optic axis to within 0.5°. The spatial filter is a $0.71mm$ diameter pinhole drilled in a thin, $4x6cm$ rectangular piece of aluminum large enough to block all beam fanning noise exiting C2. The filter is mounted on a cantilever arm attached to a micrometer controlled translational stage. The translational stage provides precise control over the location of the pinhole in the first image plane of the resonator. The cantilever arm allows one to easily remove and replace the filter during different phases of the system memory storage and recall process. The system output is imaged directly onto a Sony CCD array which is fed into a Panasonic S-VHS high density video recorder. A television monitor connected to the CCD camera allows real-time observations of the system output. Finally, a polarizer is placed in the object beam path just before C1 to ensure the input beam is extraordinarily polarized.

In addition to the optical components comprising the internal structure of the feedback system, an infrastructure of optical elements also had to be designed and assembled to provide pump beams for the gain and attenuation elements and a reference beam for the angle multiplex memory storage process. The complete system architecture, including this infrastructure of lenses, mirrors and beamsplitters, is shown in Figure 55. This figure will be referred to repeatedly throughout the remainder of this chapter.

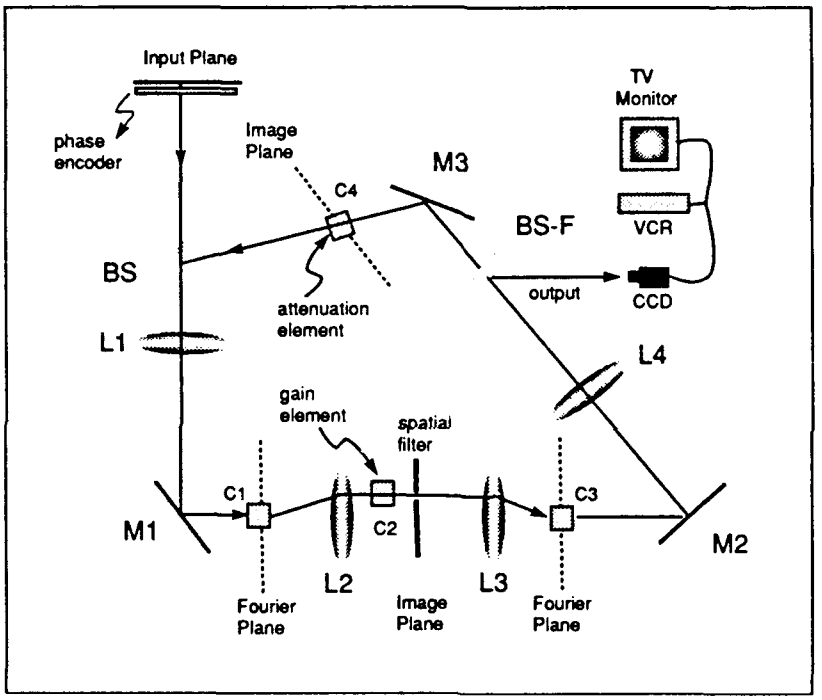

Figure 54. Diagram showing the final location of the internal processing elements in the final design of the discrete optical associative memory. C1 and C3 are $LiNbO_3$ memory storage and recall elements. C2 and C4 are $BaTiO_3$ gain and attenuation elements. The spatial filter is a $0.71mm$ diameter pinhole drilled into a thin rectangular piece of aluminum large enough to block all beam fanning noise exiting C2 during system operation.

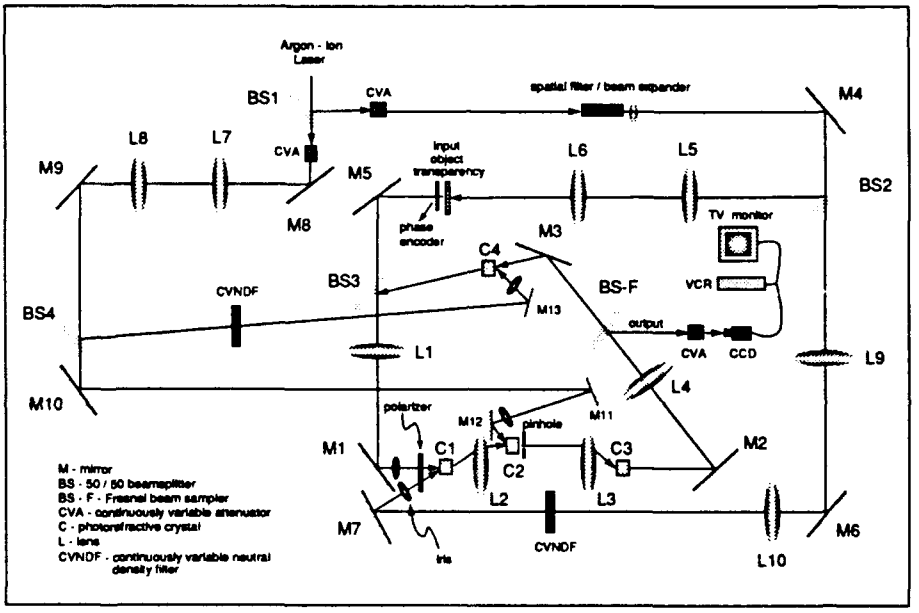

Figure 55. Diagram showing the placement of all optical elements used in the final design of the discrete optical associative memory. L1 - L4 are Fourier transforming lenses. L5 - L10 are imaging lenses used to control beam size.

In order to create an object beam, a reference beam, and two pump beams, the laser output had to be split into four arms. The object beam arm is formed by directing the laser output onto the object transparency using BS1, M4 and BS2. The continuously variable attenuator, CVA, controls the intensity of the beam and rotates the vertically polarized laser output 90^o. A spatial filter and beam expander filter out beam noise and provide an expanded, collimated input plane wave. The lenses L5 and L6 ($f = 20$ and $10cm$ respectively) are used to reduce the object beam diameter to approximately the same size as the object imprint on the plate glass transparency. An acid etched phase encoder is placed immediately behind the object transparency. As discussed above, the Fourier transforming lens, L1, forms a Fourier transform of the phase encoded object at C1. An adjustable iris placed in the object beam path just before C1 acts as a system aperture stop by controlling the size of the Fourier transform.

The reference beam arm splits from the object beam arm at BS2. The reference beam is minified using L9 and L10 which have focal lengths of 40 and 25 cm respectively. Mirrors M6 and M7 direct the reference beam through the polarizer and onto C1. M4 is mounted on a translational stage that provides control over reference beam's angle of arrival at C1. The spot size of the reference beam created by L9 and L10 is slightly larger than the input face of the crystal. Therefore, an adjustable iris is placed between M3 and C1 to control the size of the beam.

Both pump beams are formed from approximately 50% of the laser output that is transmitted through BS1. A continuously variable attenuator placed in this arm rotates the pump beam polarization to match the polarization of the object beam. Lenses L7 and L8 ($f = 12.5$ and $30cm$ respectively) expand and collimate the beam to a size slightly larger than the face of either $BaTiO_3$ crystal. Adjustable, circular irises are used to control the size of both beams as they enter each crystal. The pump beam for the attenuation element is formed at BS3. A one inch diameter plane mirror, M13, placed in an adjustable Newport mount, is used to direct the pump beam onto C4 and to control the beam's angle of arrival at the crystal. The pump beam for the gain crystal consists of the energy remaining in the pump beam arm after reflection losses at BS4. Plane mirrors M10, M11 and M12 direct the gain element pump beam onto C2. M10 is mounted on the corner of an adjustable Newport mount so it can be placed as closely as possible to C2 without interfering with the reference beam exiting C1.

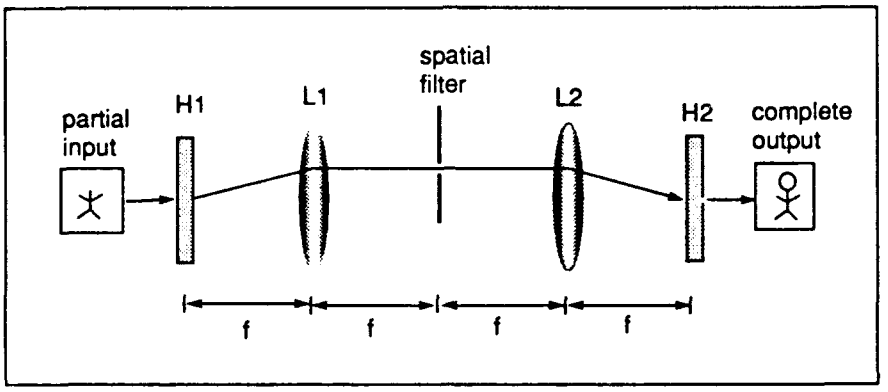

Figure 56. A typical optical associative memory holographic interconnect network. H1 and H2 are holographic storage media, L1 and L2 are Fourier transforming lenses.

4.4 Training the Associative Memory

Training an optical associative memory to recognize a group of objects is typically accomplished through an angle multiplex holographic storage technique (25) (26) (27) (30). This section begins by discussing the general concept of angle multiplex storage in a holographic interconnect network. The methodology used to train the discrete model of the F-OAM architecture is then presented, followed by an explanation of the procedures and parameters used to train the system to recognize a single object.

4.4.1 Angle Multiplex Holographic Storage The storage element in an autoassociative optical associative memory typically consists of two holograms, two Fourier or imaging lenses, and an array of spatial filters as shown in Figure 56 (26) (27) (30). This element shall be referred to as a holographic interconnect network.

Objects are stored in the holographic interconnect network through a holographic recording process known as angle multiplexing. In this process both holograms are recorded by either varying the location of each input object while maintaining a fixed plane wave reference beam (26,27), or by fixing the location of the input objects and varying the direction of each plane wave reference beam (13,25,30). The diagram in Figure 57 illustrates both techniques.

In the former technique (referred to here as simultaneous storage), an array of M off-axis objects are simultaneously presented to the system and a single plane wave reference beam is used

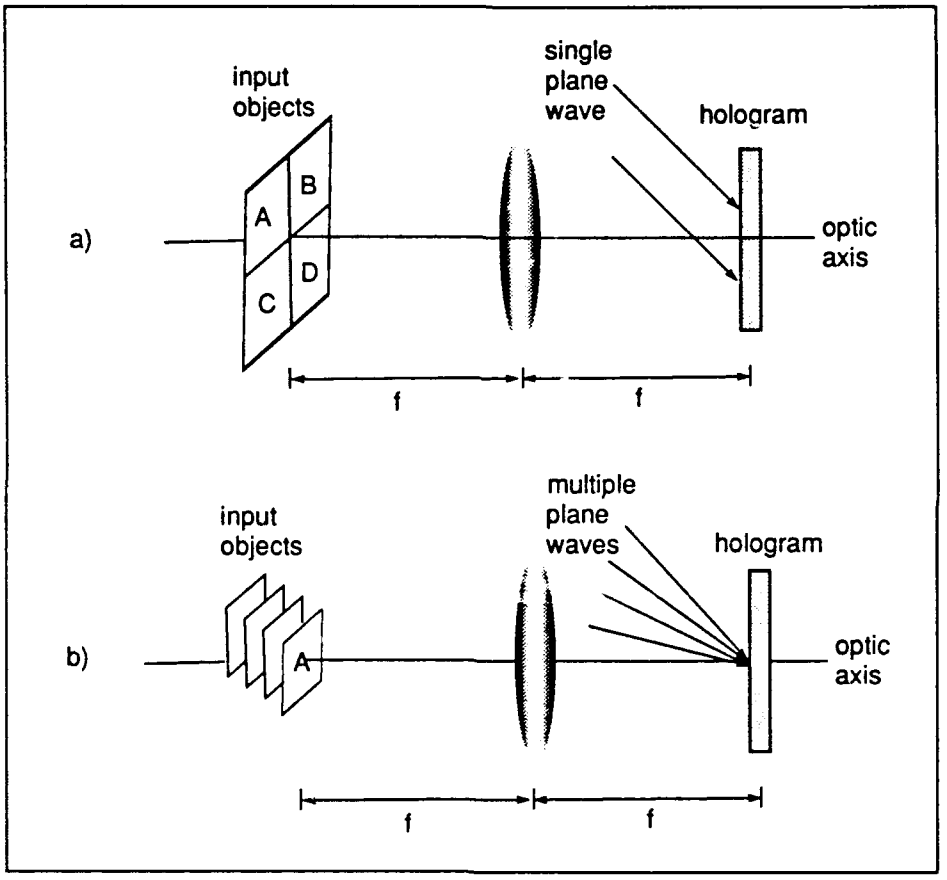

Figure 57. Two common holographic storage schemes in which a) position of input object is varied, reference beam direction is fixed, and b) location of input objects is fixed, reference beam directions are varied.

to record them on the holographic media. In the latter, or sequential storage technique, M objects are sequentially presented to the system from the same location and each object is recorded in the holographic media using a unique plane wave reference beam. The end result of both techniques is the same. When a partial version of a stored object illuminates the hologram, the output, when Fourier transformed, consists of an array of correlation peaks, separated in space, where each peak represents the correlation of the distorted input with each stored object.

In order to use the simultaneous storage technique, the holographic storage media must be insensitive to the phase of the stored object. This type of media is normally referred to as intensity sensitive. Intensity sensitive holographic media, such as a thin film hologram, responds to the intensity, rather than the phase, of a Fourier transform. Since the location of an object's Fourier transform is shift invariant, the hologram will respond to an on- axis input object that was stored in the hologram at some off-axis location. $LiNbO_3$, however, is a phase sensitive media. (13). That is, $LiNbO_3$ responds to the phase of the input object, and is, therefore, completely shift and rotation *variant*. If a distorted version of a stored object is not presented to the system in exactly the same location and orientation at which it was recorded, the volume hologram will not produce a correlation peak in the output Fourier plane. Therefore, although the simultaneous storage technique offers some advantages over the sequential storage technique, such as the ability to store many objects without changing input transparencies, it cannot be used in either of the architectures investigated in this thesis.

4.4.2 Training Methodology A photograph and accompanying diagram of the discrete associative memory's holographic interconnect network is shown in Figure 58. The interconnect network consists of two $LiNbO_3$ volume holograms, two 10 cm focal length Fourier transforming lenses, a $BaTiO_3$ gain crystal, and a pinhole spatial filter located halfway between both lenses.

The optical associative memory theory presented in Chapter 3 shows that objects must be stored in the holographic interconnect network in such a way that a reference beam reconstructed at C1 will read out its corresponding object from C3. Given that multiple memories must be stored in a volume hologram using the sequential storage technique discussed above, this implies each object must be recorded in both volume holograms using the same plane wave reference beam assigned to that object. The optical properties of the $LiNbO_3$ volume holograms, and the beam

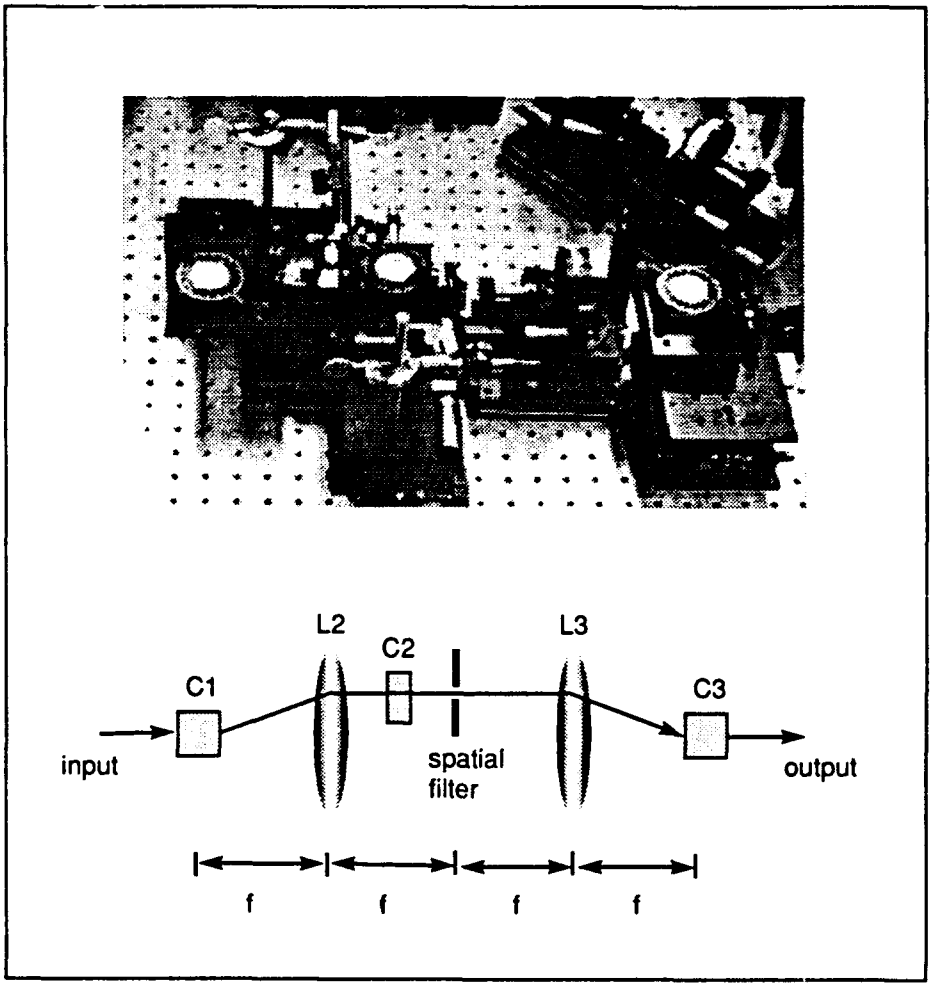

Figure 58. Digitized photograph (top) and diagram (bottom) of the discrete optical associative memory's holographic interconnect network. C1 and C3 are $LiNbO_3$ crystals, C2 is a $BaTiO_3$ gain crystal.

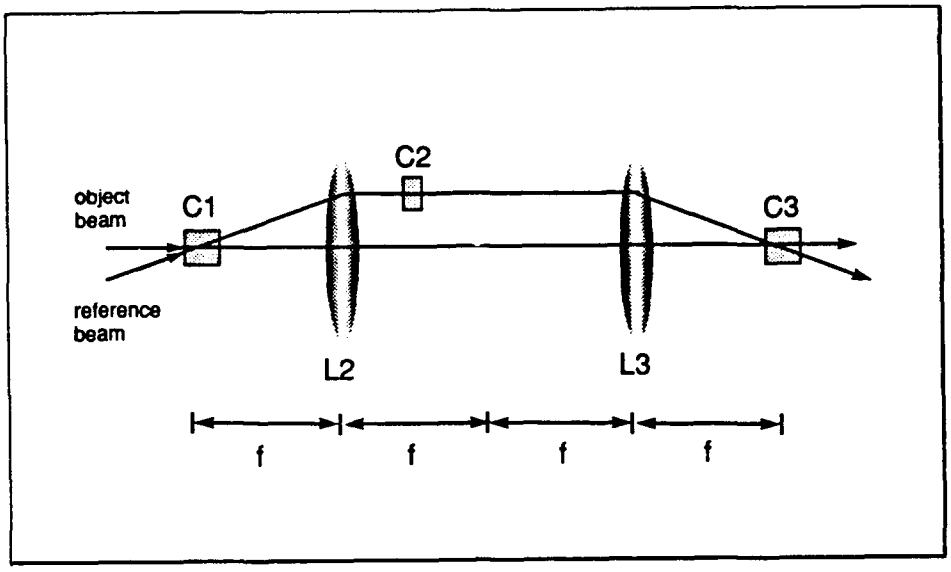

Figure 59. Diagram depicting how an object and reference combine in the holographic interconnect network to simultaneously record holograms in both $LiNbO_3$ crystals.

path characteristics of the holographic interconnect network make it possible to accomplish this by simultaneously recording an object in both volume holograms.

If the holographic storage media at C1 and C3 were intensity sensitive photographic plates, as originally proposed by Wilson, each plate would have to removed, developed and replaced in exactly the same position in which the holograms were recorded. If one wishes to add or delete an object from the system's memory, the above process must be repeated with a new set of photographic plates. $LiNbO_3$, on the other hand, is a dynamic holographic storage media. That is, new memories can be added to the crystal without removing it from the system. And, because the beams used in the recording process pass through a $LiNbO_3$ crystal attenuated but undistorted, they can be recombined at another location to record the same hologram in a second crystal. The optical properties of the holographic interconnect network are such that, two beams intersecting in the front focal plane of L1 will also intersect in the back focal plane of L2. Thus two $LiNbO_3$ crystals placed in the front and back focal planes of the interconnect network can be simultaneously recorded with a single object and reference beam. Figure 59 depicts this process.

Recall that the holographic interconnect network employed here also includes a $BaTiO_3$ gain crystal. It was discovered during preliminary experiments with the gain crystal that its input

and output faces are not parallel. A beam passing through the gain crystal is therefore altered in position and angle by refractive bending inside and at both faces of the crystal. Because $LiNbO_3$ is a phase sensitive storage media, it will only reconstruct a stored object if the beam used in the recall process is traveling in the same direction as the reference beam used in the recording process. Therefore, because the gain crystal alters the direction of the reference beam, it must be inserted in the system during the recording process. Furthermore, the gain crystal must be placed in the orientation used to provide gain during the recall process since rotating the crystal after the holograms have been recorded will alter the direction of the reconstructed reference beam arriving at C3. Another factor to consider is that the beam path deviations introduced by the gain crystal also cause the reference and object beams to combine at a location other than the back focal plane of the interconnect network. The placement of the second $LiNbO_3$ must then accommodate this deviation.

After some experimental trial and error, the methodology used to train the system to recognize a single object consisted of simultaneously illuminating both $LiNbO_3$ crystals with an object and reference beam while ensuring the reference beam exiting C1 passed through the pre-positioned gain crystal before reaching C3. The gain crystal was not pumped during the recording process to prevent beam fanning noise from degrading the holographic grating formed in C3. Additionally, because the spatial filter used to pass the correlation peak and block beam fanning noise also blocked the path of the object beam, it was not used during the training process. The procedures and parameter values used to train the holographic interconnect network are discussed in the following section.

4.4.3 Training Procedures The training process begins by removing all crystals from the holographic interconnect network. Assuming the system is aligned (i.e., the object beam travels down the optic axis and passes squarely through crystal C1, a plane wave reference beam is generated that 1) intersects the object beam at C1, 2) passes through the network's first Fourier transforming lens, and 3) lies far enough from the object beam in the network's image plane so that a gain crystal placed in its path will not interfere with the object beam. It helps here to place a white piece of paper, or a business card, at the location of C1 to ensure the object and reference beams intersect in the front focal plane of the interconnect network. The back focal plane of the

system should also be checked to ensure the beams intersect at C3. The external angle between the object and reference beams used in all experiments conducted in the discrete architecture was approximately 12°.

After generating a reference beam that meets the above conditions, the beam diameters of the circular object and reference beams are adjusted until they are both slightly less than the input face dimensions of the smallest $LiNbO_3$ crystal. The dimensions of the crystals used in this experiment were $1x1cm$ and $0.7x0.7cm$. Therefore, the object and reference beam diameters were set at approximately $6mm$. The diameter of each beam is controlled by two adjustable irises placed immediately in front of the input polarizer. The object beam iris is placed close enough to the Fourier plane of the resonator so that it acts as an aperture, rather than a field stop. After reducing the beam diameters to their required size, the power in each beam is measured by placing a detector at the intended location of C1. The variable neutral density filter is adjusted until the reference beam power is approximately six times as large the power in the object beam. This satisfies Frye's maximum diffraction efficiency recommendations summarized in Chapter 3. At full operational power, the object and reference beam powers just in front of C1 were measured at $3mW$ and $18mW$ respectively, yielding intensities of $10.6mW/cm^2$ and $63.6mW/cm^2$

The object and reference beams are both blocked and the first $LiNbO_3$ crystal, C1, is placed in the network with its optic axis pointing toward the output reference beam. From now on, the object and reference beams are never allowed to simultaneously illuminate the system in order to prevent the formation of spurious holographic gratings. Next, the reference beam is unblocked and C1 is rotated on the turntable mount until the reflection of the reference beam off the crystal face travels back along the path of the object beam. At this point, the bisector of the object beam and reference beam lies perpendicular to the crystal's optic axis as specified by Frye for maximum diffraction efficiency (13:16). The $BaTiO_3$ gain crystal, C2, is then positioned past L2 so that the reference beam leaving C1 passes through its center as it converges towards the image plane of the network.

The next stage of the network training procedure is somewhat tedious in that the gain crystal's position in the reference beam path, the location of the pump beam mirrors M11 and M12, and the direction of the pump beam must be carefully adjusted to obtain the 2° input beam separation angle required to achieve maximum two wave coupling gain. If viewed closely, the

photograph of the holographic interconnect network in Figure 58, shows M12 is mounted on the corner of an aluminum plate. This allows the mirror to be positioned as closely as possible to the reference beam passing through L1 in an attempt to minimize the angle between the reference and pump beams at C2. The pump beam arm shown in Figure 55 is unblocked and mirrors M10, M11 and M12 are adjusted until the pump and reference beams intersect inside the gain crystal. If the internal input beam separation angle (defined in Chapter 3) is not approximately 2^o, the crystal and mirror positions and the pump beam direction are varied until the separation angle is as close to 2^o as possible. The smallest internal input beam separation angle achieved here was approximately 3.7^o. The pump beam diameter is then adjusted with a variable iris to ensure the reference and pump beams interact throughout the length of the crystal.

After the size and angle of the pump beam are established, the gain crystal is removed from the system, the reference beam is blocked and a detector is placed in the pump beam path just past the location of C2 to measure the power of the reference and pump beams used in the two wave coupling process. The laser input power is increased to its operational value (in this case $2W$) and the continuously variable attenuator in the pump beam arm is adjusted until the pump beam intensity reaches the value required to bias the crystal for operation in its saturated gain regime. Preliminary crystal gain measurements presented earlier in this chapter show saturated gain operation is achieved when the input pump to signal beam ratio is approximately 10^5. Initial operational measurements revealed the power in the reconstructed reference beam was approximately $0.35mW$ after reflection losses at the gain crystal. Thus, a 10^5 pump to signal ratio would require a pump beam power of approximately $35W$. However, the maximum pump beam power available was only approximately $0.4W$, yielding an actual beam ratio of approximately 1000. The operational results presented in the next section show this input beam ratio, while substantially less than the ideal value, nevertheless produces a clearly discernable system output.

After adjusting the input intensity ratio for operation in the saturated gain regime, the $BaTiO_3$ gain crystal is replaced in its original position. The crystal is then rotated until the signal and pump beams just pass through the crystal without reflecting off its sides. This orientation provides the largest possible internal grating vector angle which in turn yields the largest possible crystal. The largest internal grating vector angle obtainable here was approximately 12^o. This orientation now determines where the object and reference beams intersect in the back focal plane

of the network, and, therefore, the location of the second volume hologram.

The point of intersection in the back focal plane was found by alternately blocking and unblocking the object and reference beams while moving an observation screen in the vicinity of the original intersection point until both beams intersected on the screen. The rotating turntable mount was then moved to the new location ($\approx 1.5cm$) behind the original intersection point and the second $LiNbO_3$ crystal was placed in the center of the turntable with its optic axis pointed in the direction of the output object beam. As before, the crystal was rotated until the reference beam reflected off the crystal face back along the direction of the input object beam. With all three crystals in place and properly aligned, the holographic interconnect network can now be trained. However, before doing so, the feedback loop must first be realigned to account for beam path deviations caused by refracting bending in the $LiNbO_3$ crystals.

When the $LiNbO_3$ crystals are added to the system, the object beam is slightly deviated from its original beam path, requiring realignment of the optical feedback loop. This problem is further complicated by the addition of the $BaTiO_3$ attenuation element which, like the gain element, has highly non-parallel input and output faces. In order to correct for these deviations the attenuation element is placed in the second image plane of the resonator at the internal grating vector angle (i.e., crystal orientation) desired for system operation. Like the gain crystal, the attenuation crystal is rotated until the object image just passes through the crystal without reflecting off its sides. As previously discussed, this orientation yields the most desirable attenuation characteristics. The object transparency is then removed and replaced with an adjustable iris in order to create a circularly shaped, plane wave object beam. As before, the CCD output is fed into a television monitor in order to observe the interference fringe pattern created when the input and feedback beams combine at BS4.

The resonator alignment procedures described earlier in this chapter are then followed while exercising extreme caution not to alter the input beam path or the alignment of the holographic interconnect network components. These procedures, however, are somewhat slowed by the presence of the attenuation element. Each time the resonator mirrors are adjusted to yield interference fringes at the output, the attenuation element must be shifted so it is once more in the center of the image plane beam path. Additionally, the pump beam must be continuously adjusted to provide the smallest possible beam separation angle and to ensure the object and pump

beams intersect at the attenuation crystal. This iterative process is repeated until the fringe pattern observed at the output is as symmetric as possible.

The characteristic bulls-eye pattern indicative of a perfectly aligned system was never achieved with the crystals used in this thesis. The photograph in Figure 60 demonstrates one reason for this behavior. This photograph shows the output interference pattern created when a single $BaTiO_3$ crystal (in this case, the gain crystal) is placed in the resonator. The fringe pattern indicates the crystal faces are not only non- parallel, they are also uneven. Mirror adjustments alone apparently will not compensate for the phase shift introduced by uneven crystal surfaces. Although time limitations prevented extensive investigation of methods that might correct this problem, future research efforts, particularly with multiple memory systems where feedback plays a critical role in system convergence, should consider placing the crystals in liquid crystal gates to compensate for the non-parallel, uneven nature of the crystals faces.

After aligning the complete system as well as possible, the holographic interconnect network was trained to recognize a single input object consisting of a transparent tank outline etched from an opaque plate glass slide. The training process began by blocking the input object and reference beams an increasing the laser power to its operational value of $2W$. This yielded a $3mW$ phase encoded Fourier transform object beam and a $18mW$ reference beam at the first $LiNbO_3$ crystal. Both beams were circular in shape with a diameter of $0.6cm$. Their respective intensities were $10.6mW/cm^2$ and $63.6mW/cm^2$. The feedback loop was also blocked in order to prevent the feedback beam from interfering in the recording process.

A plexiglass cage was placed around the architecture which completely shielded it from air currents that might induce deviations in the object and reference beam paths. The input beam blocks were then removed and the holograms were simultaneously recorded in both crystals for approximately 3 minutes. The beam blocks were then replaced and the laser power was reduced to a fraction of a watt. A low intensity reference beam was passed through the first $LiNbO_3$ crystal to mark the position of the correlation peak in the image plane. Recall that the correlation peak generated when a distorted input is presented to the system lies in exactly the same location in the image plane as the optical delta function obtained by Fourier transforming the plane wave reference beam. The spatial filter was then positioned so that the optical delta function passed directly through the center of the pinhole. A great deal of caution was taken during this procedure

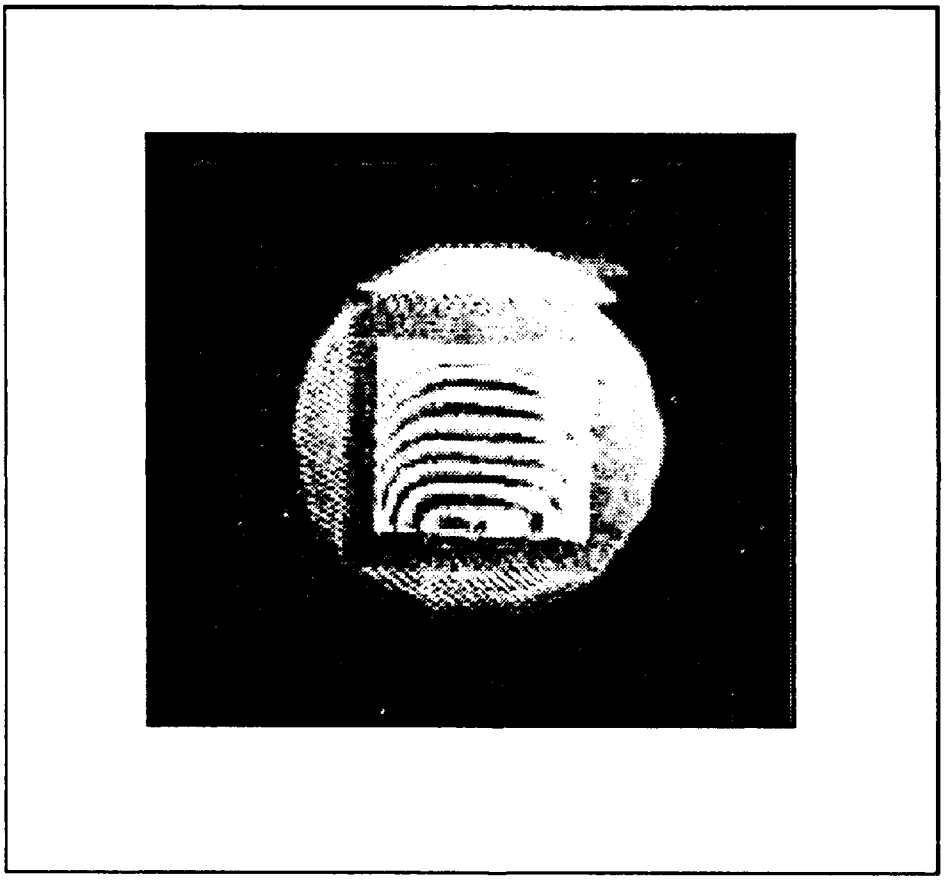

Figure 60. Fringe pattern observed when the $BaTiO_3$ attenuation element was placed in the FPCR. The fringe asymmetry suggests the crystal faces are non-parallel and uneven.

to ensure the internal components were not accidentally bumped. Preliminary experiments with the $LiNbO_3$ recording and recall process revealed minute deviations in the crystal alignment after recording a hologram eliminated any possibility of recall. Once the spatial filter was in place, the reference beam block was replaced, the feedback beam block was removed and a distorted version of the input object was presented to the system.

4.5 System Operation

In this section, the operation of the discrete optical associative memory is presented by following the input beam as it travels from the input object transparency, through each of the system's internal components and recombines with the input at the input beamsplitter. System results are also provided which show the system is capable of reconstructing a complete object from partial information about the object. Finally, possible explanations as to why the reconstructed output is less than ideal are discussed. One should note that the results shown below represent the last, and best, of several operational experiments. Any parameter changes made during previous experiments that enhanced the performance of the system are reported in conjunction with the appropriate stage of the system operation.

4.5.1 Stage 1 - Input object transparency to C1. The object transparency consisted of a tank etched onto an opaque plate glass slide. The 120 second acid etched phase encoder was placed immediately behind the transparency. The input object was created by illuminating the tank transparency with a collimated plane wave. A digitized photograph of the phase encoded object stored in the system memory is shown in Figure 61. Each of the digitized photographs contained in this section were obtained by imaging the system output directly onto a Sony CCD camera, recording the image on a Panasonic S-VHS high resolution video recorder, and digitizing the recordings using a NEXT computer and a $640 x 480 x 8$ bit Digital Eye digitizer. The speckle in the pattern is caused by the phase encoder, not by the recording or digitization process. A similar form of phase diffusion induced speckle was also reported by Paek and Psaltis (26:432). Based on preliminary experiments with phase encoded $LiNbO_3$ holograms, the glass slide etched in acid for 120 seconds was chosen for this experiment.

After storing the complete object in the associative memory, an incomplete version of the

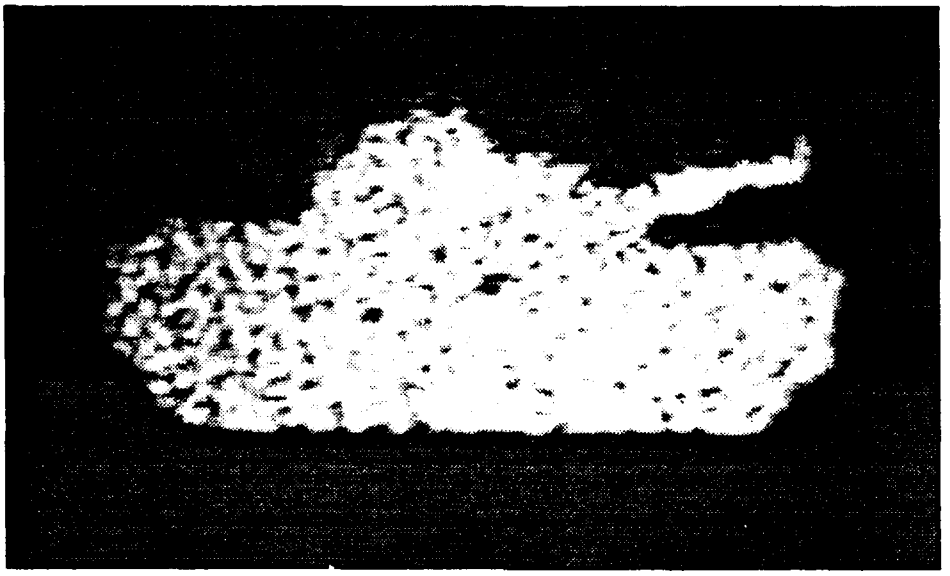

Figure 61. Digitized video recording of the phase encoded object solution for 120 seconds.

object was presented to the system. The incomplete object was formed by blocking a portion of the input beam immediately in front of the object transparency. A digitized video recording of the distorted input is shown in Figure 62.

The beam diameter (at C1) of the phase encoded Fourier transform of the incomplete object was approximately $6mm$ and the measured power was approximately $2.5mW$, yielding an object beam intensity of $8.8mW/cm^2$. In order to achieve this intensity level, the laser power was increased to its maximum single mode value of $2.5W$. The reference beam remained blocked throughout the experiment.

4.5.2 Stage 2 - C1 to C2. The beams reconstructed when the input object beam illuminated C1 included a DC term traveling in the direction of the object beam (which was eventually blocked by the spatial filter) and a plane wave traveling in the direction of the reference beam used in the recording process. The intensity pattern across the face of the plane wave was highly non-uniform, and looked identical to the central portion of the phase encoded Fourier transform stored in the crystal. Apparently, even using the strongest of the four acid etched phase diffusers, the higher spatial frequency components responsible for image quality (i.e., sharp edges) did not have enough

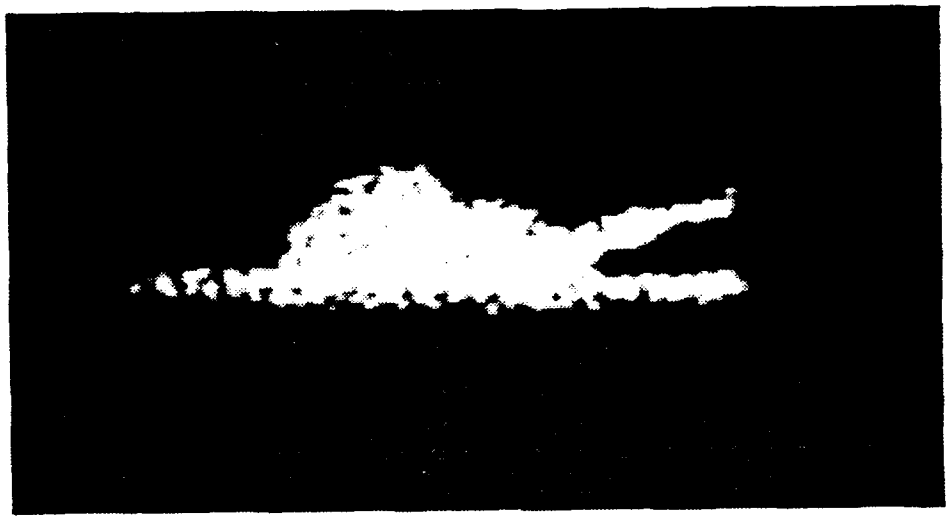

Figure 62. Phase encoded object presented to trained associative memory. Object is a partially complete version of the object stored in the system memory.

intensity to form a strong grating in the first $LiNbO_3$ crystal.

As discussed earlier, preliminary experiments with other combinations of phase diffusers showed they spread too much energy into spatial frequency components outside the dimension of the $LiNbO_3$ crystal. The Fourier transforms generated with these diffusers were highly uniform across the face of the crystal, but contained little power. Still, an attempt was made to improve the quality of the reconstructed reference beam by increasing the recording time used in the training process. However, because temperature variations and room vibrations occur throughout the recording process, it was found recording times exceeding 3 minutes resulted in poor quality object reconstructions. In fact, in order to produce reasonable quality reconstructions with 3 minute recording times, the experiments had to be conducted late in the evening when building vibrations were at a minimum. During the previously mentioned telephone conversation with Dr Harold Stoll, he stated they were able to achieve high quality, gray scale object reconstruction only after placing the $LiNbO_3$ crystals on very expensive mounts designed to isolate them from room vibrations. Dr Stoll also stated Hughes coated their crystals with anti- reflection material to reduce reflection losses encountered during training and operation. If possible, AFIT should procure similar isolation mounts and anti-reflection coated crystals before conducting follow on research with associative memory architectures that employ $LiNbO_3$ holographic media.

4.5.3 Stage 3 - C2 to the Spatial Filter. After reflection and diffraction efficiency losses at C1, the power in the reconstructed reference beam arriving at C2 was approximately $0.5mW$. The beam then lost another 55% of its energy from reflection losses at the face of the $BaTiO_3$ gain crystal so that the reference beam power actually entering the crystal was approximately $0.2mW$. As discussed earlier, the pump beam intensity was roughly 1000 times as large as the reference beam power, yielding a gain factor in the vicinity of 100. Thus, the gain element was able to easily overcome losses sustained by the $2.5mW$ input beam up to this point in the system operation.

The energy transferred from the pump beam to the reconstructed reference beam through two wave coupling in the $BaTiO_3$ crystal, was sufficient to create an intense correlation peak at the pinhole spatial filter surrounded by auto correlation noise generated by the convolution of the distorted input with the stored object. The correlation peak was further surrounded by beam fanning noise produced by the gain element. Both the auto correlation and beam fanning noise were blocked by the rectangular aluminum plate in which the $0.7mm$ diameter pinhole was drilled. In addition to the reference beam and the beam fanning noise, one could also clearly see the DC term that had exited C1 and was now being blocked by the rectangular plate. Thus the only energy allowed past the image plane of the resonator was that contained in the reconstructed reference beam and in the portion of the beam fanning noise that passed through the pinhole.

4.5.4 Stage 4 - Spatial Filter to C3. The beam exiting the pinhole spatial filter passed through the second lens in the interconnect network where it was Fourier transformed into a plane wave reference beam. The reference beam then illuminated C2 where approximately 40% was reflected back in the direction of the object beam. As before, the intensity profile across the face of the plane wave was highly non-uniform. Furthermore, the beam also included stray light rays from the beam fanning noise which, upon exiting the pinhole, traveled in the general direction of the reference beam. Based on measured reflection losses at the crystal face and spatial filtering losses at the pinhole, the power in the reference beam entering the crystal was approximately $3mW$, or, 1/6th the power of the reference beam used in the recording process.

4.5.5 Stage 5 - C3 to C4. As previously discussed, the reconstructed output object obtained during initial system tests consisted of a barely detectable "blob" of light that had the same general shape of the stored object but had no clearly defined edges. A digitized video

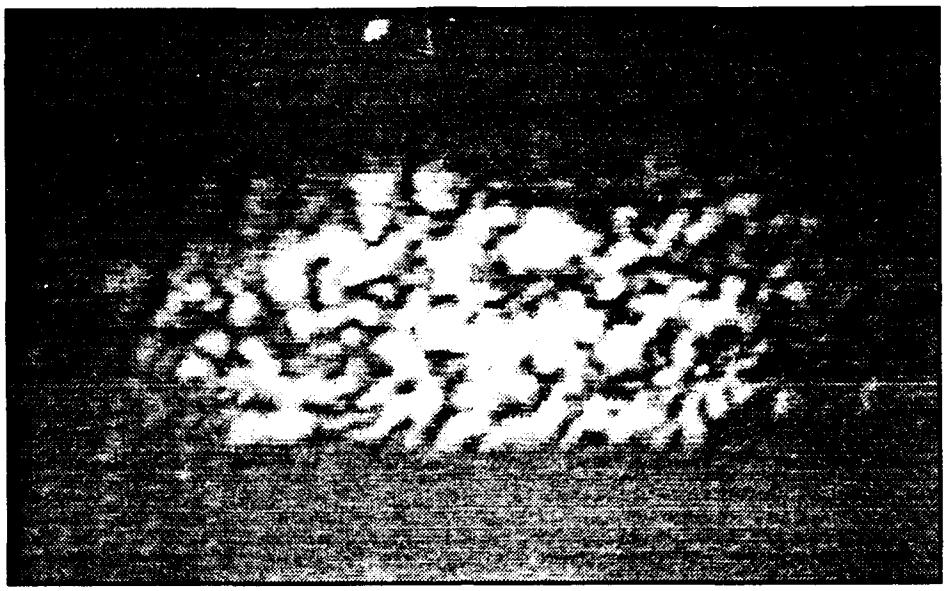

Figure 63. Digitized video recording of typical output obtained from initial operational experiments.

recording of an output generated from a typical initial system test is shown in Figure 63. After repeatedly experiencing the same results, separate storage and recall experiments were performed with the second $LiNbO_3$ crystal to determine the cause of the problem.

It was found during these "off line" tests that the system output could be improved by increasing the intensity and size of the reference beam reconstructed at C1. Several steps, many of them discussed earlier, were taken to achieve these goals. These included: increasing the laser power used to train and operate the system to its maximum value, employing a stronger phase diffuser that spread more energy into the object's higher spatial frequency components, placing the gain crystal closer to the spatial filter (where the beam diameter of the converging reference beam was smaller) in order to obtain smaller separation angles and larger grating vector angles, replacing BS3 with a Fresnel beam sampler to increase the intensity of the gain crystal's pump beam, and increasing the recording time from 1 to 3 minutes. With each change in the system architecture, the associative memory was retrained before conducting the next operational experiment.

The results obtained by making the above changes are shown in the digitized video recording contained in Figure 64. The edges in the reconstructed object are not as sharply defined as the

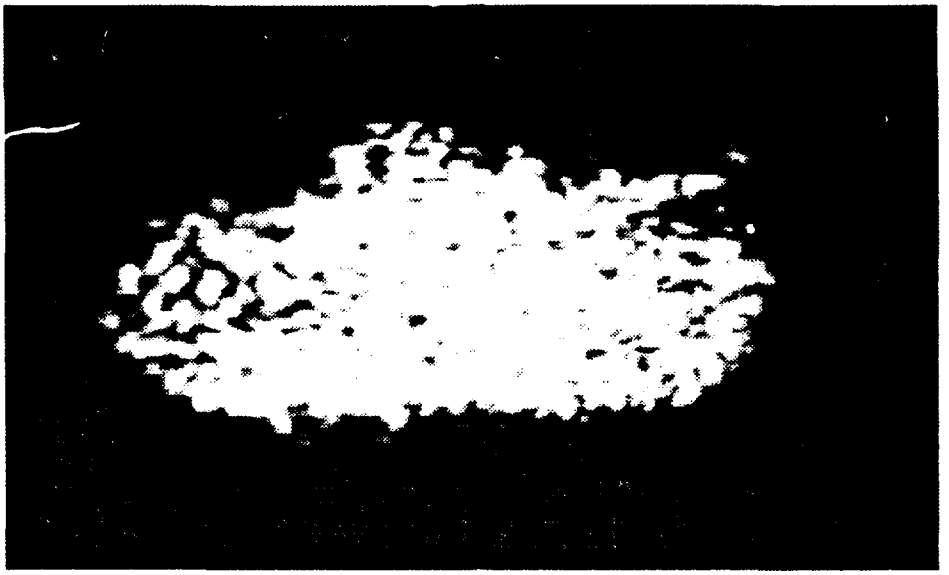

Figure 64. Digitized video recording of the complete object reconstructed from system memory after modifying Wilson's original design to improve system's signal to noise performance.

object stored in memory, however they are clearly visible. The intensity of the reconstructed output was large enough that it saturated the CCD camera and had to be reduced using a variable neutral density filter. As reported by Paek and Psaltis, the speckle in the reconstructed object is caused by the phase diffuser, while the stray light surrounding the object is believed to be beam fanning noise that passed through the spatial filter pinhole. A great deal of this noise was eliminated by increasing the strength of the variable neutral density filter placed in front of the CCD camera. Approximately 10% of the energy in the reconstructed object exited the system at the Fresnel beam sampler to form the output shown above. The remaining energy in the output beam then traveled to C4.

4.5.6 Stage 6 - C4 to Input Coupler BS4. Diffraction efficiency calculations made during the separate $LiNbO_3$ experiment described above, show that for the object and reference beam powers used to record the object in the second $LiNbO_3$ crystal, the diffraction efficiency (accounting for losses at the crystal face) was approximately 15%. Thus, the $5mW$ reference beam arriving at C3 produced approximately a $750\mu W$ output object beam. Assuming 10% of this

power was lost at the Fresnel beam sampler, the power in the reconstructed object beam arriving at C4 was then approximately $700\mu W$.

Based on the attenuation data gathered during the preliminary experimental stage of the thesis, in order to pass the $700\mu W$ object beam with less than 10% attenuation, the intensity of the object beam must be greater than 1000 times as large as the intensity of the attenuation element's pump beam. Since the pump and object beam spot sizes were approximately equal, this implies the pump beam power should be less than $7\mu W$. In order to reduce the power in the pump beam to these levels, a variable neutral density filter and several fixed plated glass neutral density filters were placed in the pump beam path shortly after it left the Fresnel beam sampler at BS3.

When the object beam illuminated the attenuation element, approximately 55% of its energy was reflected off the crystal face. The remaining energy then passed through the attenuation element where a portion was transferred into the pump beam. No attempt was made to measure the power in the attenuated output; however, their was enough energy in the output beam to make the object clearly visible on a card placed after the crystal during system operation. Because the discrete architecture employed in this thesis will only support a single stored memory, no attempt was made to optimize the crystal's attenuation characteristics for multiple memory operation.

4.6 Conclusion

The experimental research leading up to the construction and operation of the discrete optical associative memory began with an investigation into the gain and attenuation characteristics of the $BaTiO_3$ crystals employed in this system. A discrete model of the Fabry-Perot confocal resonator was then built using lenses, plane mirrors, beamsplitters and Fresnel beam samplers. After aligning the resonator, the internal components were placed inside the loop and an optical infrastructure was constructed to support the two wave coupling and holographic storage process. Initial operational experiments revealed the system was not able to produce a complete and clearly identifiable output object when presented with a distorted version of the object. Additional tests were performed which showed the system lacked the gain and holographic diffraction efficiency required to produce a clearly discernable system ouput. Based on these tests, several changes were made in the architecture including the realignment of the $BaTiO_3$ gain and attenuation elements and the addition of a phase diffuser made by etching a glass slide in hydrofluoric acid. The

final system results show the associative memory was capable of reconstructing a complete object stored in memory when presented with a partial version of the stored object. The next chapter of the thesis describes how the knowledge gained from experiments conducted in the discrete system was used to construct and successfully operate the Fabry-Perot Confocal Resonator Optical Associative Memory.

V. Fabry-Perot Confocal Resonator Optical Associative Memory

5.1 Introduction

The experiments performed up to this point formed a strong foundation for the work accomplished in this phase of the thesis. The optical components used in the discrete associative memory did indeed accurately model the behavior of the Fabry-Perot Confocal Resonator, and the final design of the discrete system's internal processing elements (i.e., photorefractive crystals and spatial filter) were imported, intact, into the FPCR optical processing environment. Because the internal design of both system's were identical, much of the operational behavior of the discrete system discussed in the previous chapter also applies to the F-OAM. Therefore, this chapter places less emphasis than Chapter 4 on the operational characteristics of the internal elements in the architecture, and, instead, focuses more attention on the overall design and operation of the F-OAM system.

The second section of this chapter examines key problems uncovered during discrete associative memory experiments that impact the design and operation of the F-OAM. These include problems associated with the operation of both the internal and external design components. The chapter's third section describes the F- OAM design in detail, highlighting the unique design changes made to overcome the above problems. The fourth section describes the methodology used to train and operate the F-OAM and presents the results obtained when a partial version of an object stored in memory was presented to the system.

5.2 Key Problems Uncovered During Discrete System Experiments that Impact the F-OAM Design.

Experiments conducted with the discrete associative memory architecture revealed several key problems that prevented it from initially operating as planned. Some of these problems, such as cavity power losses between C1 and C3 and degraded reference beam reconstruction at C1, were solved by modifications to the discrete system design that naturally carried over to the F-OAM architecture. However, several other problems uncovered during these experiments were corrected by unique design changes that could not be directly imported to the F-OAM. These included path deviations that occur when the feedback beam travels through each of the photorefractive crystals,

object beam power losses inside and outside the optical feedback loop, and signal degradation effects caused by beam fanning noise. This section briefly discusses the impact each phenomena has on the F-OAM architecture.

5.2.1 Feedback Beam Path Deviations. In order for an optical associative memory that employs feedback to operate correctly, the feedback beam must combine with the input beam so that the two arrive precisely superimposed at the first holographic storage element. If the feedback beam is slightly deviated as it traverses the feedback cavity, the beams will not precisely recombine and, theoretically, the system will not converge on the stored object that most closely matches the distorted input. This is a particularly troublesome problem with the architectures investigated here because they contain photorefractive crystals that alter the feedback beam path in both angle and position due to the refractive nature of the crystal media and the non-parallel geometry of the crystal faces.

Figure 65 depicts how the direction of the feedback beam is altered as it passes through one of the four photorefractive crystals. In Figure 65a), the crystal faces are parallel and the beam path is altered only in position (i.e., translated) due to refractive bending in the crystal. In Figure 65 b), the crystal faces are not parallel and the beam path is altered in both position and angle. Correcting deviations in position and angle requires a compensation system with four degrees of freedom. Because each of the four corner elements in the discrete loop have three degrees of freedom, it was possible to restore the deviated beam to its original path by iteratively adjusting two of the four elements (i.e., M3 and the beamsplitter).

The mirror system used in the Fabry-Perot Confocal Resonator, however, does not allow one to correct internal beam path deviations because of the symmetry of the architecture. Any attempt to restore a beam to its original direction by adjusting one mirror is automatically compensated for when the beam reflects off the opposite mirror. In this sense, the confocal mirror system has 0 degrees of freedom. Thus a separate compensation element with four degrees of freedom must be inserted into the system to correct for translation and angle deviations incurred as the beam travels through each of the four crystals.

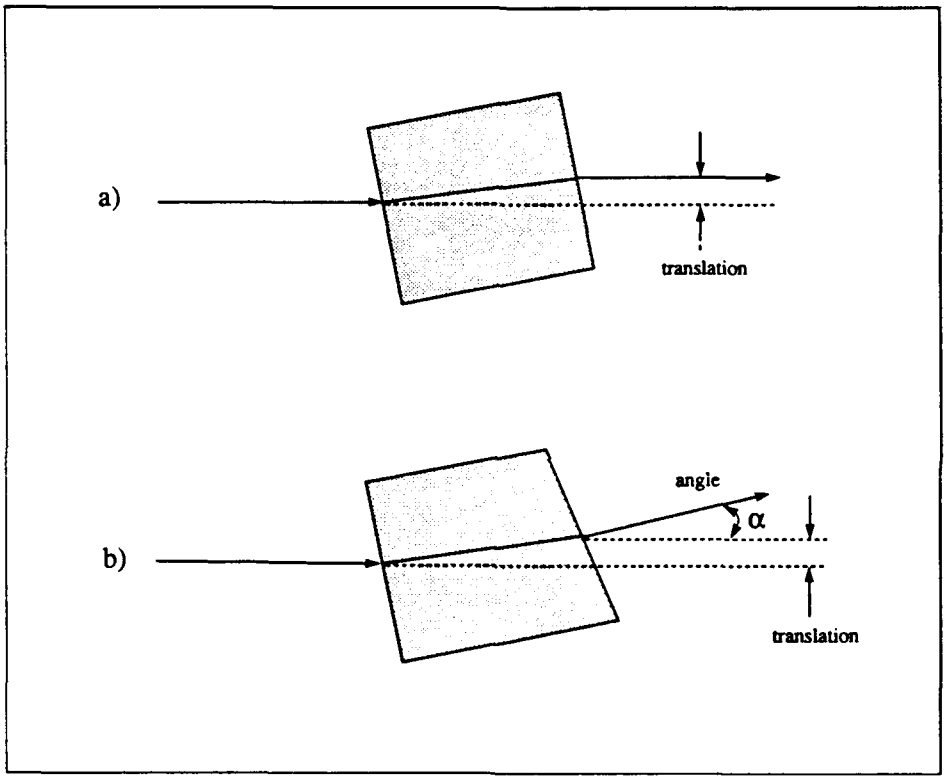

Figure 65. When a beam passes through a photorefractive crystal, its position and angular direction are altered by a) refractive bending inside the crystal, and b) the non-parallel geometry of the crystal faces.

5.2.2 Power Losses. Experiments conducted in the discrete resonator show the ability of the associative memory to reconstruct a clearly discernable object from memory is strongly dependent on the power of the object and reference beams used to train and operate the system. Both are affected by the transmission and reflection characteristics of the optical components used to form the feedback loop and external optical insfrastructure.

Frye experimentally showed the diffraction efficiency of the holographic recording process is maximized for an input object to reference beam ratio of approximately 6 to 1 and a combined beam power of $35mW$, for beam diameters approximately equal to those used in the associative memory (13). However, these power levels were never reached in the discrete architecture because of losses imposed by the phase diffuser and the 50/50 beamsplitter used to couple the input and feedback beams. Even with a maximum laser power of approximately $2.5W$, the power in the input object beam was less than $3mW$.

The result of these losses was that the holographic recording time used to train the system had to be increased to two minutes from Frye's value of 60 seconds. The additional recording time ensured the gratings formed in C1 were strong enough to reconstruct spatial frequencies higher than the DC or near DC components of the object stored in C3. This power loss problem in the F-OAM is exacerbated by the transmission characteristics of the mirrors used in the FPCR which allow only 5% of the input object beam energy to enter the cavity, or, roughly 1/10th the energy passed in the discrete architecture. Thus, in order to achieve the same diffraction efficiencies in the holograms stored in the F-OAM as those achieved object beam power must be increased.

Previous experiments conducted in the discrete architecture yielded low quality output objects for recording times exceeding approximately 3 minutes because of beam and crystal vibrations that naturally occur during the recording process. Because it's virtually impossible to eliminate these vibrations without the aid of expensive table-top isolation mounts, more emphasis was placed on redesigning the supporting optical infrastructure to increase the input object beam power than on implementing the modifications required to increase the recording time.

5.2.3 Beam Fanning Noise. When the pump beam illuminated the gain crystal during operation of the discrete system, a portion of its energy was scattered and amplified to produce an intense beam fanning noise pattern. It was found the intensity of the noise was large enough

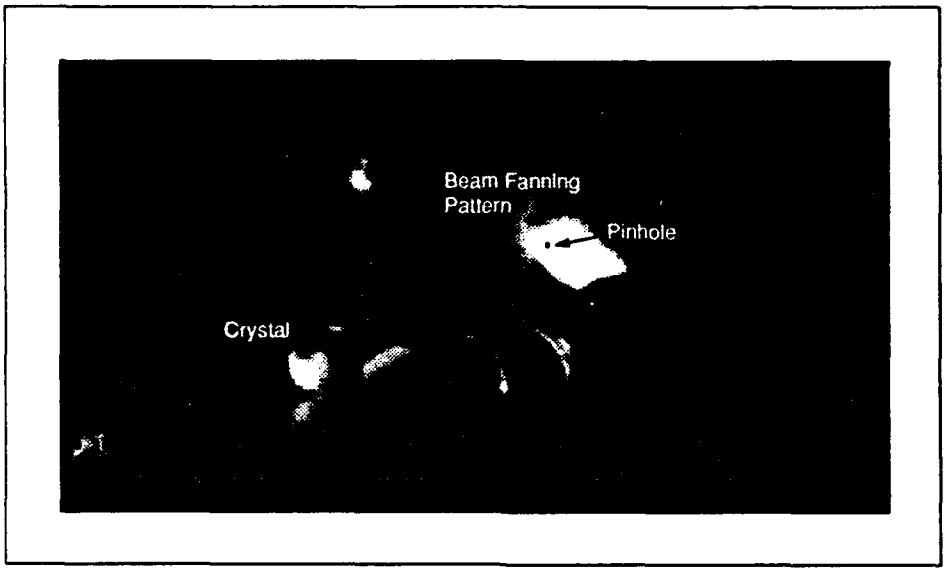

Figure 66. Beam fanning pattern produced when an intense pump beam illuminates a $BaTiO_3$ crystal. Pattern width is approximately 1.5 cm.

to quickly degrade the refractive index gratings formed in C3 during the training process and to wash out the reconstructed object pattern viewed on the television monitor. In order to alleviate this problem, a pinhole was drilled into a large aluminum plate that spanned the entire image plane to block nearly all the beam fanning noise before it reached C3. Figure 66 contains a photograph of the beam fanning pattern as it strikes the plate. For the crystal orientation used in the discrete system, the pattern was approximately 1.5 cm in diameter.

The F-OAM employs the same gain crystal orientation and pump beam intensity used in the discrete associative memory. However, the smaller processing space limits the size of the beam block that can be inserted in the feedback beam path. Figure 67 shows the dimensions of a typical object beam path in the F-OAM. Clearly, the aluminum plate used in the discrete system is too large for use here. In fact, the diameter of the beam fanning pattern is nearly half as wide as the outer edges of the input and feedback beam path, precluding the insertion of a beam block large enough to completely block the entire fanning pattern. Thus, the design of the F-OAM must attempt to minimize the effects of beam fanning on crystal C3 while allowing the input, reference, pump and feedback beams to travel unimpeded throughout the resonator.

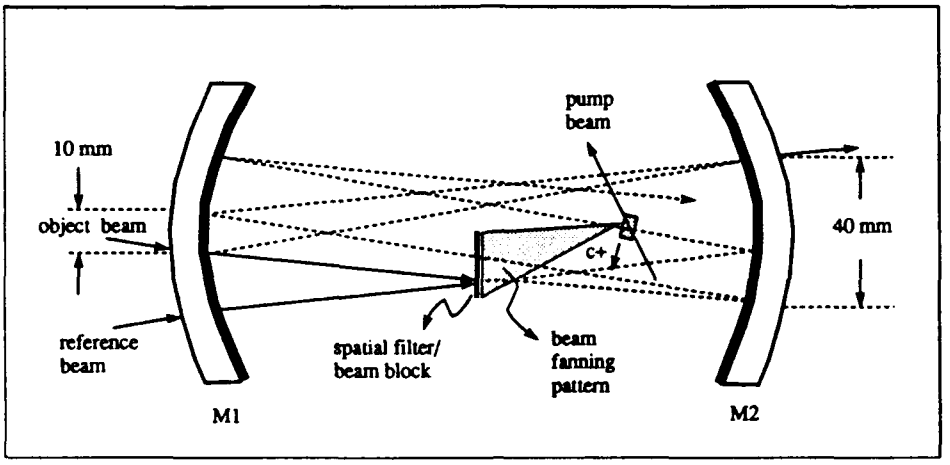

Figure 67. Block prevents object and feedback beam from freely propagating through resonator.

5.3 System Design

Although the design and test phases of the F-OAM experiment are divided into two sections in this chapter, in reality, they occurred iteratively. After the initial architecture was constructed using the infrastructure employed in the discrete architecture, initial tests showed the infrastrucure was not capable of producing the beam power required to successfully operate the system. The results of these tests were fed back into the design process which eventually led to a system design capable of producing results similar to those obtained in the discrete system.

The design presented in this section is the final result of the iterative process described above. It is divided here into three main subsections which describe its internal and external characteristics. These are: 1) the FPCR processing environment, 2) the placement of the internal components within this environment, and 3) the external infrastructure created to provide the object, reference and pump beams required for system operation. Each subsection describes a particular facet of the design, how it evolved from the results of system tests, and, when appropriate, how it implemented lessons learned from the discrete architecture experiments.

5.3.1 Fabry-Perot Confocal Resonator. A photograph of the FPCR is shown in Figure 68. The mirrors are rigidly mounted in cast iron metal frames approximately separated by the sum of their focal lengths. The position of the entrance mirror, on the left, is fixed. The position of the

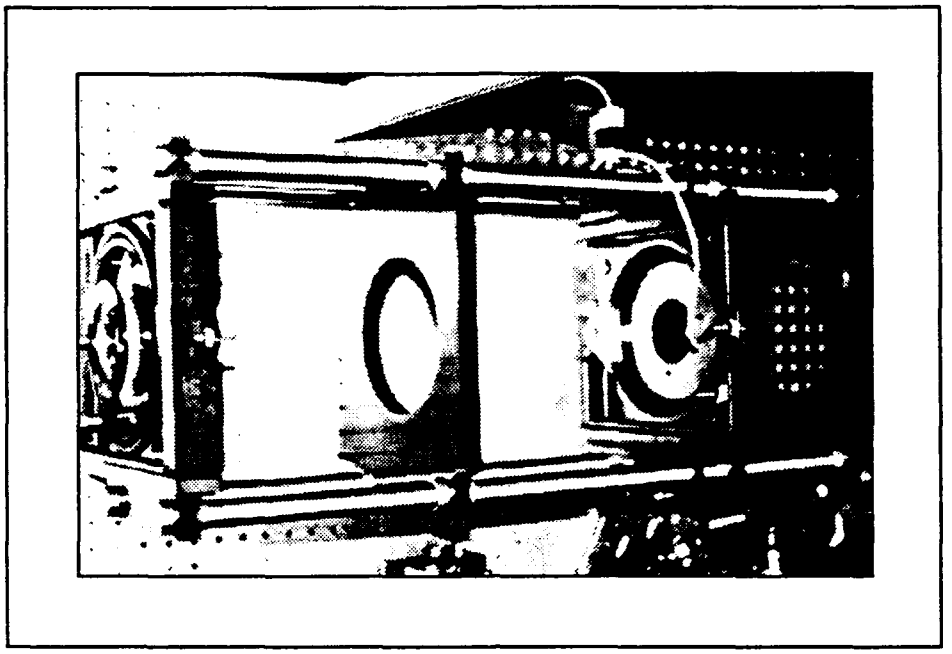

Figure 68. The Fabry-Perot Confocal Resonator.

exit mirror, on the right, can be controlled by an active stabilization feedback circuit that controls the mirror's angular and longitudinal position by monitoring the movement of interference fringes in the system output. Two aluminum plates are attached to the four stabilization rods that connect the cast iron mirror mounts. One plate is inserted between the mirrors, and the second plate is placed behind the exit mirror. The center plate slides along the stabilization rods and provides a convenient way of identifying the midplane of the resonator. It also provides a stable platform on which to mount internal processing elements.

Both Mangin mirrors used in the F-OAM architecture have an effective focal length of 35 cm and a diameter of 15 cm. Each mirror is split coated to provide 94% reflectance over one half of its surface, and 99% over the other half. This also means that a beam passing through the mirror loses either 94% of 99% of its energy in the transmission process. Therefore, in order to allow as much energy as possible to enter the system during the training and playback process, the input object beam is directed through the less reflective half of the entrance mirror. Because the system output is formed on the opposite side of the resonator's optic axis from the system input, the lower reflectivity half of the output mirror is rotated 180° from that of the input mirror.

The FPCR was aligned by following the cavity alignment procedures described by Wilson (35). One difference, however, was that the longitudinal spacing of the mirrors was set at a distance slightly less than the sum of the mirror's effective focal lengths. Recall from Chapter 2 that Fainman and Lee experimentally verified that this separation distance yields the least phase deviation over the largest output area. When the resonator was aligned, the diameter of the central dark fringe produced at the output was approximately 40 mm. This value is larger than the 36 cm central fringe diameter reported by Wilson and is believed to be the result of separating the mirrors by a distance slightly less than the sum of their focal lengths. (35:83). As recommended by Wilson, the system was shielded from air currents during the alignment process.

The FPCR's active stabilization circuitry measures the intensity in a bright fringe produced at the system output and, through a feedback loop, moves the output mirror to maintain the measured intensity at a constant value. To accomplish this, a detector with a narrow aperture is placed behind the system so that a bright fringe passes across the center of the aperture. When the mirror spacing changes, the bright fringe pattern drifts across the aperture, causing the intensity at the detector to decrease. The stabilization circuitry senses the reduction in energy and sends a bias signal to three piezo-electric crystals that control the longitudinal and angular position of the mirrors. The crystals expand and contract to reorient the mirror so that the bright fringe returns to the center of the detector aperture.

When a signal beam passes through the resonator, it is desired that phase variations across the beam remain small enough so that the system output does not contain a bright/dark fringe pattern. Of course, this also means a bright fringe pattern is not available for actively stabilizing the mirror alignment. In order to solve this problem, a second, or stabilization, beam was passed through the cavity that traveled far enough way from the optic axis to contain a bright fringe. This process is shown in Figure 69. A detector placed in the path of the output stabilization beam was then used to control the angular and longitudinal alignment of the mirrors. This process worked quite well for an empty resonator cavity. However, when the internal processing elements and supporting optical infrastructure were added to the system, it was found their was no room in the cavity in which a stabilization beam could freely propagate. Additionally, creating a stabilization beam would have consumed laser power that, as shown later, was required for system operation. Thus, the active stabilization circuitry was not used during the associative memory experiments.

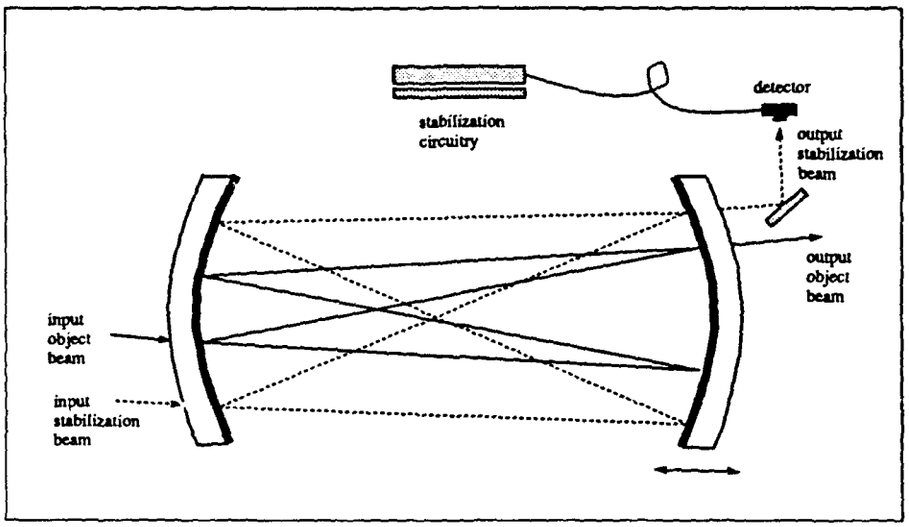

Figure 69. A second beam was transmitted through the FPCR in order to generate a high intensity fringe pattern with which to control the position of M2.

5.3.2 Positioning the F-OAM's Internal Components. The F-OAM's internal processing elements consist of the $LiNbO_3$ storage and recall elements, the $BaTiO_3$ gain and attenuation elements, and the spatial filter. These elements are inserted in the F-OAM in the same relative positions they occupied in the final design of the discrete associative memory. Thus, the process of importing the discrete design into the FPCR initially seemed rather straightforward. The $LiNbO_3$ elements would be placed in the resonator's Fourier planes, the gain crystal would be placed between M2 and the first image plane (which would also contain the spatial filter), and the attenuation element would be placed in the resonator's second image plane. However, it was found this process was complicated by the restrictive nature of the resonator's processing environment.

A diagram showing the object and reference beams as they travel through the resonator cavity is shown in Figure 70. As was the case in the discrete system, the object and reference beams combine in both Fourier planes of the resonator. Key distances and angles that define and/or constrain the beam paths are also included in the diagram. d1 is the distance below the cavity's optic axis at which the object beam reflects off M2. d2 is the distance separating the object and reference beams at M2. This distance remains constant as the beams reflect off M2 and travel to M1. d3 and d4 are the distances below the optic axis at which the object and reference

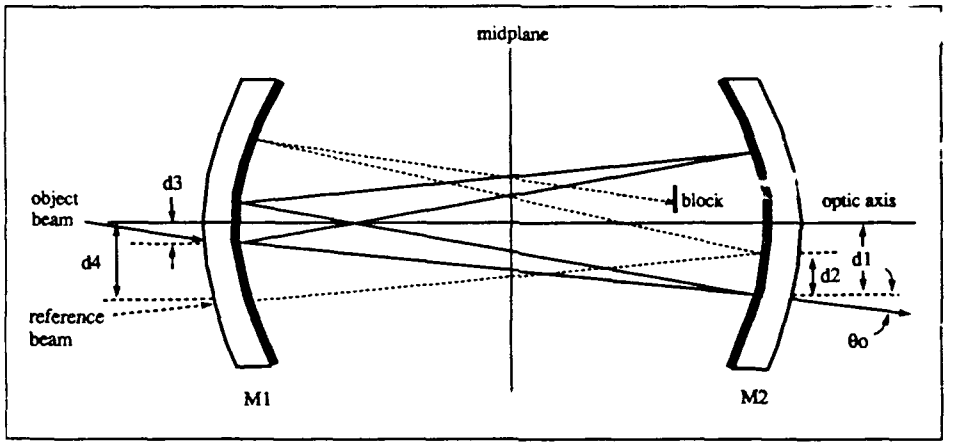

Figure 70. Object and reference beam paths inside the F-OAM.

beams enter the cavity. θo is the entrance angle of the input object beam.

The first constraint imposed by the resonator's processing environment limits the distance d1. Recall from the above discussion that when the cavity is aligned, the first interference fringe occurs at a diameter of approximately $20mm$ from the optic axis. In order to prevent fringe affects from inadvertently canceling or enhancing portions of the image in the feedback beam, the object beam must lie within this diameter. Therefore, the distance d1 must be less than $20mm$.

The physical dimensions of the $BaTiO_3$ gain crystal place a second constraint on the direction of the object and reference beams. Recall that in the discrete system, the gain crystal is placed between L2 and the first image plane of the optical feedback loop. In the FPCR, this corresponds to placing the crystal in the path of the reference beam between M2 and the first image plane. Since the reference beam travels approximately through the center of the crystal, d2 must be large enough to prevent the object beam from striking the gain crystal during the training process. Given that the width of the gain crystal is $5mm$ and the width of the object beam is $\approx 3mm$, d2 must then be at least $4mm$. These constraints led to the final gain crystal position shown in Figure 71.

The direction of the reference beam is also constrained by the geometry of the cavity. If the reference beam's angle of arrival at C1 is too large, it will pass though the crystal, reflect off M2 and exit the cavity before it reaches M1. This occurs when the reference beam's angle of arrival at

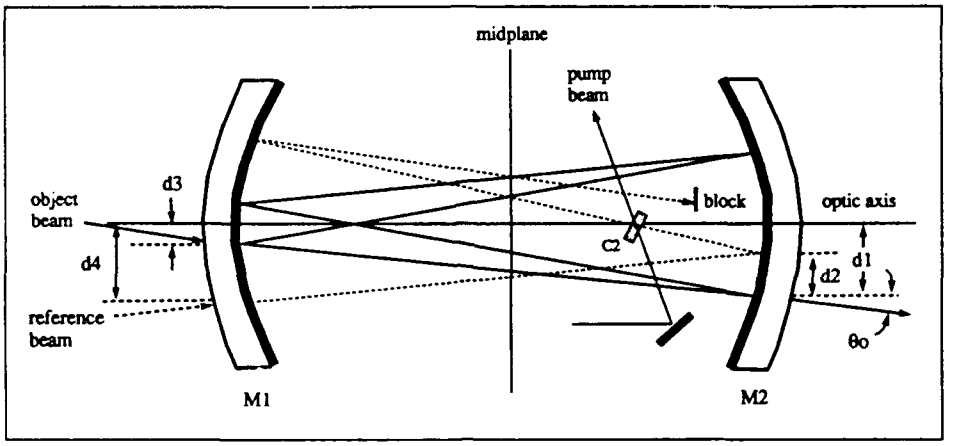

Figure 71. Position of the gain element in the F-OAM.

C1 is greater than the arctangent of the ratio of the mirror radius and cavity spacing, or, as Wilson notes, approximately 3° (35:85). Thus, in order to ensure the input reference beam angle at C1 remains smaller than 3°, the reference beam is introduced to the cavity through the input mirror.

A third constraint on the internal beam paths is imposed by the dimensions and location of the attenuation element. In the discrete architecture, the attenuation element was placed in the second image plane of the resonator. However, the $20mm$ constraint placed on d1 does not leave enough separation distance between the $LiNbO_3$ crystals to insert the attenuation crystal in the midplane of the resonator and still allow the object, reference and feedback beams to freely propagate though the midplane of the resonator. Thus the attenuation crystal must be moved along the feedback beam path either towards M1 or M2. The crystal was not moved towards M2 because the gain crystal already occupied this half of the resonator, thus limiting the amount of room available to insert the optical elements required to direct the pump beam onto the crystal. Therefore, the attenuation element was positioned in the opposite side of the cavity between the second image plane and M1 as shown in Figure 72. The symmetric feedback properties of the resonator are such that the point at which the arm of the object beam traveling between M2 and M1 strikes M1 is equidistant above the optic axis from the point at which the object beam entered the resonator below the optic axis. Thus, if d3 is too small, the attenuation crystal will interfere with the arm of the object beam that travels between M2 and M1. Since the attenuation element is $5.5mm$ wide, d3 and the location of the attenuation element must be chosen to allow a separation

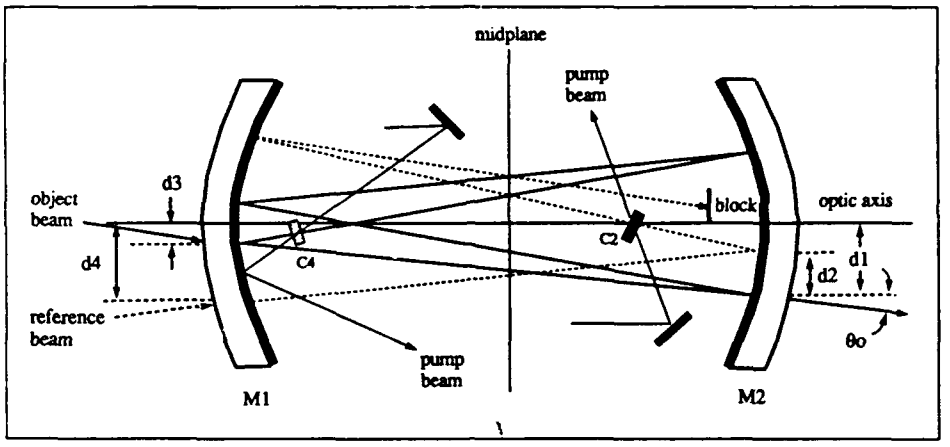

Figure 72. Position of attenuation element in the F-OAM.

distance of at least $2.75mm$ between the center of the feedback beam and the outer edges of the input beam before and after it reflects off M1.

Another consideration, rather than a constraint, when choosing beam trajectories and crystal locations inside the resonator concerns the angle of arrival of the pump beams at the gain and attenuation elements. As shown in preliminary crystal experiments, smaller input beam separation angles improve the gain and attenuation characteristics of the crystal. Therefore, the crystal positions and beam paths should be chosen to reduce the input signal and pump beam separation angles as much as possible.

The final processing element inserted in the resonator was the spatial filter pinhole apparatus shown in Figure 73a). A $0.71mm$ pinhole was drilled into a rectangular aluminum plate that was narrow enough ($\approx 5mm$) to fit between the reference beam arriving at C3 and the object beam leaving C3 and traveling through the midplane of the resonator on its way to M1. The pinhole was attached to an optical post which in turn connected to a micrometer controlled translational stage and sliding mount constructed on top of the aluminum plate located in the midplane of the resonator. A photograph of the pinhole mount is shown in Figure 73b). The sliding mount controls the horizontal position of the pinhole and the translational stage controls its vertical position.

As mentioned earlier, the $5mm$ width of the pinhole plate is significantly smaller than the $1.5cm$ width of the beam fanning noise pattern produced by the gain crystal. However, because the

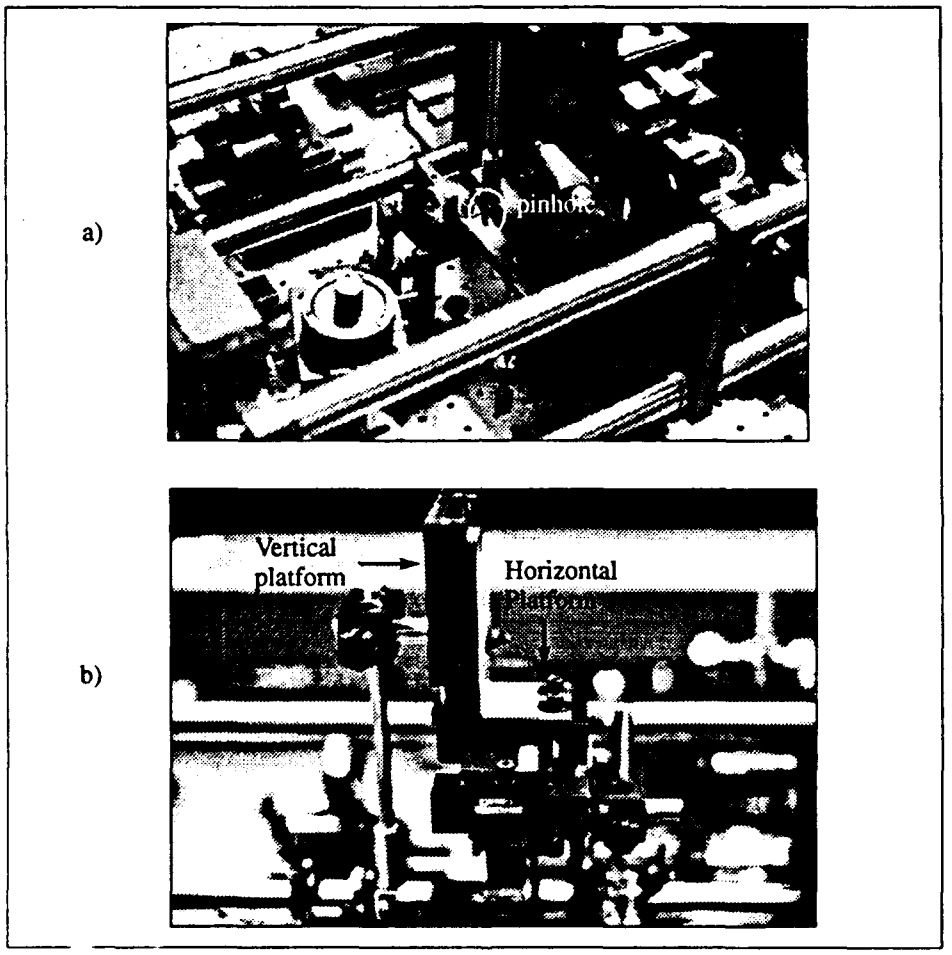

Figure 73. a) Pinhole placed in resonator's image plane. b) Mounting apparatus used to control horizontal and vertical postion of pinhole.

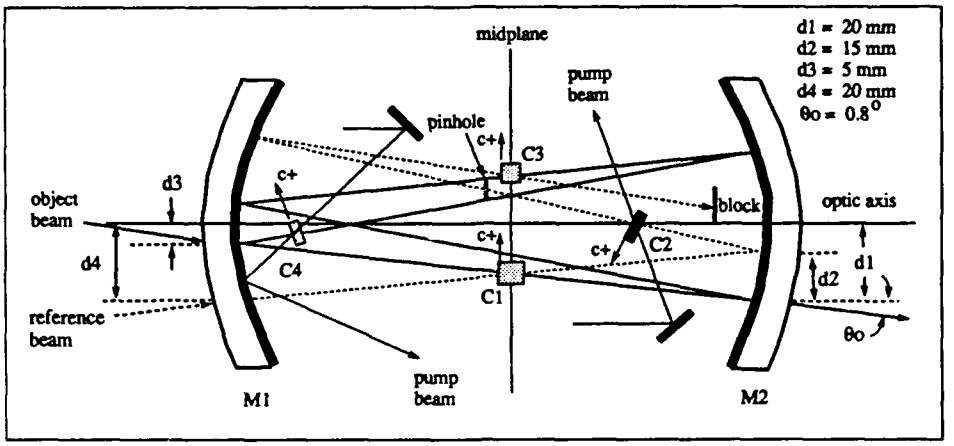

Figure 74. Final locations of the F-OAM's internal processing elements.

gain crystal is placed halfway between M2 and the midplane of the resonator, the noise collected by M1 is not focused on the second $LiNbO_3$ crystal. Although the beam fanning noise presented more of a problem than in the discrete cavity, where it was completely blocked by the spatial filter, the experimental results discussed in the last section of this chapter show it did not prevent the system from constructing a clearly discernable output.

A diagram and accompanying photograph of the final locations of the internal processing elements in the FPCR are shown in Figure 74. C1 and C3 were placed $10mm$ above and below the resonator's optic axis respectively. The input beam entered the cavity $5mm$ below the optic axis, passed through C1 and reflected off M1 $20mm$ below the optic axis. The reference beam behaved in the opposite manner. It entered the cavity $20mm$ below the optic axis, passed though C1 and reflected off M1 approximately $5mm$ below the optic axis. This yielded an input object/reference beam separation angle of 1.6^o. The separation distance between the object and reference beams as they reflected off M1 and traveled to M2 was approximately in the feedback beam path between the second image plane and M1 at a location where it did not interfere with the object beam.

The photograph also shows that the $LiNbO_3$ crystals are placed on a thick aluminum plate that stretches across the midplane of the resonator. The plate absorbs vibrations and allows room to position C3 to compensate for beam path deviations caused by C1 and C2. Both $BaTiO_3$ crystals are mounted on cylindrical steel rods placed on top of rotating turntables. The rods place

the crystals high enough above the turntables to allow non-paraxial beams to pass though the resonator without striking the turntables. As before, the turntables allow precise control over the direction of the crystal's optic axes.

5.3.3 Compensating for Internal Beam Path Deviations. In the discrete architecture, the refractive and geometric properties of the four photorefractive crystals altered the point at which the object and reference beams intersected in the second Fourier plane of the feedback loop, and the position and direction of feedback beam when it rejoined the input. The deviation in the beam's intersection point in the second Fourier plane was compensated for by repositioning the second $LiNbO_3$ crystal, C3, slightly behind the second Fourier plane. Deviations in the position and direction of the feedback beam were compensated for by iteratively adjusting the tilt of the loop's mirrors and beamsplitter and the position of the attenuation element until the feedback and input beams again overlapped at the beamsplitter. Because the position and orientation of the crystals in the F-OAM are nearly identical to those used in the discrete architecture, these same problems exist and must be compensated for before attempting to train and operate the system.

Like the discrete architecture, translational and angular path deviations incurred at C1 and C2 also moved the second object and reference intersection point slightly behind the second Fourier plane of the FPCR. However, in anticipation of this problem, the thick aluminum plate used to support C3 was made wide enough to move the crystal to the new intersection point located approximately 1 cm behind the original intersection point. As discussed earlier in the chapter, because the FPCR's mirrors cannot be adjusted to alter the position and direction of the feedback beam, the second problem was corrected by designing and fabricating a beam path compensation device that was inserted in the F-OAM immediately behind C3.

An *in situ* photograph of the compensator in the FPCR is shown in Figure 75. It consists of a 1.5 cm X diameter rubber O-ring sandwiched between two $2x\,2x\,.25cm$ near-optically flat glass plates. The O-ring is filled with index matching fluid that matches the refractive index of the glass. The back plate is attached to an aluminum rod for mounting purposes. The face plate is attached to the back plate with four set screws that allow one to control its tilt around the horizontal and vertical axes.

The compensator is filled with index matching fluid by laying the back plate flat and placing

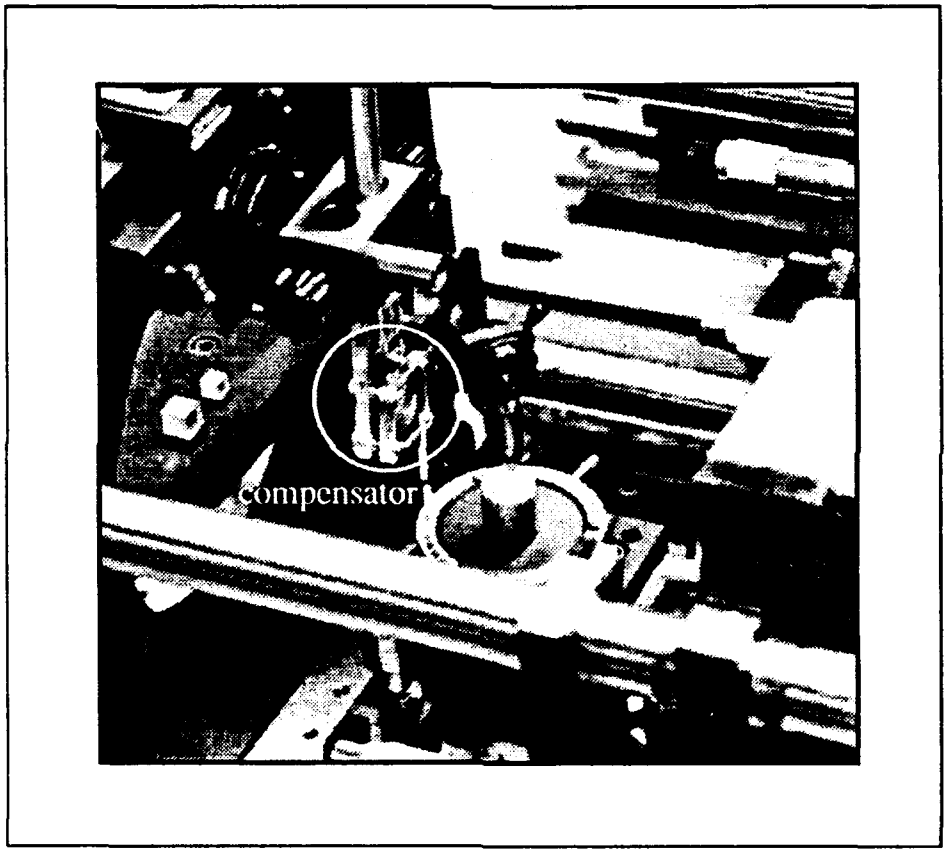

Figure 75. Wedge compensator in position in the FPCR.

the O-ring squarely in the center of the plate. The O-ring is then filled with index matching fluid using a capillary tube. The fluid is added drop by drop until a meniscus is formed across the surface of the O-ring. The face plate is carefully layed on top of the O-ring to prevent the creation of air bubbles in the index matching fluid. The set screws are then inserted down through the face plate and into four hex-nuts epoxied onto the bottom surface of the back plate. Although the idea for the compensator is shared jointly by the author and Mr G. Vogel, Mr Vogel is solely responsible for its design. The compensator was fabricated by personnel at the AFIT Fabrication Shop.

The compensator was mounted on a Newport variable pitch platform attached to the large aluminum plate spanning the midplane of the resonator. As shown in Figure 75, the compensator was placed in the path of the reconstructed object beam shortly after leaving C3. The platform rotates the back plate about its horizontal and vertical axes, which, combined with set screw adjustments that rotate the face plate about its horizontal and vertical axes, provides the four degrees of freedom required to correct for translational and angular deviations in the feedback beam path.

Figure 76 show the effects of beam path deviations on the F-OAM output and how the compensator corrects these effects. The first picture shows the system output when a diamond pattern passes through C1, C2 and C3 before recombining with the input. The compensator is not present in the system. The translation and angular beam path deviations introduced by the crystals causes the feedback beam to walk out of the FPCR. The light and dark regions in the output are interference fringes. The second photograph shows the fringe pattern that results when translational deviations are corrected by the compensator, and the last photograph shows the system output when translational and angular adjustments in the feedback beam path are both fully compensated.

It must be emphasized here that only C1, C2 and C3 were present in the resonator when these photographs were taken. The compensator was not able to correct for path deviations introduced when the attenuation element, C4, was added to the system. Therefore, the attenuation element was not used in the F-OAM discriminate between multiple objects traveling superimposed in the feedback beam, removing it from the architecture did not present a problem for single memory recalled using some type of modified F-OAM architecture (remember, the current architecture will not support more than one memory), either the "strength" of the compensator will have to be

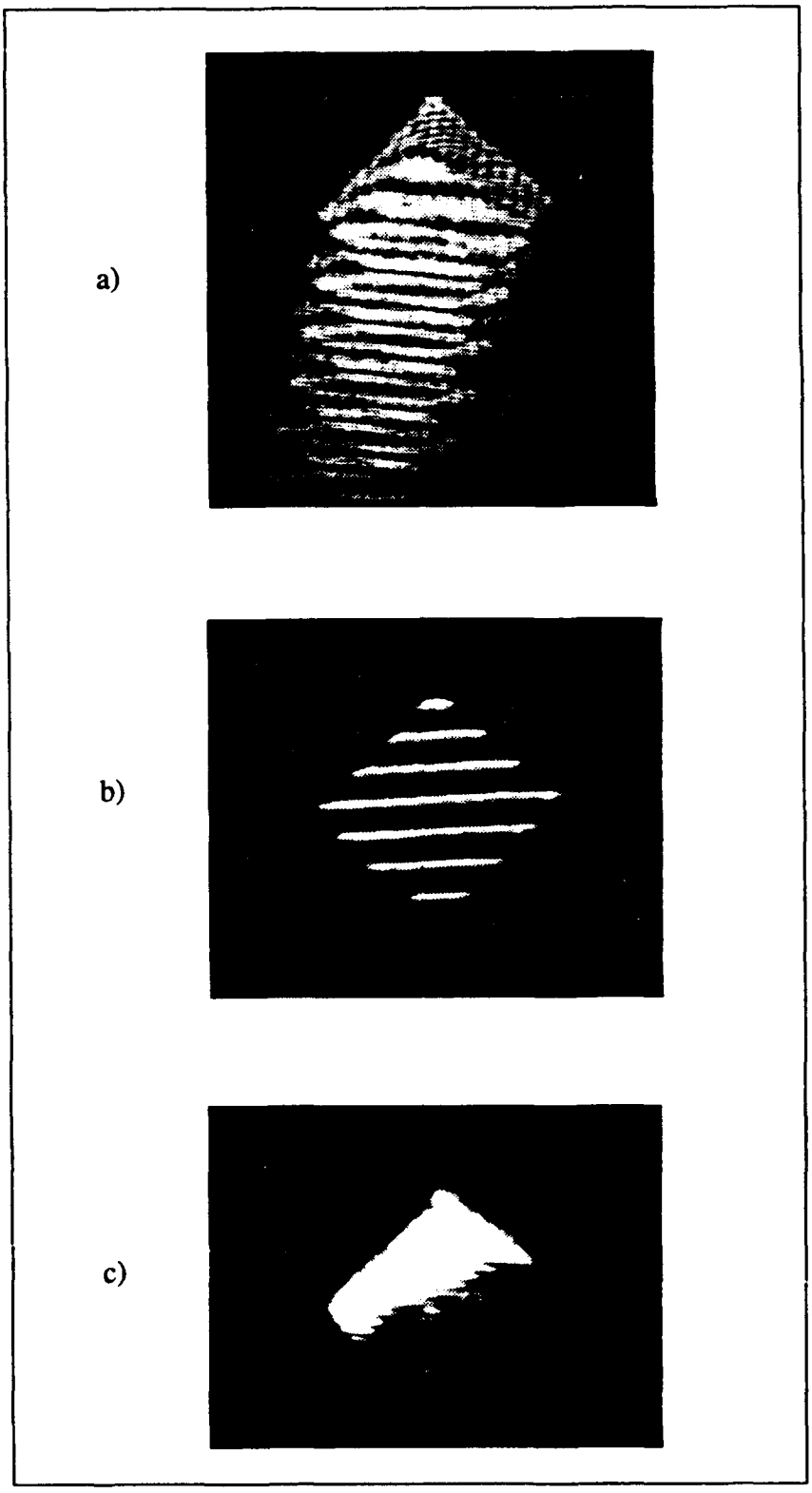

Figure 76. Various stages of feedback beam compensation in the F- OAM.

increased, or a different compensation technique will have to be found. One possible alternative is to immerse each of the four crystals in a separate liquid crystal gate with a surface geometry that can be varied to correct for the non-parallel nature of the crystal faces.

5.3.4 External Optical Infrastructure. As in the discrete architecture, the primary purpose of the optical infrastructure surrounding the FPCR is to provide object, reference and pump beams at the appropriate sizes and intensities required to train and operate the F-OAM. Since the infrastructure used in the discrete system already achieved these goals, initial attempts were made to simply replace the discrete optical feedback loop with the FPCR and, with some minor modifications, use the existing infrastructure to support the F-OAM. Initial experiments with this approach showed that it failed for three main reasons.

The first, and most debilitating, problem with using the existing optical infrastructure was that, even at maximum laser power it was not able to deliver more than $300\mu W$ of power at C1. Based on results from the discrete architecture experiments, this is not enough power to generate refractive gratings in the $LiNbO_3$ crystals for the higher spatial frequency components required to produce a quality output.

The second major problem with the existing discrete infrastructure was that it controlled the size of the phase encoded Fourier transform using an adjustable iris placed approximately $10cm$ in front of C1. The restrictive nature of the F-OAM's internal processing environment precluded placing the iris this close to C1 in the FPCR. Additionally, when the iris was placed in the input beam path just outside the resonator ($\approx 45cm$ from C1) vignette effects were present in the output object.

The final problem with the existing infrastructure was that a distinct Fresnel ring pattern was evident in the reference beam at C1. The rings were caused by the input and output apertures of the spatial filter/beam expander. They were eliminated (or hidden) in the discrete architecture by closing down the spatial filter's input aperture size until the bright rings caused by the spatial filter's input aperture overlapped the dark regions in the rings caused by the beam expander's output aperture. Because the F-OAM required as much power as possible, the input aperture had to be opened and the rings reappeared. When a Fourier transform hologram is stored in a photorefractive crystal using a ringed reference beam, the spatial frequencies that lie inside the

dark regions of the ring pattern are not recorded.

In order to correct the above problems, the supporting infrastructure was completely redesigned. Figure 77 contains a photograph and accompanying diagram of the final design and is repeatedly referred to throughout the remainder of the chapter. The following sections briefly describe the major elements in the infrastructure design.

5.3.4.1 Input Object Beam. In the discrete architecture, the laser output was immediately separated into two beams as it left the laser. One beam, containing approximately half the output laser power was used to create both two wave coupling pump beams, while the remaining laser power was divided equally between the input object and reference beams. In order to gain more power in the input object beam, the beamsplitters BS1 and BS2 in the discrete architecture were replaced with plane mirrors M1 and M2 and the reference and pump beams were created by extracting approximately 10% of the output laser power using the Fresnel beam sampler BS-F. This ensured roughly 90% of the laser output power was directed into the object beam, yielding about 3.5 times as much object beam power as the discrete infrastructure. However, the object beam losses at the FPCR mirror were roughly 8.3 times larger than the losses at the 50/50 beamsplitter used as an input element in the discrete feedback loop. Thus, even with the input laser producing nearly 3 W of power, the F-OAM was only able to deliver a $1mW$ object beam at C1.

The lens combination L1 and L2 (f = 20 and 10 cm respectively) were used to reduce the input beam diameter to approximately the same size as the diameter of the input object transparency . The diameter of the phase encoded Fourier transform was controlled by placing an adjustable iris (i.e, an aperture stop) in an external Fourier plane created by the 15 cm focal length lenses L3 and L4. This architecture eliminates the vignetting effects discussed earlier.

The last elements in the input object beam arm are the 50 cm focal length lens L5 and the plane mirror M5. L5 Fourier transforms the phase encoded object formed in the back focal plane of L4 and M5 directs it onto the first Fourier plane of the FPCR. Because the input mirror produces a slight negative lens effect, L5 is positioned so that the input object beam is slightly converging when it reaches the input mirror (35:76). As shown in the photograph in Figure 78, M5 is mounted on a slide rail in order to control the angle at which the object beam enters the

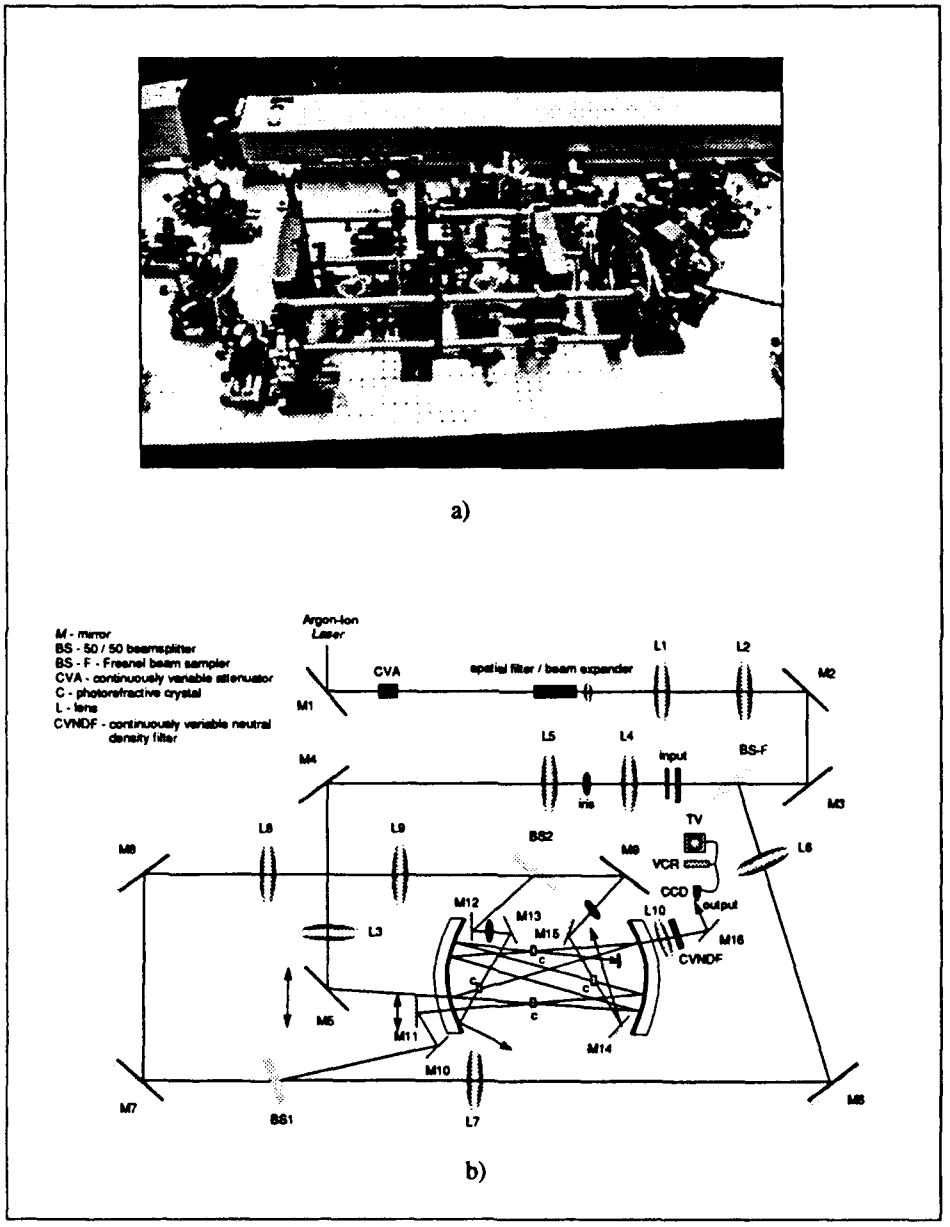

Figure 77. Final design of the F-OAM optical infrastructure.

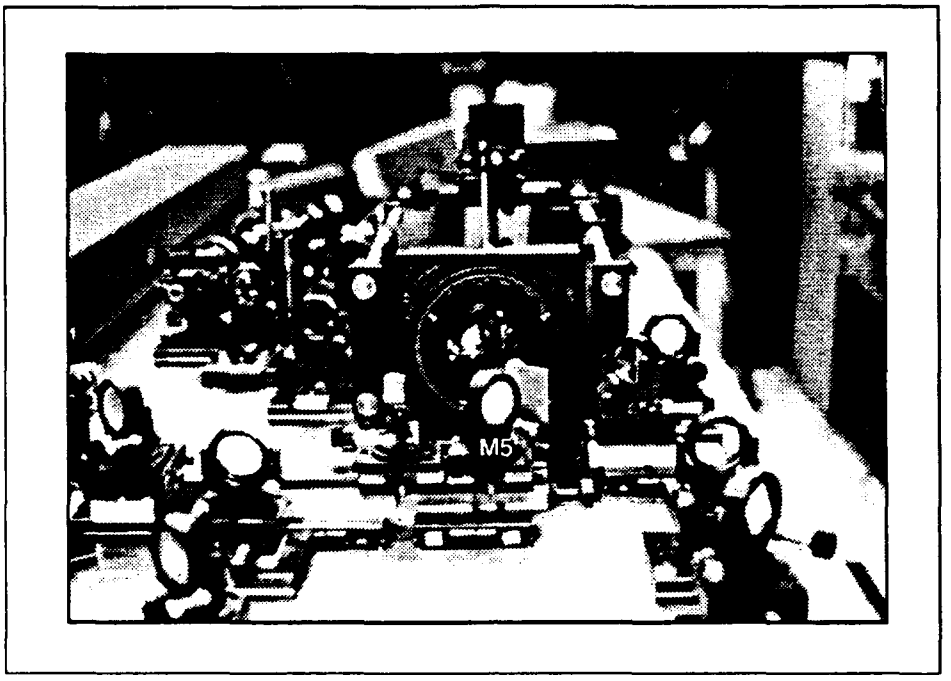

Figure 78. Sliding input mirror used to control the input object beam location and angle.

cavity. The wood blocks placed beneath the lens mounts are used to raise the beam height to the centerline of the FPCR.

5.3.4.2 Reference Beam. The reference beam was created from the input laser beam reflection off the 90/10 Fresnel beam sampler BS-F. As the reflected beam leaves the beam sampler, the intensity distribution across its face is uniform. However, when it arrives at C1, a Fresnel ring pattern is clearly visible across the face of the beam. Lenses L6 (f = 100 cm) and L7 (f = 75 cm) eliminate the ring pattern by imaging the uniform beam distribution present at the beam sampler onto C1. BS1 is moved along the reference beam path in order to control the location of the image. Mirrors M10 and M11 are steering mirrors that control the angle at which the reference beam enters the cavity. M11 is shown in more detail in the photograph contained in Figure 79. The mirror is mounted on the corner of an aluminum plate in order to place it as close to the input object beam as possible. M11 is also mounted on a micrometer controlled translational stage to precisely control the input location of the beam. In addition to removing the Fresnel rings from the reference beam, L6 and L7 also reduce the reference beam diameter to the $6mm$ size used in

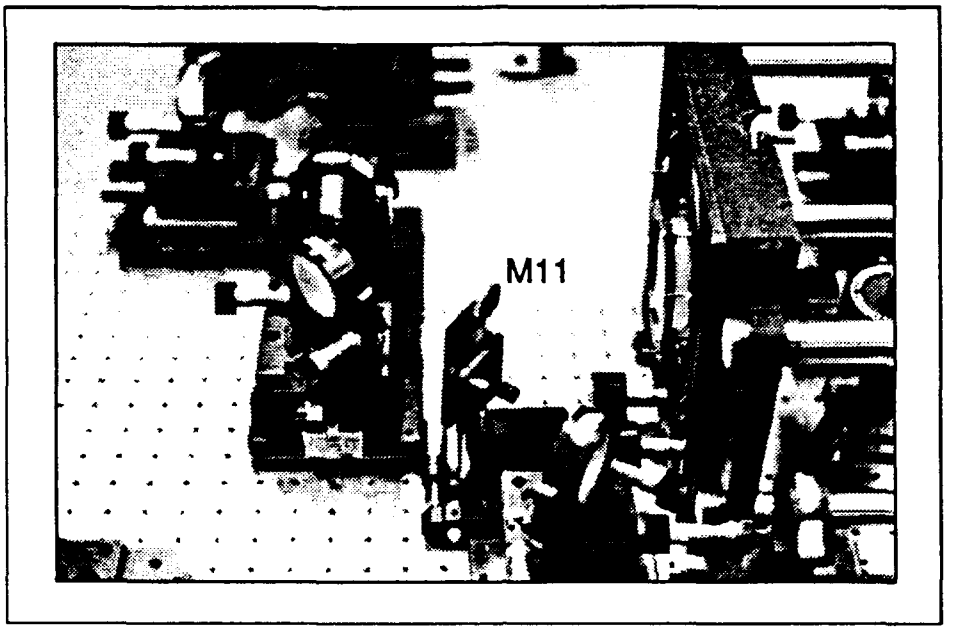

Figure 79. Sliding input mirror used to control the input reference beam location and angle.

the holographic recording process. Thus, an iris is no longer required to control the size of the reference beam. At full laser power, the reference beam power measured at C1 was approximately $8mW$, yielding an input reference to object beam intensity ratio of 8 to 1, and a combined input beam power of $9mW$.

5.3.4.3 Pump Beams. Both pump beams are created by the beam transmitted by the beamsplitter BS1. At full laser power, the power in the beam just past BS1 was measured at $170mW$. M7 and M8 directed the pump beam to the opposite side of the FPCR where two lenses, L8 (f = 30 cm) and L9 (f = 15 cm) reduced the beam size and increase its intensity. BS2 is used to create the pump beam for the attenuation element placed in the entrance cavity of the FPCR, and M9 directs the gain crystal pump beam into the FPCR's exit cavity. A diagram and photograph showing the internal optical elements used to control the size and direction of the pump beams when they enter the resonator are contained in Figure 80. Each of the optical elements in the cavity are 1 inch in diameter and mounted in miniature Newport mounts.

Plane mirrors M12 and M13 are used as steering mirrors to control the elevation and angle

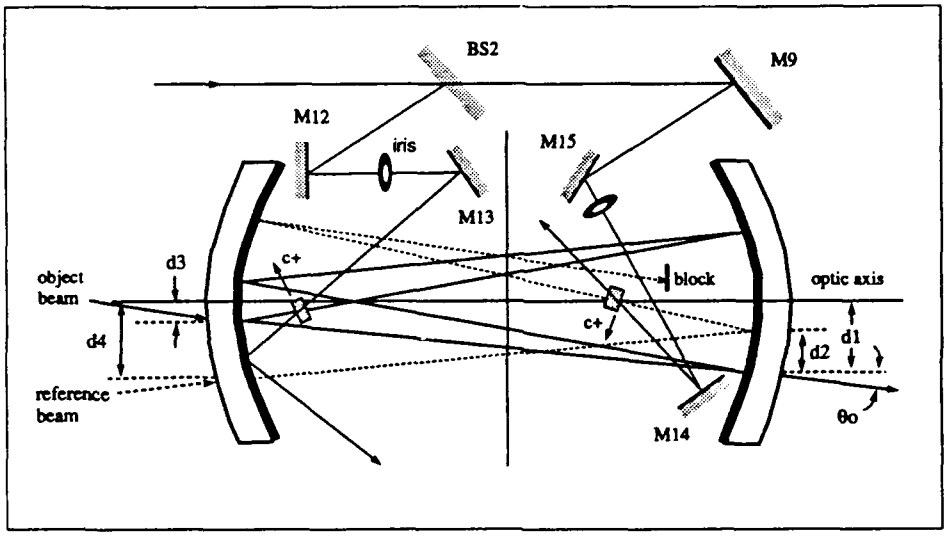

Figure 80. Internal elements used to control pump beams.

of arrival of the pump beam at the attenuation element C4. An adjustable iris is placed just past M12 to control the size of the beam. Recall from the earlier discussions concerning the internal path of the object beam that the beam's input location (d3) was chosen so that the attenuation element placed in the feedback beam did not interfere with the input object beam before and after it reflected off the cavity mirror M1. Another consideration only mentioned at the time involves the location of the steering mirrors. Figure 80 shows that by reducing d3, the separation angle between the feedback and pump beams is also reduced, and, therefore, the gain coefficient of the crystal is increased. Thus, d3 was chosen so that the object beam traveling between M1 and M2 barely missed the side of the attenuation element. The resulting internal input beam separation angle was approximately 8.5°.

A similar approach was used to determine the final location of the gain crystal (i.e., the distance d1). By reducing the input reference beam angle so that the distance d1 is slightly larger than the half-widths of the gain crystal and object beam, the separation angle between the pump beam reflecting off the steering mirror M11 and the reference beam is reduced and the gain coefficient is in turn increased. Therefore, the reference beam angle and the location of C2 were chosen so that the object beam reflected off the cavity mirror M1 while barely missing the side of the gain crystal. This yielded an internal input beam separation angle at the gain crystal of 6°.

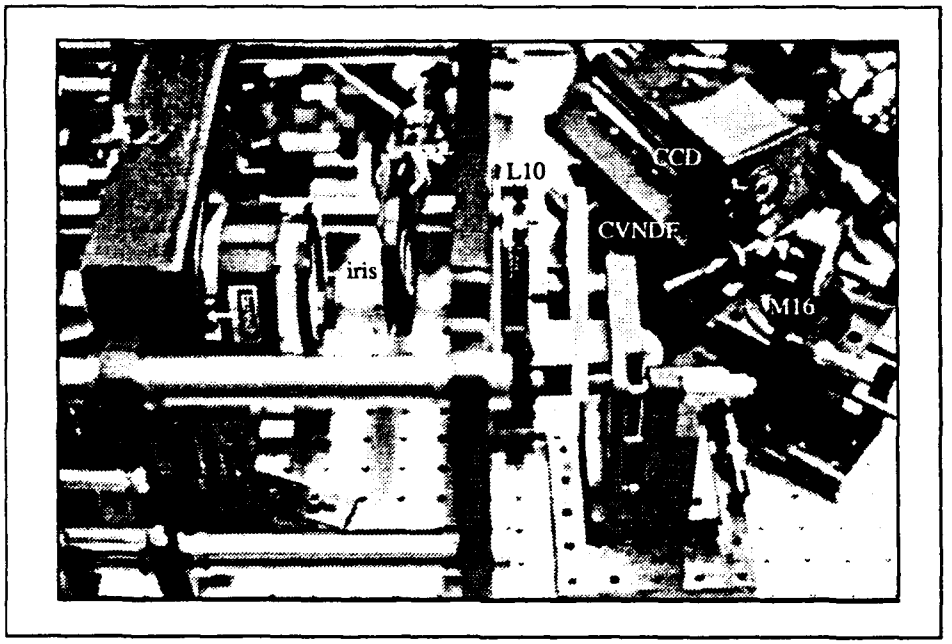

Figure 81. Internal elements used to control pump beams.

5.3.4.4 System Output. A photograph showing the optical elements used to form and capture the system output is provided in Figure 81. The circular object located just behind the mirror is a large, adjustable iris. The aperture of the iris is reduced to approximately the same size as the output object, while the remaining portion of the iris blocks optical noise collected by the output mirror. After passing through the iris aperture, the output signal is Fourier transformed by a 30 cm focal length lens placed immediately after the rear mounting plate of the FPCR. A variable neutral density filter controls the intensity of the output before it reflects off M14 and into the Sony CCD camera. The CCD is placed a focal length away from the output Fourier transforming lens and is covered by a protective shield and adjustable iris to reduce background noise scattered off surrounding external components. The lens is removed from the CCD camera in order to focus the Fourier transformed output beam directly onto the CCD array. As in the discrete system, the camera output is connected to a Panasonic S-VHS video recorder and a Zenith monochrome television monitor.

5.4 *System Operation*

This section first presents the parameters and methodology used to train the F-OAM to recognize a single object. The system's operation is then examined by following the object beam as it travels from the input object transparency through each of the system's internal components and recombines with the input at the cavity entrance mirror M1. Results showing the system is capable of recalling a complete object when presented with partial information about the object are also described. These results were obtained at the conclusion of an iterative design and test process in which results from a series of operational experiments were used to modify the F-OAM design to enhance system performance. Pertinent changes made in the system design as a result of the iterative process are discussed at the appropriate stage of the system operation. Because the operation of the discrete and F- OAM architectures was so similar, many of the details of the system operation are not repeated in this chapter.

5.4.1 Training. The location and orientation of the internal processing elements in the F-OAM and discrete architectures were nearly identical. Consequently, the same methodology and procedures used to train the discrete system were also used to train the F-OAM. The details of the training process were presented in Chapter 4, therefore only a general summary of the approach is described here.

The initial crystal locations were chosen based on the design constraints described earlier in the chapter. The position of each crystal was marked at it respective location in the FPCR and the crystals were removed from the resonator. The object and reference beams were first individually, then simultaneously, transmitted through the FPCR in order to establish their correct input locations at M1 and angles of arrival at C1. Crystals C1 and C2 were then placed at their respective locations in the resonator and oriented to provide maximum diffraction efficiency and two wave coupling gain. C3 was inserted at the location required to compensate for beam path deviations introduced by C1 and C2. A low intensity object beam was passed through the system and the compensator was adjusted to ensure the input and feedback beams overlapped at M1. The attenuation element was not inserted in the system because the compensator was not able to fully compensate for its non-parallel geometry. The final crystal locations and beam path parameters used in the training process were previously described in the system design section of this chapter.

The system was initially trained by blocking the feedback beam between C3 and M2, shielding the system from air currents using a plexiglass cage, and allowing the object and reference beams to illuminate C1 and C3 for two minutes. At this point, the optical infrastructure used to support the discrete architecture was still being used to provide the object and reference beams for the F- OAM. Thus, the object beam power at C1 (before Fresnel reflections at the crystal face) was only $0.2mW$ and the reference beam power was $1.2mW$. Both beam diameters were $6mm$. Although the input reference to object beam intensity ratio of 6 to 1 meets the criteria established by Frye for maximum diffraction efficiency, the total power of $1.4mW$ falls far short of the $35mW$ figure recommended by Frye.

Thus, when the object beam was presented to the system at the same power used in the recording process, it failed to reconstruct a reference beam at C1. The experiment was repeated for recording times of 3, 5 and 7 minutes, yielding the same results. Finally, a card was placed behind C1 in the path of the reference beam to monitor the length of time required to reconstruct a noticeable reference. The hologram was recorded at the above input powers and the reference beam was briefly blocked at 1 minute intervals. The central portion of the reference beam was faintly visible on the card after a recording time of approximately 12 minutes. Given the previously discussed problems associated with exceeding a recording time of three minutes, it was decided to redesign the optical infrastructure to increase the system power.

Before arriving at the final infrastructure discussed earlier, an intermediate design was implemented that doubled the object and reference beam powers to 0.4 and $2.4mW$ respectively. However, for a recording time of 3 minutes, the system was only able to reconstruct the central portion of the reference beam at C1, which in turn generated a "blob" of light, rather than a tank, at the output. In order to confirm the system's poor performance was the result of power problems, the tank transparency was replaced with a square pattern that yielded an object beam power of approximately $1mW$ (or, roughly three times the beam power produced by the tank pattern). The system was then trained to recognize the square pattern using a $6mW$ reference beam and a recording time of 3 minutes. When presented with an incomplete version of the square pattern, the system was able to clearly reproduce the complete pattern. Having confirmed that the system suffered from a lack of power, the infrastructure was again redesigned until it matched the final architecture discussed above. Using the tank transparency as an input object, this design

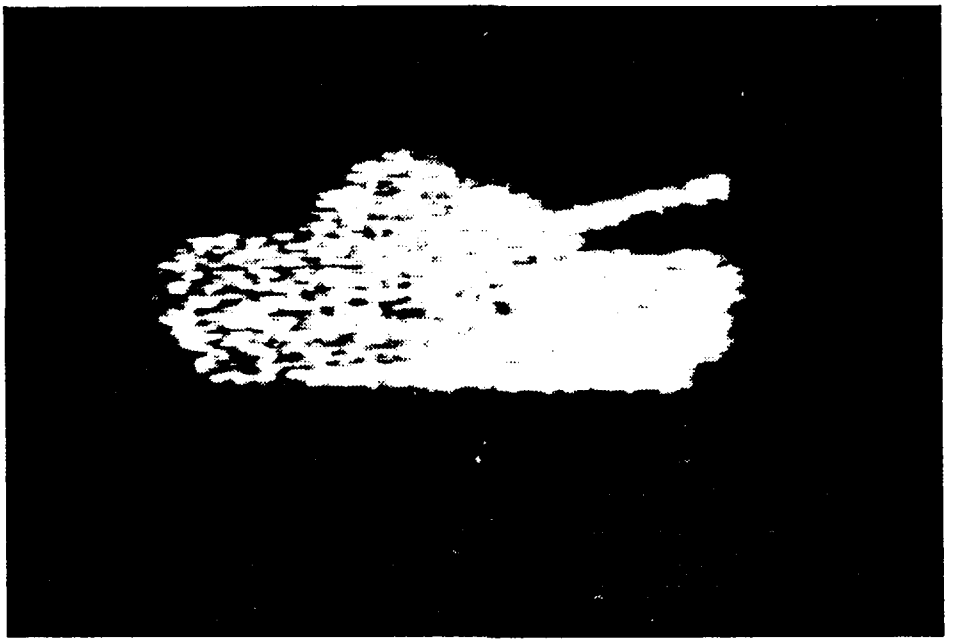

Figure 82. Object stored in memory.

yielded a $1mW$ object beam and an $8mW$ reference beam for an input laser power of 3 W. The tank was recorded in the volume holograms for 3 minutes and the system was illuminated with an incomplete version of the tank. The following sections discuss the operation of each phase of the system.

5.4.2 Stage 1 - Object transparency to C1. The object transparency consisted of a tank etched onto an opaque plate glass slide. The 120 second acid etched phase encoder was placed immediately behind the transparency. The input object was created by illuminating the tank transparency with a collimated plane wave. A digitized photograph of the object pattern stored in the system is shown in Figure 82. As before, the speckle pattern is produced by the phase encoder.

After storing the object in the system memory, an incomplete version of the object was presented to the system. The incomplete object was formed by blocking a portion of the input beam immediately in front of the object transparency. A digitized photograph of the incomplete object is shown in Figure 83.

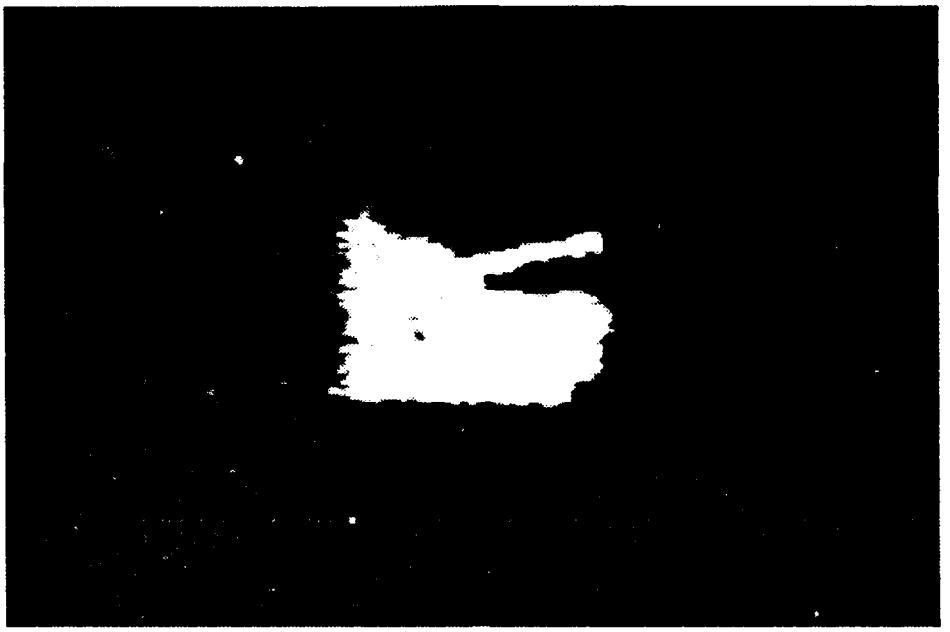

Figure 83. Incomplete object presented to system.

When the phase encoded version of the partially blocked object left the input plane, it traveled to the external Fourier plane formed by the 15 cm focal length lenses L3 and L4. The size of the phase encoded Fourier transform was controlled by an adjustable iris placed a focal length behind L3. The iris aperture was set to provide a $6mm$ diameter Fourier transform at C1. The object beam then traveled through the 50 cm focal length lens, L5, which produced the object's phase encoded Fourier transform C1. The beam steering mirrors M4 and M5 were used to control the input location, angle and plane of the object beam. In these experiments, the input location at M1 was $5mm$ off the optic axis, the input object angle was $\approx 0.8^{o}$ and the object traveled in a horizontal plane taken through the center of the cavity mirrors.

5.4.3 Stage 2 - C1 to C2. When the incomplete object illuminated C1, a plane wave with an intensity profile identical to the central portion of the stored object traveled in the direction of the reference beam and a "DC" term traveled in the direction of the object beam. The DC term was blocked before it reached M2, while the reconstructed reference beam was allowed to reflect off M2 and travel to the gain crystal. No attempt was made to measure the power in the reconstructed beams because the restrictive nature of the processing environment made it extremely difficult to

insert a power detector without disturbing the position of the internal components.

The gain crystal was rotated to provide an internal grating vector angle of $\approx 10^o$. The internal reference beam/pump beam separation angle was 6^o. Because the attenuation element was not present in the resonator, BS2 was removed from the system. Thus, the entire power contained in the beam transmitted by the beamsplitter BS1 was used to form the gain crystal's pump beam. The resulting pump beam power was $\approx 150mW$ at a beam diameter of $3mm$. Assuming the diffraction efficiency at C1 was approximately 10% (not unreasonable considering the relatively small intensities of the beams used in the recording process), the input pump beam to signal beam intensity ratio at C2 was greater than 2000. After exiting the gain crystal, the pump beam propagated out the side of the resonator, while the amplified reference beam and beam fanning noise pattern traveled toward the spatial filter.

5.4.4 Stage 3 - Spatial Filter to C3. The plate in which the pinhole spatial filter was drilled was approximately $5mm$ wide. It was painted flat black to reduce internal reflections in the cavity. The plate was narrow enough to leave in the system during the training and operation process. This alleviated the need to insert the spatial filter after training the system (and risk disturbing the internal elements) as was the case in the discrete architecture. The trade-off, however, was that the narrow plate was not large enough to block all the beam fanning noise pattern generated by C2. When the amplified reference beam and beam fanning noise reached the pinhole, about one third of the noise was blocked by the plate. The remaining portion of the noise pattern, as well as the filtered reference beam then reflected off M1 and traveled to C3.

5.4.5 Stage 4 - C3 to M1. If the gain crystal had been placed in the resonator midplane as originally suggested by Wilson, the beam fanning noise generated by the crystal would have been focused by M1 onto crystal C3, and, as discussed earlier, may have washed out the holographic gratings formed during the training process. However, by placing the gain crystal halfway between M1 and the resonator's midplane, the beam fanning noise was spread out in space when it reached C3. Although beam fanning noise was still present in the system output, it appeared to have little effect on the integrity of the holographic gratings formed in the $LiNbO_3$ crystal.

When the reconstructed reference beam illuminated C3, an object beam was generated that

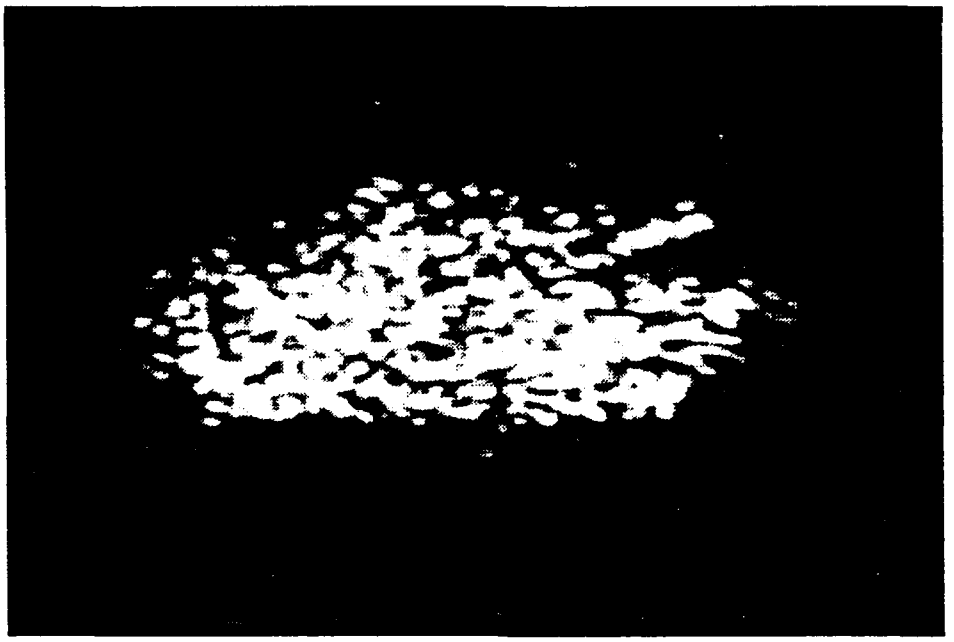

Figure 84. Reconstructed output.

traveled in the same direction as the object beam used in the training process. The remainder of the reference beam that exited C3 was blocked before it reached M2. The reconstructed object beam passed through the plate glass compensator and traveled to M2 where approximately 6% of its energy was transmitted through the mirror. The remaining energy in the object beam reflected off M2 and traveled to M1 where it rejoined the input.

The object beam transmitted by M2 passed through an iris used to block beam fanning noise collected by the mirror. The beam then traveled to an external 30 cm focal length lens, L10, that transformed the phase encoded Fourier transform reconstructed at C3 into an image of the stored object at a CCD array located in the back focal plane of the lens. A digitized photograph of the reconstructed object is shown in Figure 84.

Although the F-OAM output is clearly discernable, a comparison between the F-OAM and discrete system outputs shows the discrete system was able to reconstruct a brighter, more clearly defined object. Because the internal structure of both systems are nearly identical, the difference is most likely the result of the three- to-one power difference between the total beam powers used in the discrete system and F-OAM training processes. Additionally, the low beam powers used

to train the F-OAM required a recording time of 3 minutes. Based on results from experiments conducted in the discrete architecture, the object reconstructed at C3 may have been degraded by deformities in the holographic gratings caused by vibration induced beam fluctuations occurring over the course of the extended recording process. Two alternatives for increasing the beam power at C1 are 1) replace the current input mirror with one that is 50% rather than 94% reflective over half its surface, and 2) coat the input and output faces of all four crystals with a quarter wave anti-reflection coating to reduce power losses at the crystal faces.

5.5 Conclusion

Experiments conducted in the discrete architecture showed that in order to achieve success with the F-OAM architecture, the design must overcome internal and external power losses, correct for deviations in the feedback beam path and control the effects of beam fanning noise. Power was conserved by redesigning the external optical infrastructure used to provide the object reference and pump beams. Beam power could be increased further by lowering the reflectivity of the input mirror and anti- reflection coating the photorefractive crystals. Translation and angular deviations in the internal feedback beam caused by crystals C1, C2 and C3 were corrected through the use of a plate glass compensator inserted in the feedback beam path between C3 and the output mirror M2. The compensator was not able to correct beam deviations caused by C4; thus, the attenuation element was not used in the F-OAM experiments. Future associative memory experiments conducted in the FPCR should consider using a separate liquid crystal gate for each crystal rather than a single compensator for all four crystals. The effects of beam fanning noise were minimized by placing the gain crystal outside the resonator's midplane.

After designing the system to account for lessons learned from experiments in the discrete architecture, a single object was stored in the F-OAM's memory. The system was then able to reconstruct a complete object when presented with an incomplete version of the stored object. Although the reconstructed object was clearly discernable, it lacked the intensity and edge definition of the discrete system output. Because the major difference between the operation of both architectures was the total power in their respective object and reference beams, it is believed that increasing the F-OAM's beam power though the design changes discussed above will improve system performance. Finally, like the discrete architecture, the F-OAM is only capable of single

memory operation.

VI. Conclusions and Recommendations

6.1 Introduction

This chapter begins by summarizing the theoretical and experimental work performed throughout the course of this thesis. The results of these experiments are then used to draw conclusions about the effectiveness of the F-OAM and discrete associative memory designs. The chapter ends with a brief description of original contributions made during the course of this thesis.

6.2 Summary

The theory investigated in this thesis focused primarily on the operation of each of the components in the discrete and Fabry- Perot associative memory architectures. These included optical feedback in the Fabry-Perot Confocal Resonator and its discrete counterpart, two wave coupling gain and attenuation in $BaTiO_3$, and holographic storage and recall in $LiNbO_3$. The mathematical equations developed to model the operation of each component were combined to form a Fourier optics mathematical model describing the behavior of the complete F-OAM system. A comparison was then made between the Fourier optics system model and the equations describing the operation of a Hopfield neural network associative memory. It was shown the two were linked by an inner product associative memory recall process.

The experimental phase of the thesis began by characterizing the behavior of the $BaTiO_3$ crystals used as gain and attenuation elements in the F-OAM architecture. Experiments showed the formation of a phase conjugate return inside the gain crystal precluded the use of the theoretically investigated grating vector angles ($\beta = 0 - 90°$). The theory was then reexamined and it was found similar gain performance was predicted for grating vector angles between 270 and 360°. These predictions were verified by experiments that measured crystal gain as a function of input beam intensity ratio and grating vector angle.

The experimental behavior of the $BaTiO_3$ attenuation crystal was examined next. Attenuation measurements were taken over a wide range of input signal to pump beam intensity ratios. The experimental results matched the theoretical predictions and showed the current $BaTiO_3$ crystal outperformed the crystal investigated by Wilson.

Using the above experimental results as guidelines, the internal architecture proposed by Wilson was constructed inside a discrete model of the Fabry-Perot Confocal Resonator built from lenses, mirrors, beamsplitters and a 90/10 Fresnel beam sampler. Initial experiments conducted in the discrete resonator revealed the system was not capable of clearly reproducing an object stored in memory when presented with a *complete* version of the stored object. In order to more easily investigate the cause of this behavior, a series of "off-line" holographic storage and recall experiments were conducted with a single $LiNbO_3$ crystal.

The $LiNbO_3$ experiments uncovered three major causes for the system's inability to reproduce a clearly discernable output object. First, the energy in the higher spatial frequency components of the input object's Fourier transform did not contain enough energy to form diffraction gratings in the volume hologram. Second, the intensity of the reconstructed reference beam was too small to overcome reflection losses at the $BaTiO_3$ attenuation crystal and diffraction efficiency losses at the second $LiNbO_3$ crystal. And third, the holographic gratings formed in the volume hologram were degraded by beam fluctuations and table vibrations that occurred during the recording process.

Several different types of phase diffusers were investigated for their ability to "spread" more energy into the objects higher spatial frequency components without drastically reducing the intensity of the object beam used to record the holograms. The best alternative was provided by a glass microscope slide etched in a 40% hydrofluoric acid solution for approximately 120 seconds.

The intensity of the reconstructed reference beam used to read the stored object out of the second $LiNbO_3$ crystal was increased by reversing the gain and attenuation elements in Wilson's original design. The impact of beam fluctuations and table vibrations on the recording process was reduced by shielding the complete architecture with a plexiglass cage, repairing and or replacing defective components in the optical infrastructure, and conducting the experiments late in the evening when building vibrations were at a minimum.

After implementing the above changes, the discrete system was again tested to determine if it was capable of reconstructing a complete object when presented a *complete* version of a stored object. Although the output was clearly visible for a few seconds, it quickly degraded to an edgeless "blob" of light superimposed on a high intensity, and seemingly random background

pattern. Further investigations revealed the beam fanning pattern generated by the $BaTiO_3$ gain crystal (located in the first image plane of the feedback loop) was being focused onto the $LiNbO_3$ crystal positioned in the loop's second Fourier plane. The energy in the pattern rapidly washed out the gratings stored in the $LiNbO_3$ crystal and created the intense background pattern at the system output. This problem was alleviated by moving the gain crystal out of the image plane and by blocking the beam fanning pattern before it reached the second $LiNbO_3$ crystal. Experiments conducted after making these changes showed the system was capable of reconstructing a complete object when presented with *partial* information about the object.

The lessons learned from the discrete associative memory architecture experiments were then applied toward the construction and operation of the F-OAM architecture. The system was constructed by aligning the FPCR to provide the smallest feedback phase deviations over the widest possible area. Initially, each of the internal components were inserted into the FPCR system in the same relative positions they occupied in the discrete optical feedback loop. However it was found the restrictive nature of the FPCR optical processing environment precluded placing the $BaTiO_3$ attenuation crystal in the second image plane of the resonator. Therefore, the crystal was repositioned in the path of the feedback beam approximately halfway between the second image plane and the input mirror. While checking the system alignment with a low intensity object beam, it was found the feedback and input beams were no longer aligned. The deviations in the feedback beam path were caused by the refractive properties and non- parallel geometry of the four photorefractive crystals used in the architecture.

In the discrete system, these path deviations were corrected by adjusting two of the optical elements comprising the four corners of the feedback loop. This provided the four degrees of freedom required to compensate for both translational and angular path deviations. Because of the symmetry of its architecture, the FPCR's mirrors will not, by themselves, compensate for these deviations. Therefore, a separate compensator was constructed which, when inserted into the feedback beam path, provided the four degrees of freedom needed to redirect the feedback beam onto the input beam. The compensator consisted of two near-optically flat glass plates that sandwiched a rubber O-ring filled with index matching fluid. It was found that simultaneously varying the relative position of both plates would correct for path deviations caused by three out of the four photorefractive crystals. The fourth crystal (i.e., the attenuation element) was not required

for single memory operation and was, therefore, removed from the system.

Initial attempts to store and retrieve a single object using the F-OAM architecture were unsuccessful. System tests revealed the intensities of the object and reference beams used in the recording process were too small to produce diffraction gratings in the $LiNbO_3$ crystals. Internal and external power measurements showed the optical infrastructure used to support the discrete architecture did not provide the power required to overcome losses at the FPCR's input mirror. The infrastructure was then completely redesigned to increase the input object beam power, provide an external Fourier plane in which to control the size of the phase encoded Fourier transform in the FPCR cavity, and eliminate Fresnel rings present in the reference beam. As was the case in the discrete architecture, the F-OAM was able to reconstruct a complete object when presented with *partial* information about the object.

6.3 Conclusions

Both the Fabry-Perot Confocal Resonator Associative Memory and its discrete counterpart were able to store and recall a single memory. However, the difficulties associated with implementing each architecture, as well as the potential each has for multiple memory storage and recall are quite different.

A side by side comparison of the output objects produced by both systems is shown in Figure 85. Although both objects are clearly discernable, the output from the discrete system is brighter, has better defined edges, and contains less noise than the F-OAM output. The brightness and edge enhancement achieved with the discrete system is believed to be a result of the larger object and reference beam intensities used in the storage and recall process. This implies the F-OAM output could produce similar results with equal beam intensities. As discussed earlier, two possible methods for achieving these intensity levels are to 1) use an input mirror with 50% reflectivity over half of its surface, and 2) quarter-wave coat each of the photorefractive crystals to reduce reflection losses at their input and output faces.

The noise in both figures is primarily caused by the beam fanning pattern generated by the gain crystal. In the discrete system, the majority of the noise is blocked by the spatial filter. The restrictive nature of the F-OAM's processing environment, however, only allows enough room to

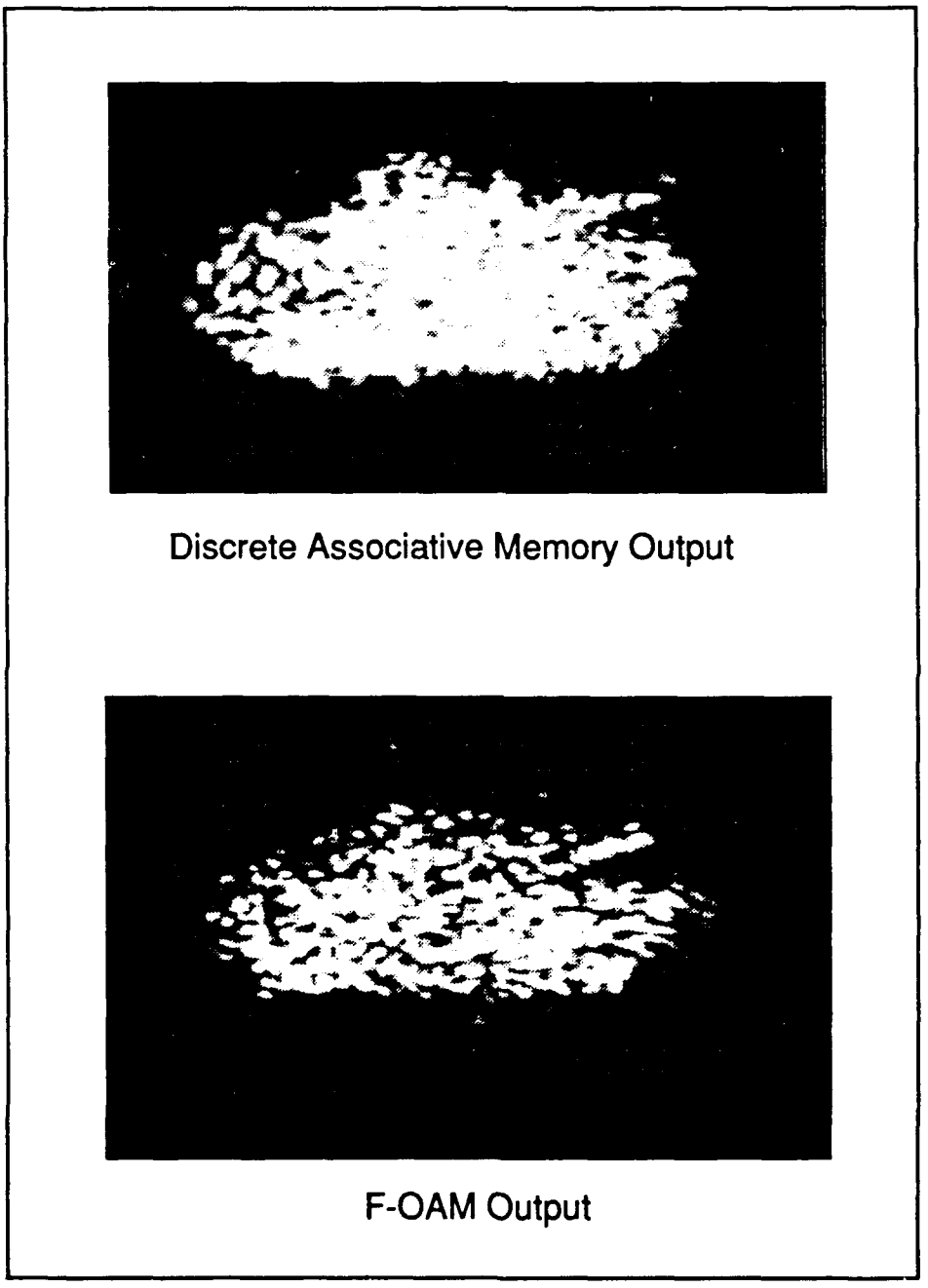

Figure 85. A side by side comparison of the F-OAM and discrete system outputs.

block a portion of the beam fanning pattern. The remainder freely propagates inside the resonator where it contributes to grating decay in the second $LiNbO_3$ crystal and background noise in the system output. Attempts to block the noise at various locations in the system were unsuccessful, leading to the conclusion that the presence of beam fanning noise is probably an inevitability of the F-OAM architecture used here.

Another important difference between the performance of both systems was their ability to compensate for feedback path deviations caused by the refractive media and non-parallel geometry of the photorefractive crystals. When the internal processing elements were removed from the system, the Fabry-Perot confocal resonator is a far superior feedback processing environment. However, when the crystals were added to both systems, the discrete architecture was able to correct for path deviations caused by all four crystals, while the FPCR, with the compensator present, was only able to correct for path deviations introduced by three of the crystals. Although a "stronger" compensator might compensate for the path deviations caused by the addition of the fourth crystal, it is recommended that future experiments in the FPCR consider using separate liquid crystal gates to individually compensate for beam path deviations introduced by each crystal.

The final, and probably most important, figure of merit for judging the performance of both systems is their potential for multiple memory operation. As Stoll and Lee have shown, the discrete feedback system can be expanded to accommodate at least two stored memories by inserting a gain element in the first image plane of the optical feedback loop. The gain element is designed to focus each reference beam generated at the first $LiNbO_3$ crystal onto a single $BaTiO_3$ gain crystal. This avoids the need for using a separate gain crystal to amplify each reconstructed reference beam, which, as shown earlier, is highly impractical. In order to store and recall more than one memory in the F-OAM with a single gain element, the current design must also be modified to combine the reference beams at a single location. Because a design alternative for achieving this behavior is not readily apparent, the next phase of the research process should focus on this area.

6.4 Contributions

The following list summarizes original contributions made during the course of this thesis.

- *Two Wave Coupling Gain for $\beta > 90^o$.* Developed and experimentally verified theoretical two wave coupling $BaTiO_3$ gain curves for grating vector angles between 270 and 360^o. Demonstrates two wave coupling gain is possible for angles other than the $0 - 90^o$ regime found in the literature. Provides alternative gain orientations for use in system design.

- *Two Wave Coupling Attenuation Model.* Developed and experimentally verified theoretical model describing two wave coupling $BaTiO_3$ attenuation behavior. The model was derived in a straightforward manner from Khuktarev's two wave coupling gain equations. Allows one to theoreticallly predict attenuation profile for a given crystal geometry and beam orientation.

- *Discrete Fabry-Perot Confocal Resonator Optical Associative Memory.* Substantially modified F-OAM design originally proposed by Wilson. Modifications included employing dynamic, volume holographic media rather than static, thin film media, placing a $BaTiO_3$ gain crystal between both $LiNbO_3$ crystals to enhance the efficiency of the holographic recall process, repositioning the $BaTiO_3$ attenuation element in the feedback arm of the resonator, phase encoding the object beam with an acid etched phase diffuser to improve the diffraction efficiency at the first $LiNbO_3$ crystal, and placing the gain crystal ahead of the spatial filter to minimize grating degradation caused by beam fanning noise. Designed optical infrastructure to provide object, reference and pump beams to internal components. Successfully stored and recalled a complete object from partial information about the object

- *Fabry-Perot Confocal Resonator Optical Associative Memory.* Transplanted internal component design developed in the discrete architecture into the Fabry-Perot Confocal Resonator optical processing environment. Further modified F-OAM design by repositioning the attenuation element to accommodate object, reference and feedback beams, employing a plate glass compensator to correct path deviations in feedback beam, and redesigning optical infrastructure to externally control size of input object beam and eliminate non-uniform intensity distribution of reference beam. Developed and experimentally verified a Fourier optics mathematical model describing single object storage and recall in the Fabry-Perot Confocal Resonator Optical Associative Memory.

Bibliography

1. Abu-Mostafa, Yaser S. and Demetri Psaltis. "Optical Neural Computers," *Scientific American 87:* 88-95 (March 87).
2. Burckhardt, C.B. "Use of Random Phase Mask for the Recording of Fourier Transform Holograms of Data Masks," *Applied Optics 9:3* 695-700 (March 70).
3. Caulfield, John H. et al. "Optical Neural Networks," *Proceedings of the IEEE.* 1573-1583 (October 1989)
4. Casasent, David and Brian Telfer. "Key and Recollection Vector Effects on Heteroassociative Memory Performance," *Applied Optics, 89:* 272-283 (January 1989).
5. Cederquist, Jack and Sing Lee. "Confocal Feedback Systems with Space Variance, Time Sampling, and Secondary Feedback Loops," *Journal of the Optical Society of America, 71:* 643-650 (June 1981).
6. Cederquist, Jack and Sing Lee. "The Use of Feedback in Optical Information Processing," *Applied Physics, 79:* 311-319.
7. Eichler, H.J. et al. *Laser-Induced Dynamic Gratings.* New York: Springer-Verlag, 1986.
8. Fainman, Y. and S. Lee. "Experimental Evaluation of Mangin Mirror Performance for Optical Processing with Feedback," *Optical Engineering, 24:* 535-540 (May/June 1985).
9. Fainman, Y. et al. "Optimal Coherent Image Amplification by Two Wave Coupling in Photorefractive $BaTiO_3$," *Optical Engineering, 25:* 228 - 234 (February 1986).
10. Farhat, Nabil H. "Optoelectronic Analogs of Self-Programming Neural Nets: Architecture and Methodologies for Implementing Fast Stochastic Learning by Simulated Annealing," *Applied Optics, 26:* 5093-5103 (December 1987).
11. Feinberg, Jack. "Optical Phase Conjugation in Photorefractive Materials," *Optical Phase Conjugation,* edited by Robert A. Fisher. New York: Academic Press, 1983.
12. Fisher, Arthur D. et al. "Optical Implementations of Associative Networks with Versatile Adaptive Learning Capabilities," *Applied Optics 87:* 5039-5053 (December 1987).
13. Frye, Dwayne William. *Neural Network Associative memory Using Non-Linear Holographic Storage Media.* MS Thesis AFIT/GEO/ENG/89D-3. School of Engineering, Air Force Institute of Technology (AU), Wright-Patterson AFB OH, December 1989 (DTIC number not available at this time).
14. Gaskill, Jack D. *Linear Systems, Fourier Transforms, and Optics.* New York: John Wiley and Sons, 1978.
15. Goodman, J.W. *Introduction to Fourier Optics.* New York: McGraw-Hill Book Company, 1968.
16. Gunter. P. "Holography, Coherent Light Amplification and Optical Phase Conjugation with Photorefractive Materials," *Physics Reports (Review Section of Physics Letters), 93:* 199-299 (January 1982)

17. Hopfield, J.J. "Neural Networks and Physical Systems with Emergent Collective Computational Abilities," *Proc. Natl. Acad. Sci. USA, 79:* 2554-2558 (April 1982).

18. -----. "Neurons With Graded Response Have Collective Computational Properties Like Those of Two-State Neurons," *Proc. Natl. Acad. Sci. USA, 81:* 3088- 3092 (May 1984).

19. Kabrisky, Matthew. Class handout distributed in EENG 620, Pattern Recognition. School of Engineering, Air Force Institute of Technology (AU), Wright-Patterson AFB OH, September, 1989.

20. Kogelnick, Herwig. "Coupled Wave Theory for Thick Hologram Gratings," *The Bell System Technical Journal, 48:* 2909-2947 (November, 1969).

21. Kuhktarev, N. V. et al "Holographic Storage in Electrooptic Crystals. II. Beam Coupling - Light Amplification," *Ferroelectrics, 22:* 961-964 (1979).

22. Keppler, K.S. *Optical Amplification in* 45^o*-cut* $BaTiO_3$. MS Thesis AFIT/GEO/ENG/89D-5. School of Engineering, Air Force Institute of Technology (AU), Wright- Patterson AFB OH, December 1989 (DTIC number not available at this time).

23. Lippman, Richard P. "An Introduction to Computing with Neural Nets," *IEEE ASSP Magazine, 87:* 4-22 (April 1987).

24. Maniloff, Eric S. and Kristina M. Johnson. "Dynamic Holographic Interconnects Using Static Holograms," *Optical Engineering, 29:* 225-229 (March 1990).

25. Owechko, Y. et al. "Holographic Associative Memory with Nonlinearities in the Correlation Domain," *Applied Optics, 26:* 1900-1910 (May 1987).

26. Paek, Eung Gi and Demetri Psaltis. "Optical Associative Memory Using Fourier Transform Holograms," *Optical Engineering, 26:* 428-433 (May 1987).

27. Psaltis, Demetri and Nabil Farhat. "Optical Information Processing Based on an Associative-Memory Model of Neural Nets with Thresholding and Feedback," *Optics Letters, 10:* 98-100 (February 1985).

28. Psaltis, Demetri et al. "Adaptive Optical Networks Using Photorefractive Crystals," *Applied Optics, 27:* 1752-1759 (May 1988).

29. Rogers, Steven K. et al. Class handout distributed in EENG 620, Pattern Recognition. School of Engineering, Air Force Institute of Technology (AU), Wright- Patterson AFB OH, September, 1989.

30. Stoll, H.M. and L-S. Lee. "A Continuous-Time Optical Neural Network," *Proceedings of the IEEE International Conference on Neural Networks, 2:* 373-384 (July 1988).

31. Lee, L.-S. et al. "Continuous-Time Optical Neural Network Associative Memory," *Optics Letters, 14:* 162- 164 (February 1989).

32. van Heerden, P.J. "A new Optical Method for Storing and Retrieving Information," *Applied Optics, 2:* 387-392 (1963).

33. Verdeyen, Joseph T. *Laser Electronics*. Englewood Cliffs, New Jersey: Prentics Hall Inc, 1989.

34. Vogel, George A. *Characterization of Barium Titanate as an Optical Amplifier.* DS Dissertation AFIT/DS/ENG/90-B. School of Engineering, Air Force Institute of Technology (AU), Wright-Patterson AFB, OH, December 1990.

35. Wilson, Jeffrey A. *Optical Information Processing in a Confocal Fabry-Perot Resonator.* MS Thesis AFIT/GEO/ENG/88D-5. School of Engineering, Air Force Institute of Technology (AU), Wright-Patterson AFB OH, December 1988.

36. Yariv, Amnon and Pochi Yeh. *Optical Waves in Crystals.* New York: John Wiley and Sons, 1984.

Vita

Captain Thomas J. Burns [redacted] He graduated from Iver C. Ranum High School in Westminster, Colorado in 1975 and attended Ohio State University where he received a Bachelor of Arts Degree in Philosophy in 1980. Upon graduation, he was accepted into the Air Force Undergraduate Engineering Conversion Program where he received his commission from Officer Training School and returned to Ohio State University to receive his Bachelor of Science Degree in Electrical Engineering. His first assignment was to Headquarters, Air Force Logistics Command at Wright-Patterson AFB, OH, where he served as Staff Electronics Engineer until entering the Air Force Institute of Technology in May 1989.

[redacted]

REPORT DOCUMENTATION PAGE

Form Approved
OMB No 0704-0188

1. AGENCY USE ONLY (Leave blank)	2. REPORT DATE	3. REPORT TYPE AND DATES COVERED
	December 1990	*Master's Thesis*

4. TITLE AND SUBTITLE
A Compact Optical Associative Memory Using Dynamic Holographic Storage Media and Photorefractive Gain and Attenuation Elements

5. FUNDING NUMBERS

6. AUTHOR(S)
Thomas Joseph Burns, Capt, USAF

7. PERFORMING ORGANIZATION NAME(S) AND ADDRESS(ES)
Air Force Institute of Technology, WPAFB OH 45433-6583

8. PERFORMING ORGANIZATION REPORT NUMBER
AFIT/GEO/ENG/90D-02

9. SPONSORING MONITORING AGENCY NAME(S) AND ADDRESS(ES)

10. SPONSORING / MONITORING AGENCY REPORT NUMBER

11. SUPPLEMENTARY NOTES

12a. DISTRIBUTION AVAILABILITY STATEMENT
Approved for Public Release; Distribution Unlimited.

12b. DISTRIBUTION CODE

13. ABSTRACT *(Maximum 200 words)*

This research effort implemented a compact optical associative memory architecture consisting of a Fabry-Perot Confocal Resonator (FPCR) optical processing environment, two dynamically reprogrammable Lithium Niobate volume holograms, and Barium Titanate gain and attenuation elements. The reduced physical dimensions of the compact optical processing environment make it more adaptable to military applications than previous associative memory designs. The FPCR employs Mangin mirrors designed to reduce spherical aberrations in off-axis rays. The orientation of the gain element's grating vector angle and the model used to predict the profile of the attenuation element were unique to this research effort. The object stored in the associative memory was phase encoded using a glass microsope slide etched in a 40% hydrofluoric acid solution. Beam path deviations caused by the non-parallel geometry of the photorefractive crystals were corrected with a variable pitch, plate glass optical wedge inserted in the cavity's feedback arm. Experimental results showed the system is capable of storing and fully retrieving a single object from memory when presented with partial information about the object. Additional system modifications are required to store and retrieve multiple objects.

14. SUBJECT TERMS
Associative Memory, Optical Feedback, Artificial Intelligence, Neural Networks

15. NUMBER OF PAGES
169

16. PRICE CODE

17. SECURITY CLASSIFICATION OF REPORT	18. SECURITY CLASSIFICATION OF THIS PAGE	19. SECURITY CLASSIFICATION OF ABSTRACT	20. LIMITATION OF ABSTRACT
Unclassified	Unclassified	Unclassified	UL